University of Kentucky
UKnowledge

Theses and Dissertations--Physics and Astronomy

Physics and Astronomy

2015

SYNTHESIS, INTEGRATION, AND PHYSICAL CHARACTERIZATION OF GRAPHENE AND CARBON NANOTUBES

David P. Hunley
University of Kentucky, patrickhunley@gmail.com

Right click to open a feedback form in a new tab to let us know how this document benefits you.

Recommended Citation
Hunley, David P., "SYNTHESIS, INTEGRATION, AND PHYSICAL CHARACTERIZATION OF GRAPHENE AND CARBON NANOTUBES" (2015). *Theses and Dissertations--Physics and Astronomy*. 28.
https://uknowledge.uky.edu/physastron_etds/28

This Doctoral Dissertation is brought to you for free and open access by the Physics and Astronomy at UKnowledge. It has been accepted for inclusion in Theses and Dissertations--Physics and Astronomy by an authorized administrator of UKnowledge. For more information, please contact UKnowledge@lsv.uky.edu.

STUDENT AGREEMENT:

I represent that my thesis or dissertation and abstract are my original work. Proper attribution has been given to all outside sources. I understand that I am solely responsible for obtaining any needed copyright permissions. I have obtained needed written permission statement(s) from the owner(s) of each third-party copyrighted matter to be included in my work, allowing electronic distribution (if such use is not permitted by the fair use doctrine) which will be submitted to UKnowledge as Additional File.

I hereby grant to The University of Kentucky and its agents the irrevocable, non-exclusive, and royalty-free license to archive and make accessible my work in whole or in part in all forms of media, now or hereafter known. I agree that the document mentioned above may be made available immediately for worldwide access unless an embargo applies.

I retain all other ownership rights to the copyright of my work. I also retain the right to use in future works (such as articles or books) all or part of my work. I understand that I am free to register the copyright to my work.

REVIEW, APPROVAL AND ACCEPTANCE

The document mentioned above has been reviewed and accepted by the student's advisor, on behalf of the advisory committee, and by the Director of Graduate Studies (DGS), on behalf of the program; we verify that this is the final, approved version of the student's thesis including all changes required by the advisory committee. The undersigned agree to abide by the statements above.

David P. Hunley, Student

Dr. Douglas R. Strachan, Major Professor

Dr. Timothy Gorringe, Director of Graduate Studies

SYNTHESIS, INTEGRATION, AND PHYSICAL CHARACTERIZATION OF GRAPHENE AND CARBON NANOTUBES

DISSERTATION

A dissertation submitted in partial fulfillment of the
requirements for the degree of Doctor of Philosophy in the
College of Arts and Sciences
at the University of Kentucky

By
David Patrick Hunley
Lexington, Kentucky

Director: Dr. Douglas R. Strachan, Assistant Professor of Physics and Astronomy
Lexington, Kentucky 2015

Copyright © David Patrick Hunley 2015

ABSTRACT OF DISSERTATION

SYNTHESIS, INTEGRATION, AND PHYSICAL CHARACTERIZATION OF GRAPHENE AND CARBON NANOTUBES

Graphene and carbon nanotubes are among the hottest topics in physics today. Both materials exhibit numerous remarkable mechanical, electrical, optical, and thermal properties that make them promising materials for use in a large number of diverse applications, especially in the field of nanotechnology. One of the ultimate goals driving the fields of nanoscience and nanotechnology has been the attainment of atomically precise construction of intricate integrated systems consisting of materials with diverse behavior. Specifically, it is desirable to have high performance conductors, semiconductors, and insulators integrated into complex atomically precise arrangements. This dissertation represents the culmination of work that has made significant progress towards achieving these goals. The main results of this study include the fabrication of graphene and carbon nanotubes successfully integrated into nanoscale systems with precise crystallographic orientations. These systems are shown to be electrically isolated and many of their properties are explored through the use of novel techniques in scanning probe microscopy.

KEYWORDS: graphene, carbon nanotubes, nanoelectronics, material properties, scanning probe microscopy

Student's Signature: David Patrick Hunley

Date: February 13, 2015

SYNTHESIS, INTEGRATION, AND PHYSICAL CHARACTERIZATION OF GRAPHENE AND CARBON NANOTUBES

By

David Patrick Hunley

Douglas R. Strachan
Director of Dissertation

Timothy Gorringe
Director of Graduate Studies

February 13, 2015

ACKNOWLEDGMENTS

First and foremost, this work would not have been completed without the excellent guidance from my advisor, Professor Douglas Strachan. Never lacking in ideas, Doug consistently provided positive and supportive direction as I pursued my Ph.D. I sincerely thank him for sharing his knowledge and providing me with all the tools necessary to succeed.

I would like to express my appreciation to my Ph.D. committee members, Professors Joe Brill, Gang Cao, and Y. T. Cheng. I thank them for their time and input throughout the course of my research. I thank the technical staff, including Gene Baber, Jim Morris, Charles Tipton, Steve Maynard, Greg Porter, Rick Carr, Chuck May, and Brian Wajdak, who have assisted in helping design, maintain, and build components that enabled parts of this work to be carried out. I also thank the department's support staff for all of their assistance.

It would have been a lonely and much more difficult journey without my friends and co-workers. Thanks to all of you, especially: Stephen Johnson, Abhishek Sundararajan, Mohsen Nasseri, Mathias Boland, Aram Arash, Armin Ansary, and Javad Farrokhi.

For sparking my interest and inspiring me to pursue a career in science, I would like to thank a few of the most influential teachers and professors I've had along the way. In chronological order, I give thanks to Randall Scoville, formerly of Highlands Intermediate, David Pevovar at Central Kitsap High School, and Professors Capp Yess, Kent Price, Ignacio Birriel, and Jennifer Birriel at Morehead State University.

Finally, I would like to especially thank my family. Thank you Mom, Dad, and Alex for your loving support and encouragement throughout my entire life. It has provided me with the confidence, fortitude, and ambition to challenge myself and to pursue my goals. Thank you to my loving wife, Kim. I'm so very lucky to have you with me through all of life's journeys. What's next?

TABLE OF CONTENTS

ACKNOWLEDGMENTS iii
LIST OF TABLES vi
LIST OF FIGURES vii

CHAPTER 1: Background and Theory 1
1.1 Properties and Potential Applications 1
1.2 Chemical Structure 3
1.3 Graphene Band Structure 6
1.4 Carbon Nanotube Band Structure 11
1.5 Chirality in Carbon Nanotubes 13
1.6 Electron Transport 14
1.7 Contact Resistances 18
1.8 Strain-Induced Effects in Graphene 20

CHAPTER 2: Electrostatic Force Microscopy and Electrical Isolation of Etched Few-Layer Graphene Nano-Domains 21
2.1 Introduction 21
2.2 Experimental Details 22
2.3 Investigating Nano-Domains in Graphene 23
2.4 Comparison to Finite Element Simulations 26
2.5 Modeling Resistance between Isolated Nano-Domains 30
2.6 Relevant Time Scales 31
2.7 Lower-Bound Estimate of Etch-Track Resistance 34
2.8 Conclusions 35

CHAPTER 3: Crystallographically Aligned Carbon Nanotubes Grown on Few-Layer Graphene Films 36
3.1 Introduction 36
3.2 Experimental Details 37
3.3 Results of Nanotube Growth Process 38
3.4 Determination of the Crystallographic Direction of Growth 39
3.5 Thickness Dependence of Nanotube Alignment 42
3.6 Unique Nanotube Morphologies 44
3.7 Potential for Transferring Nanotubes to Insulating Substrates 47
3.8 Conclusions 50

CHAPTER 4: Integrated Nanotubes, Etch Tracks, and Nanoribbons in Crystallographic Alignment to a Graphene Lattice 51
4.1 Introduction 52
4.2. Experimental Details 53
4.3 Bridging Nanogaps with Nanotubes 54
4.4 Potential Growth Mechanisms 59
4.5 Conclusion 64

CHAPTER 5: Friction, Adhesion, and Elasticity of Graphene Edges 66
5.1 Introduction 66
5.2 Experimental Details 67
5.3 AFM and LFM of Graphene Edges 68
5.4 Quantifying LFM Forces 70
5.5 Novel Low-Load LFM Calibration Technique 72
5.6 Flexing an Exposed Graphene Edge 74
5.7 Spring Constant of Graphene Edges 76
5.8 Modeling the Observed Stick-Slip 76
5.9 Graphene Flexing Modes 77
5.10 Conclusions 78

CHAPTER 6: Analytical Model for Self-Heating in Nanowire Geometries 79
6.1 Introduction 79
6.2 Model of Heat Generation in a Nanowire Field Effect Transistor 80
6.3 Assumptions and Boundary Conditions 82
6.4 Comparisons to Finite Element Simulations 86
6.5 Electrical Current Studies 88
6.6 Nanowire Width and Oxide Thickness Studies 89
6.7 Significant Improvement over Other Models 90
6.8 Geometrical Regimes of Validity 91
6.9 Temperature-dependent Resistivities 93
6.10 Conclusions 94

APPENDICES 96
Appendix A: Cantilever Characterization 96
Appendix B: Lateral Force Models 99

REFERENCES 103

VITA 109
EDUCATION 109
PROFESSIONAL EXPERIENCE 109
PUBLICATIONS 110
PATENTS 111
HONORS AND AWARDS 111

LIST OF TABLES

Table 6.1. Thermal healing lengths L_H for the nanowires of widths W and electrical insulator thicknesses d 93

LIST OF FIGURES

Figure 1.1. Graphene is the two-dimensional building material for zero-dimensional fullerenes, one-dimensional nanotubes, and three-dimensional graphite. 1
Figure 1.2. Illustration of the shape of the ground state orbitals of the carbon atom. 3
Figure 1.3. Illustration of one of the 2s electrons getting pulled into the higher p orbital. 4
Figure 1.4. Illustration of the hybridized orbitals in graphene. 5
Figure 1.5. Illustration of the bonding arrangement between two carbon atoms in graphene. 5
Figure 1.6. Graphene's lattice structure. 7
Figure 1.7. Illustration of the energy dispersion surface of in graphene. 10
Figure 1.8. The dispersion relation near graphene's K point is found to be linear. 10
Figure 1.9. Reciprocal lattice of graphene. 11
Figure 1.10. Illustration of the zone folding technique. 12
Figure 1.11. Schematic diagram illustrating a carbon nanotube's chirality. 14

Figure 2.1. Atomic force microscope topography image of a bi-layer graphene 25
Figure 2.2. The quadratic fitting coefficient of the EFM phase curves plotted against the surface area of the bi-layer graphene domain size directly below the tip 26
Figure 2.3. Finite element simulations of the electrostatic interactions between the EFM tip and the etched FLG sample. 29
Figure 2.4. A simplified circuit diagram that approximates the electrostatic force microscopy measurement 31

Figure 3.1. SEM image of NTs aligned to the crystallographic axes of FLG. 39
Figure 3.2. AFM phase image of NTs and etch tracks in graphene. 41
Figure 3.3. SEM image of NTs grown on regions of a contiguous flake of FLG 43
Figure 3.4. SEM images of NTs showing abrupt changes in crystallographic alignment.45
Figure 3.5. AFM height image of NTs 50

Figure 4.1. AFM image of a CNT traversing a graphene nanogap etch track. 56
Figure 4.2. SEM image of two parallel CNTs traversing an armchair-directed etched FLG nanogap. 58
Figure 4.3. SEM image of a nanotube traversing two closely spaced etch tracks that bound a FLG nanoribbon. 59
Figure 4.4. Model of a CNT traversing a FLG nanogap. 63

Figure 5.1. AFM and LFM of graphene crosses. 69
Figure 5.2. Local frictional characteristics of graphene edges. 72
Figure 5.3. Topography of graphene edges determined through LFM. 74
Figure 5.4. Elastic response of graphene edge. 75

Figure 6.1. Metallic nanowire geometry and electrodes 82
Figure 6.2. Finite-element simulation 88
Figure 6.3. Plot of temperature rise versus position for a range of applied current densities for a nanowire. 88

Figure 6.4. Simulations (small circles) and our model (solid-blue lines) for nanowires .. 90
Figure 6.5. Simulations (small circles) focusing on the contact region for nanowires 92
Figure 6.6. Plot of temperature rise versus position for a nanowire with a temperature-independent resistivity 94

Figure A1. Adhesion/Force Curve Plots. 97
Figure A2. Adhesion force maps over various regions of sample. 97
Figure A3. Effects of tip-wear. 98

CHAPTER 1: Background and Theory

1.1 Properties and Potential Applications

Graphene and carbon nanotubes are among the hottest topics in physics today. Both materials exhibit numerous remarkable mechanical, electrical, optical, and thermal properties that make them promising materials for use in a large number of diverse applications.

Graphene, which is a single atomic layer of graphite, is an allotrope of carbon characterized by its two-dimensional, hexagonal structure of sp^2-bonded carbon atoms. It can also be thought of as the base structure of fullerenes, carbon nanotubes, and graphite as illustrated in Fig. 1.1.

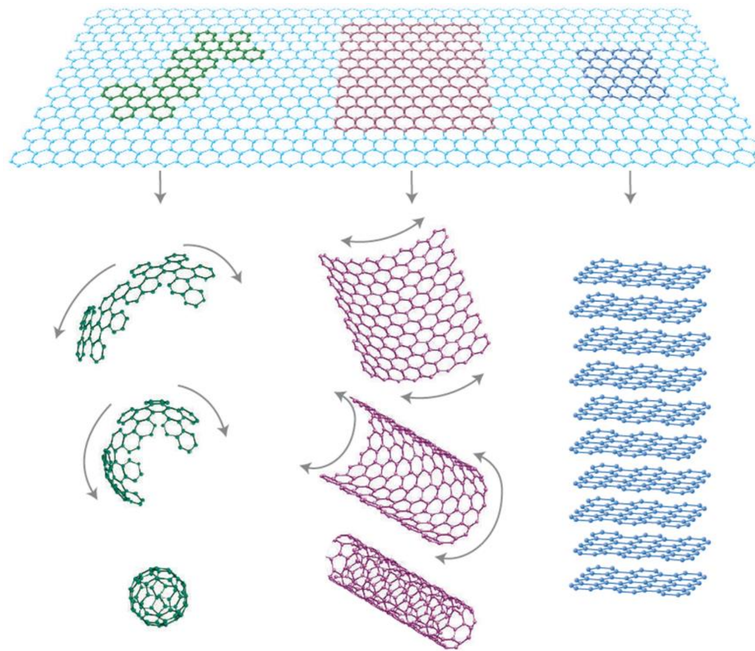

Figure 1.1. Graphene is the two-dimensional building material for zero-dimensional fullerenes, one-dimensional nanotubes, and three-dimensional graphite.[1] Reprinted by permission from Macmillan Publishers Ltd: Nature Materials (Vol. 6), © 2007

With an intrinsic tensile strength of 130 GPa and a Young's modulus of 1 TPa, graphene is one of the strongest materials ever discovered.[2] For comparison, its tensile strength is 50 times greater than diamond and it's Young's modulus is about 5 times that of steel, while graphene's density is a mere one-tenth that of steel.

Perhaps even more astonishing are graphene's electrical properties, which are a result of the two-dimensional nature of the material. Pristine suspended graphene is expected to exhibit an electron mobility of 200,000 cm^2/Vs at room temperature, which is ten times greater than that of copper.[3,4] While traveling through the sheet, the electrons behave as nearly massless particles, which will be discussed further in this chapter. The thermal conductivity of graphene is also excellent, with a value around 5000 W/mK.[5] This is over an order of magnitude greater than copper.

Though graphene is an excellent conductor, it has been found to absorb approximately 2.3% of white light.[6] This is a surprising amount, considering graphene is merely one atomic layer thick. However, this property has played a very important role in graphene's discovery and subsequent research, as the ability to visually identify graphene with a relatively inexpensive optical microscope has no doubt expedited progress in its research. However, graphene is still a highly transparent material and as such, lends itself to a number of potential applications such as use as a conductive coating in solar cells and liquid crystal displays.

Additional applications that could make use of graphene's unique electronic and thermal properties include supercapacitors, batteries, sensors, and nanoscale devices such field effect transistors. There are also a whole host of applications that could utilize graphene's incredible mechanical properties, such as structural and material reinforcement agents, use as an additive in lubricants, and in micro- and nanoelectromechanical devices.

The incredible properties of both graphene and carbon nanotubes are due to their chemical structure and resulting band structure. Therefore these important concepts will be developed in the following section.

1.2 Chemical Structure

The carbon atom, which has 6 electrons, has a ground state electronic configuration of $1s^2 2s^2 2p^2$. The shape of the associated ground state orbitals of the carbon atom are depicted in Fig. 1.2 below. Both the 1s and 2s electron orbitals are spherical in shape though only the much larger 2s orbital is shown. The 2p electrons form lobe-shaped orbitals that are perpendicular to each other and, by convention, are depicted to lie in the x-y plane.

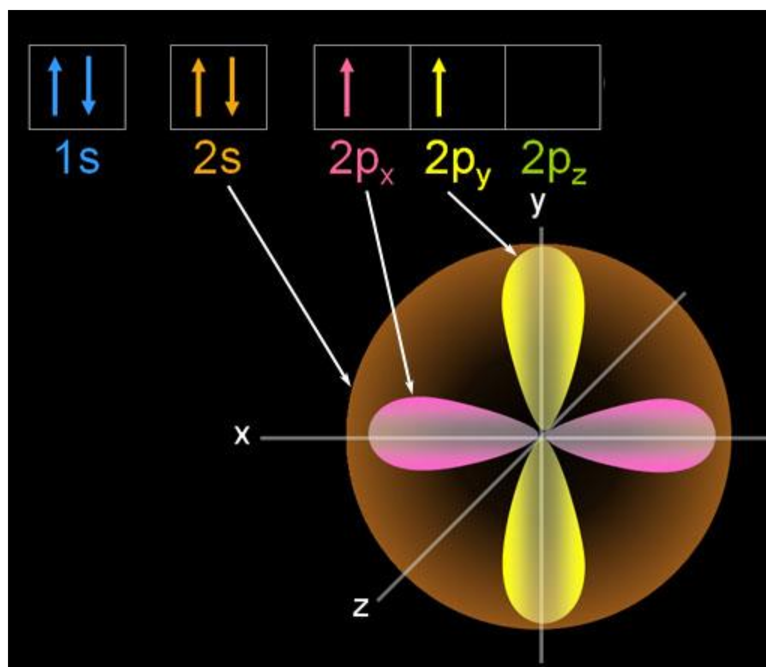

Figure 1.2. Illustration of the shape of the ground state orbitals of the carbon atom. Reprinted by permission from Ref [7].

If the carbon atom is brought into close proximity to another atom, it is possible for one of the 2s electrons to be pulled into the higher p orbital, as is illustrated in Fig. 1.3.

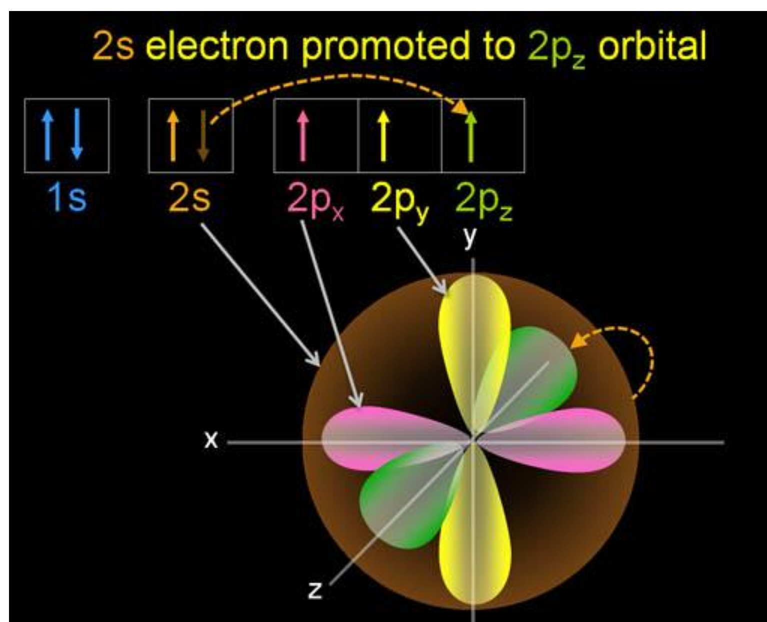

Figure 1.3. Illustration of one of the 2s electrons getting pulled into the higher p orbital. Reprinted by permission from Ref [7].

At this point, hybridization occurs between the 2s electron and two of the 2p electrons to form three sp^2 orbitals that are trigonal planar, meaning all three orbitals lie on the same plane separated by 120°. This hybridization and subsequent covalent bonding in graphene forms its distinctive hexagonal structure. The remaining 2p electron is in a p-orbital that is perpendicular to the plane of the sp^2 orbitals, and is referred to as the $2p_z$ electron by convention. This is illustrated in Fig. 1.4.

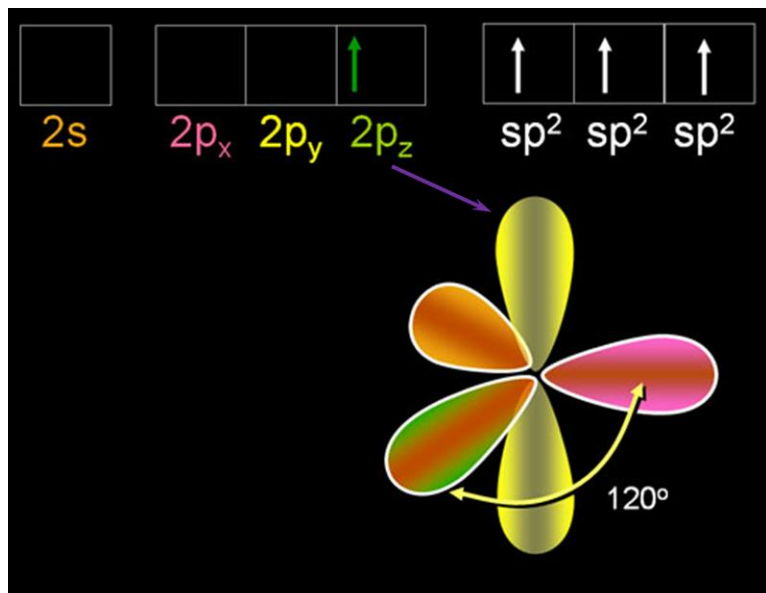

Figure 1.4. Illustration of the hybridized orbitals in graphene. Reprinted by permission from Ref [7].

The carbon atom then bonds with other nearby carbon atoms, in which the sp^2 orbitals from each atom form sigma bonds. This results in the familiar hexagonal shape of the carbon bonds in graphene and carbon nanotubes and is the source of these materials' incredible mechanical strength. The p_z electrons then form delocalized pi bonds which are responsible for conduction in these allotropes. This bonding arrangement is illustrated in Fig. 1.5.

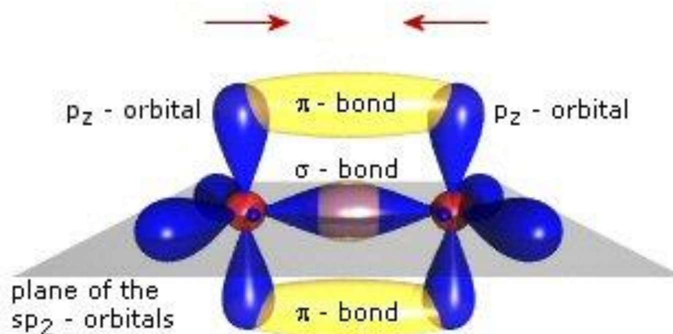

Figure 1.5. Illustration of the bonding arrangement between two carbon atoms in graphene. Reprinted by permission from Ref [8].

1.3 Graphene Band Structure

As we've seen, the carbon atoms in graphene form a planar, hexagonally shaped crystal structure. Though all atoms are carbon, a hexagonal lattice is not a Bravais lattice because there are non-equivalent atomic sites. As such, graphene's lattice structure must be considered as the combination of two sub-lattices (Fig. 1.6) such that the elementary unit cell consists of a basis with two p_z electrons (one from each carbon atom in the unit cell), the bands of which are referred to as the π and π^* bands.

All of this results in some very unique and interesting phenomena. For example, in graphene, charge carriers propagating through the lattice at low energies can be better described as effectively massless particles by a two dimensional analog of the Dirac equation, rather than the Schrodinger equation for spin=1/2 particles. Using the tight-binding model for graphene, we will find that the valence and conduction bands touch each other at 6 points, referred to as the K-points or Dirac points, where the three-dimensional dispersion relation is approximately conical.

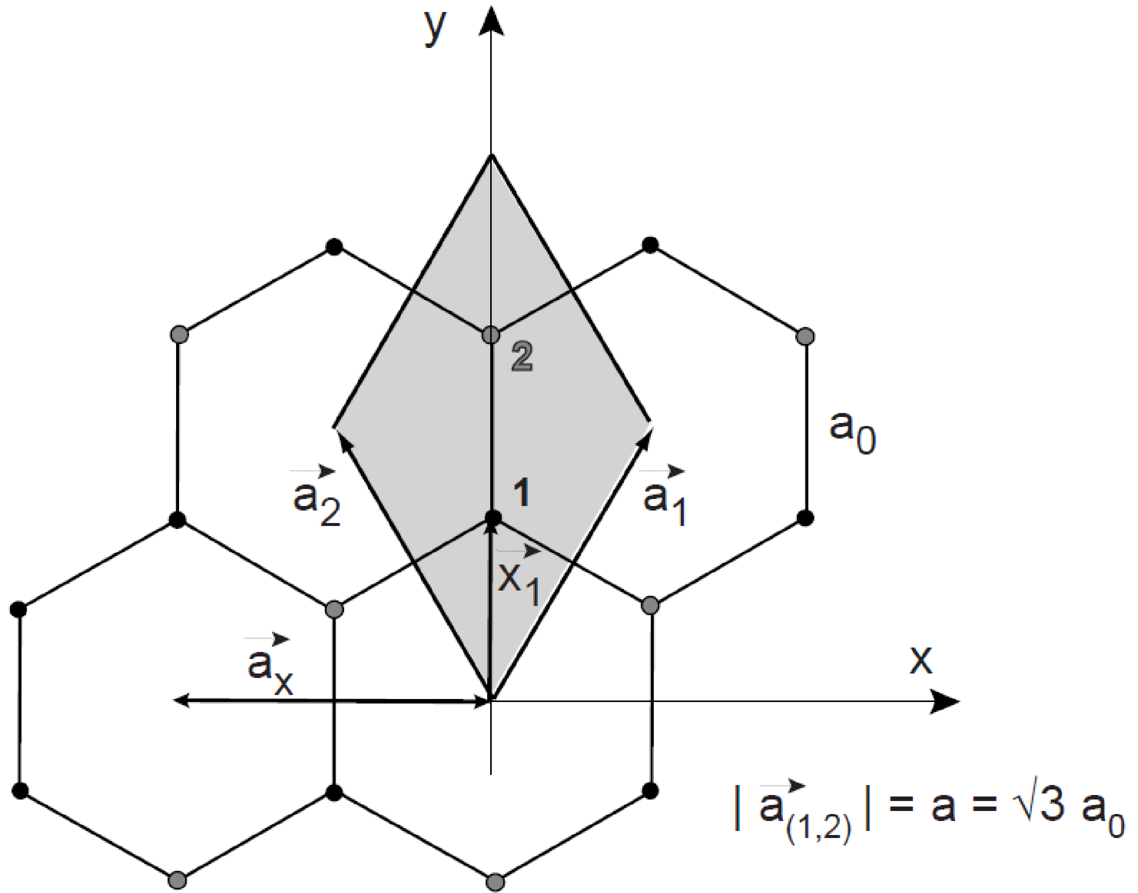

Figure 1.6. Graphene's lattice structure. Adapted from Ref[9].

From Fig 1.6, we can see that graphene's lattice vectors can be written as:

$$\vec{a}_1 = a_0\sqrt{3}(\tfrac{1}{2}, \tfrac{\sqrt{3}}{2})$$

$$\vec{a}_2 = a_0\sqrt{3}\left(-\tfrac{1}{2}, \tfrac{\sqrt{3}}{2}\right).$$

The wavefunction Ansatz is:

$$\psi_{\vec{k}} = \sum_{\vec{R}\in G} e^{i\vec{k}\cdot\vec{R}}\phi(\vec{x} - \vec{R})$$

where G denotes the set of lattice vectors, $\vec{x}$ is the position of a carbon atom within the until cell, and ϕ is the atomic wavefunctions, which in this case is the linear combination of the two p_z atomic orbitals (one from each atom in the unit cell). Therefore

$$\phi(\vec{x}) = b_1\phi_1(\vec{x}) + b_2\phi_2(\vec{x}) = \sum_n b_n\phi_n$$

and the Hamiltonian for an electron in the atomic potential due to all the carbon atoms is given by

$$H = \frac{\vec{p}^2}{2m} + \sum_{\vec{R}\in G}(V_{at}\left(\vec{x} - \vec{x}_1 - \vec{R}\right) + (V_{at}\left(\vec{x} - \vec{x}_2 - \vec{R}\right)$$

From these, we find

$$H\phi_1 = \epsilon_1\phi_1 + \left(\sum_{\vec{R}\neq 0}\left(V_{at}\left(\vec{x} - \vec{x}_1 - \vec{R}\right) + (V_{at}\left(\vec{x} - \vec{x}_2 - \vec{R}\right)\right) + (V_{at}(\vec{x} - \vec{x}_2)\right)\phi_1$$

where ϵ_1 is the eigenvalue for the atomic p_z state. Substituting the second term on the right hand side of the above equation with $\Delta U_1\phi_1$, we can write the two relevant equations more simply as:

$$H\phi_{1,2} = \epsilon_{1,2} + \Delta U_{1,2}\phi_{1,2}$$

At this point, we note that $\epsilon_1 = \epsilon_2$ and that we can arbitrarily set the energy to any value. We choose $\epsilon_{1,2} = 0$ so that

$$H\phi_{1,2} = \Delta U_{1,2}\phi_{1,2}$$

Now we need to solve the Schrodinger equation:

$$H\psi_{\vec{k}} = E(\vec{k})\psi_{\vec{k}}$$

Since we have two unknown constants, b_1 and b_1, we require two equations to solve the eigenvalue problem. Assuming that only the nearest-neighbor overlap integrals have to be taken into account and that the integral is real,

$$E\left(\vec{k}\right)\langle\phi_j|\psi\rangle = \langle\phi_j|\Delta U_j|\psi\rangle$$

$$\langle \phi_1 | \psi \rangle = b_1 + b_2 \left(\int \phi_1^* \phi_2 \right) \left(1 + e^{-i\vec{k}\cdot\vec{a}_1} + e^{-i\vec{k}\cdot\vec{a}_2} \right)$$

$$\langle \phi_2 | \psi \rangle = b_2 + b_1 \left(\int \phi_2^* \phi_1 \right) \left(1 + e^{i\vec{k}\cdot\vec{a}_1} + e^{i\vec{k}\cdot\vec{a}_2} \right)$$

In a similar manner, we now calculate $\langle \phi_j | \Delta U_j | \psi \rangle$.

$$\gamma_1 = \int \phi_1^* \Delta U_1 \phi_2 = \int \phi_2^* \Delta U_2 \phi_1$$

These two integrals are equal due to symmetry and we have:

$$\langle \phi_1 | \Delta U_1 | \psi \rangle = b_2 \gamma_1 \left(1 + e^{-i\vec{k}\cdot\vec{a}_1} + e^{-i\vec{k}\cdot\vec{a}_2} \right)$$

$$\langle \phi_2 | \Delta U_1 | \psi \rangle = b_1 \gamma_1 \left(1 + e^{i\vec{k}\cdot\vec{a}_1} + e^{i\vec{k}\cdot\vec{a}_2} \right)$$

Combining all that we have found, we have for the eigenvalue problem

$$\begin{pmatrix} E(\vec{k}) & \alpha(\gamma_0 E(\vec{k}) - \gamma_1 \\ \alpha^*(\gamma_0 E(\vec{k}) - \gamma_1 & E(\vec{k}) \end{pmatrix} \begin{pmatrix} b_1 \\ b_2 \end{pmatrix} = \begin{pmatrix} 0 \\ 0 \end{pmatrix}$$

where for simplicity, we have made the substitution

$$\alpha(\vec{k}) = 1 + e^{-i\vec{k}\cdot\vec{a}_1} + e^{-i\vec{k}\cdot\vec{a}_2}$$

and γ_0 is the overlap integral

$$\gamma_0 = \int \phi_2^* \phi_1 \in \mathbb{R}.$$

Setting the determinant equal to zero and making use of the fact that γ_0 is small, we find

$$E(\vec{k}) = \pm \gamma_1 |\alpha(\vec{k})|$$

Calculating the magnitude of $\alpha(\vec{k})$ and using the x- and y-components of $\vec{k}$, we arrive at our expression for $E(\vec{k})$ for graphene[9]:

$$E_g(k_x, k_y) = \pm \gamma_1 \sqrt{1 + 4\cos\left(\frac{\sqrt{3}ak_y}{2}\right)\cos\left(\frac{ak_x}{2}\right) + 4\cos^2\left(\frac{ak_x}{2}\right)} \qquad \text{Eq. 1.1}$$

The full energy dispersion surface can be seen in Fig. 1.7, and the linear dispersion relation near one of graphene's K-points can be seen in the plot in Fig. 1.8.

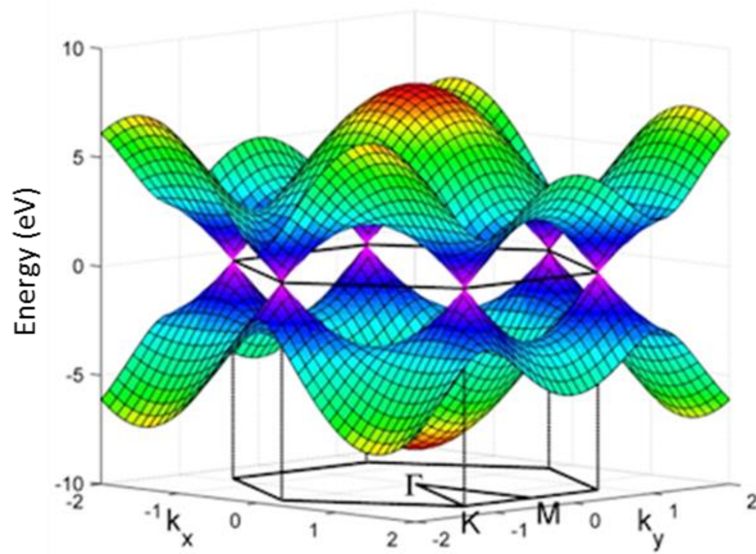

Figure 1.7. Illustration of the energy dispersion surface of in graphene. Adapted from Ref [10].

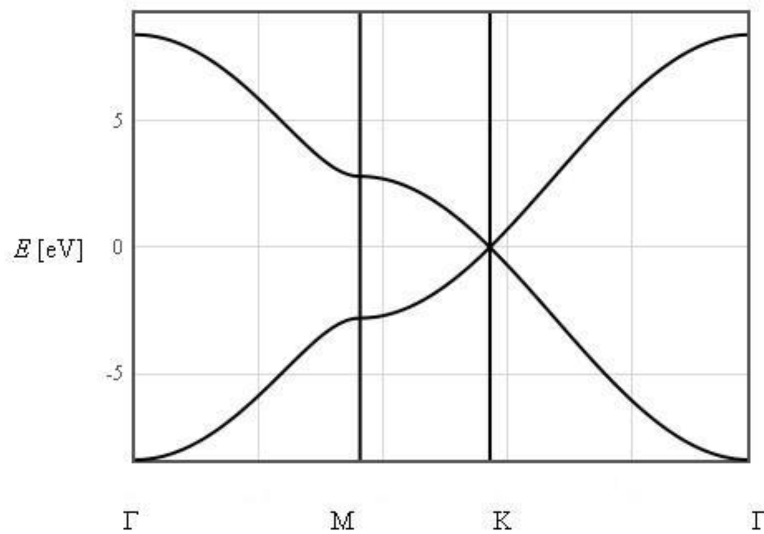

Figure 1.8. The dispersion relation near graphene's K point is found to be linear. Adapted from Ref [11].

1.4 Carbon Nanotube Band Structure

Since single wall carbon nanotubes can be viewed as a single sheet of graphene rolled into a cylinder, we can make use of the above derived dispersion relation for graphene and a technique known as zone folding in or to find the dispersion relation for single wall carbon nanotube. Qualitatively, we obtain this by using a periodic boundary condition in the circumferential direction for the nanotube. This leads to the associated wave vector becoming quantized in that direction, while the wave vector associated with the nanotube axial direction remains infinite (if we assume the nanotube has infinite length). The energy bands created are a set of one-dimensional energy dispersion relations that are cross sections of the dispersion relation we found for graphene above.

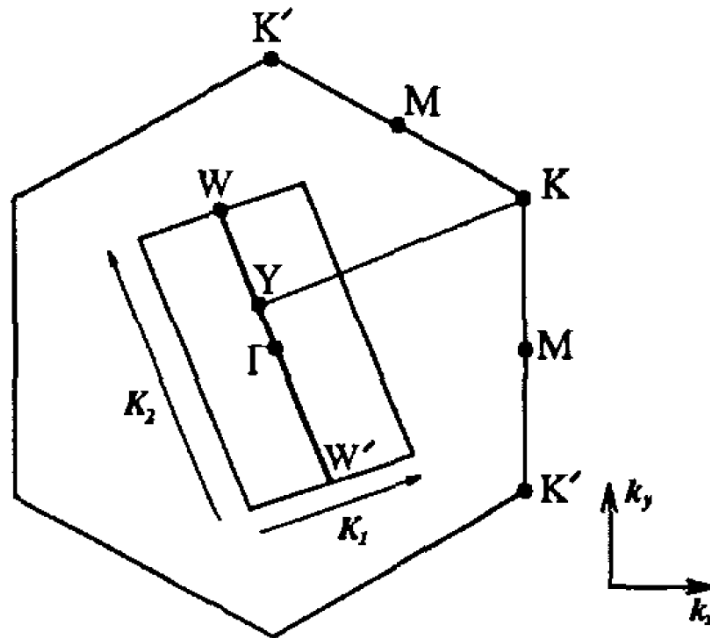

Figure 1.9. Reciprocal lattice of graphene. The reciprocal lattice vectors are given by K_1 and K_2 and the line segment WW' is the first Brillouin zone of a one-dimensional nanotube. Adapted from Ref [[12]].

In practice, we begin by considering the reciprocal lattice, shown in Fig. 1.9, where the reciprocal lattice vectors are given by K_1 and K_2, and the line segment WW' is the first Brillouin zone of a one-dimensional nanotube. When the dispersion relations in

graphene (Eq. 1.1) are folded so that the wave vectors parallel to K_2 coincide with WW' when shifted from WW' by μK_1, where $\mu = 0, \ldots, N-1$, N pairs of one-dimensional dispersion relations, E_{CNT}, are obtained. While not discussed in detail here, N is the number of hexagons per unit cell of a nanotube, or in other words, the area of a nanotube's unit cell divided by the area of a hexagon. These one dimensional energy dispersion relations are given by[12]:

$$E_{CNT}(k) = E_g\left(k\frac{K_2}{|K_2|} + \mu K_1\right) , \qquad \mu = 0, \ldots, N-1, \text{and} -\frac{\pi}{|T|} < k < \frac{\pi}{|T|} \qquad \text{Eq. 1.2}$$

where T is the nanotube's translational vector, which is parallel to the nanotube axis.

The N pairs of energy dispersion relations, given by E_{CNT} in Eq. 1.2, are the one-dimensional cuts in the two-dimensional dispersion surface we found for graphene in section 1.3 where the cuts are along the direction given by $k\frac{K_2}{|K_2|} + \mu K_1$. This is schematically represented in Fig 1.10.

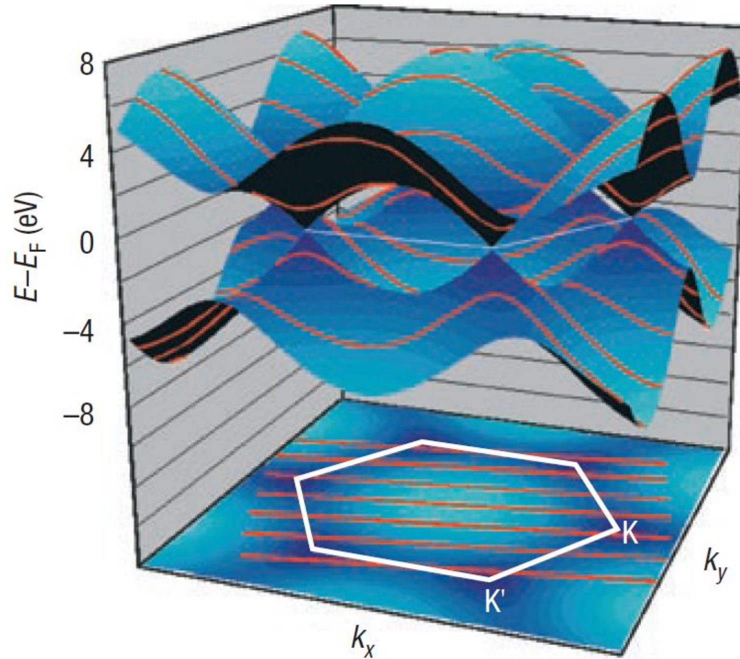

Figure 1.10. Illustration of the zone folding technique. The energy dispersion relation of carbon nanotubes is calculated from the cut lines (shown in red) overlaid on graphene's energy dispersion surface.[13] Reprinted by permission from Macmillan Publishers Ltd: Nature Nanotechnology (Vol. 2), © 2007

Recall that at graphene's K-points, there is zero energy gap. Therefore when a particular nanotube has a cut line that passes through a K point, the nanotube is metallic. All other nanotube are semiconducting to varying degrees. The way a nanotube is wrapped into a cylinder, or its chirality, ultimately determines this so it would be instructive to review this characteristic of carbon nanotubes and will the topic of the following section.

1.5 Chirality in Carbon Nanotubes

As mentioned, the structure of a single wall carbon nanotube can be conceptually viewed as a single sheet of graphene wrapped up as a cylinder. Incredibly, the electronic properties of these nanotubes are determined by the way they are wrapped, which is referred to as their chirality. This convention can easily be understood through the schematic in Fig. 1.11. Here, a_1 and a_1 are the unit vectors of the graphene lattice and the square represents the graphene area that is to be wrapped into a tube. T represents the direction of the resulting nanotube's axis while $C_h = na_1 + ma_2$ is the wrapping vector that determines the chirality of the nanotube.

There are a few special cases that are commonly referred to when characterizing nanotubes. The first is when $n = m$. This results in what is called an armchair nanotube and these nanotubes are always conducting, or metallic. Another special case is when $m = 0$. These nanotubes are referred to as zigzag nanotubes and are typically semiconducting, along with all other nanotube chiralities, with moderate band gaps. And in the case where $n - m$ is a multiple of 3, these nanotubes would be semiconducting with very small band gaps. There are a few exceptions to these rules, such as when nanotube diameters become very small, but these will not be discussed here.

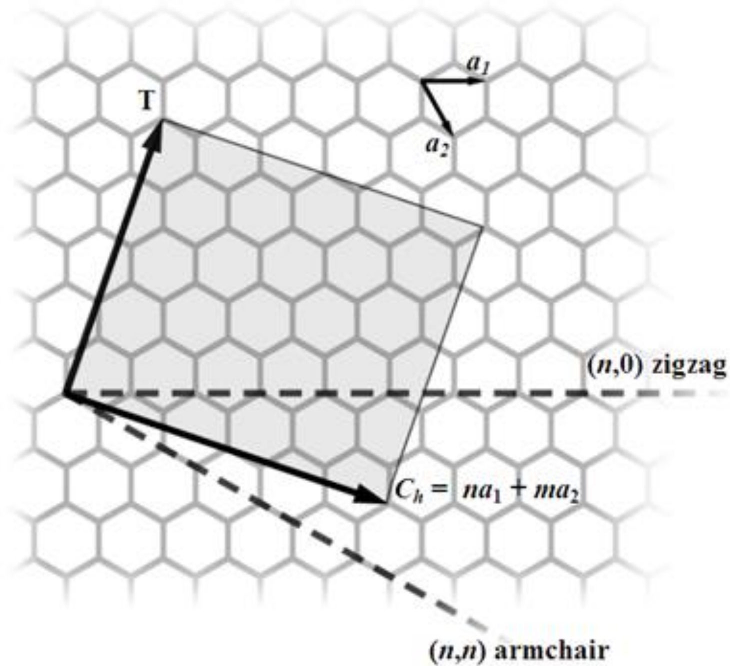

Figure 1.11. Schematic diagram illustrating a carbon nanotube's chirality. Here, a_1 and a_1 are the unit vectors of the graphene lattice and the square represents the graphene area that is to be wrapped into a tube. T represents the direction of the resulting nanotube's axis while C_h is the wrapping vector that determines the chirality of the nanotube. Adapted from Ref. [14]

1.6 Electron Transport

In chapter 6, I will be presenting my work modeling the heat generation and dissipation in a nanowire field-effect transistor. In this work, an analytical closed-form diffusive model is developed of Joule heating in a device consisting of a nanowire connected to two contacts on a substrate. This analytical model is compared to finite-element simulations and demonstrates excellent agreement over a wider range of system parameters in comparison to other recent models. There were particularly large improvements in cases when the width of the nanowire is less than the thermal healing length of the contacts and when the thermal resistance of the contact is appreciable relative to the thermal resistance of the nanowire. The success of this model is due to more accurately accounting for the heat spreading within the contact region of a device and below the nanowire into a substrate. Additional features of this model are the ability to

incorporate contact resistances that may be present at the nanowire-contact interfaces, as well as accommodating materials with a linear temperature-dependent electrical resistivity.

In chapters 3 and 4, I will present my work on the successful integration of few-layer graphene (FLG), carbon nanotubes, and etch tracks exposing SiO_2 into nanoscale systems with precise crystallographic orientations. Specifically, CNTs are grown across nanogap etch tracks and nanoribbons formed within FLG films as a result of chemical vapor deposition (CVD) processing. Due to the fact that these three nanoscale components align along specific directions of a single-FLG lattice, their relative orientations are locked into precise values. This provides a potential route to achieve precise orientation of conductors, insulators, and semiconductors with nanoscale intricacy. In the systems presented, the graphene film that is cut by an etch track into two electrically isolated regions could potentially act as the conducting source and drain electrodes, while the bridging nanotube(s) that are crystallographically aligned to the electrodes on either side would ideally act as a semiconducting channel.

It is well known that carbon nanotubes and graphene can exhibit ballistic conduction.[1,15] It is also predicted that there would be greatly enhanced electron transmission between two sp^2 carbon lattices that are in commensurate contact with each other.[16] Therefore systems such as the ones I present hold the exciting promise of providing a means to fabricate highly efficient, ballistic FET transistors with dimensions significantly smaller than current lithographic capabilities allow.

Due to the nature of these two works, it is important to briefly overview the theory behind diffusive and ballistic electron transport.

1.6.1 Diffusive Transport

For this discussion, consider a typical transistor device with a semiconducting channel and metallic electrodes. In general the flow of charge carriers (assume electrons in this case) through the channel is impeded due to scattering. This scattering can occur due to numerous sources including the repulsion between electrons, acoustic and optical phonons, impurities, defects, and boundaries, and results in diffusive electron transport.

Based on the contributions from each source, the average distance an electron can travel before being scattered, or its mean free path, is approximated by Matthiessen's Rule:

$$\frac{1}{\lambda_{MFP}} = \frac{1}{\lambda_{el-el}} + \frac{1}{\lambda_{ap}} + \frac{1}{\lambda_{aop}} + \frac{1}{\lambda_{eop}} + \frac{1}{\lambda_i} + \frac{1}{\lambda_d} + \frac{1}{\lambda_b}$$

where λ_{el-el} is the electron-electron scattering length, λ_{ap} is the scattering length due to acoustic phonons, λ_{aop} is the scattering length due to the absorption of optical phonons, λ_{eop} is the scattering length due to the emission of optical phonons, λ_i is the scattering length due to impurities, λ_d is the scattering length due to defects, λ_b is the scattering length due to boundaries, and λ_{MFP} is the total electron mean free path.[17]

The mean free path of bulk conductors at room temperature is typically on the order of a few tens of nanometers or less. When the dimension of the medium an electron is traveling through is longer than the electron's mean free path, $L > \lambda_{MFP}$, charge transport in that medium is said to be in the diffusive regime. Therefore channel length is a critical parameter in the performance of transistor devices, as diffusive charge transport results in increased electrical resistance in the channel, leading to reduced device performance due to increases in power consumption, heat generation, electrical noise, and latency.

It is of interest to note that in traditional materials used for current thin film devices, such as silicon, surface scattering effects can also significantly increase the electrical resistance of the channel when the channel's width and thickness are on the order of or less than the mean free path of the charge carriers.

1.6.2 Ballistic Transport

In ballistic conduction, charge carriers travel unimpeded over relatively long distances. With respect to the hypothetical FET we are considering, electron transport in the device is in the ballistic transport regime when the mean free path is significantly longer than the channel's length, $L \ll \lambda_{MFP}$. Fabrication of devices operating in this regime can be achieved through the reduction of the channel length and/or using novel materials such as graphene and nanotubes, which have exhibited electron mean free path length of hundred or nanometers or even microns.[18,19]

In such devices, and when the charge carriers remain coherent, the conductance in the channel is described by the Landauer formula,

$$G = \frac{2e^2}{h} \sum_{i,j} T_{ij}(E_F)$$

where e is the elementary charge, h is the Planck constant, and T_{ij} is the transmission probability for electrons to travel through the ballistic conductor, across all conduction channels, between the Fermi levels E_F of two electrodes. If we assume that the transmission probability for all conduction channels are the same, the above expression can be more simply expressed as

$$G = \frac{2e^2}{h} TM$$

where

$$T = \sum_{j} T_{ij}(E_F)$$

and M is the number of quantum conduction channels.

As an illustration of the large differences in conductance that occur between devices that exhibit ballistic transport and those that exhibit diffusive transport, we first consider a device utilizing a metallic single wall carbon nanotube. In the nanotube there are two quantum conduction channels, with each channel able to accommodate two electrons of opposite spin, making $M = 2$ in the above equation.[20] If there is no backscattering of electrons along the nanotube and there is no reflectance at the nanotube-electrode interfaces, the transmission probability $T = 1$. This results in a value for the conductance of

$$G = 1.55 \times 10^{-4}\ S.$$

Now let's consider a transistor made from a conventional material, such as heavily-doped silicon that has a resistivity of $= 1\ \Omega \cdot cm$, and calculate the channel conductance using a conservative geometry based on current fabrication technology. We will assume a channel length of 32 nm, a width of 10 nm, and a thickness of 5 nm. Using equation

$$G = \frac{A}{\rho L}$$

where L is the channel length and A is the channel's cross sectional area, we find a channel conductance of

$$G = 3.33 \times 10^{-7}\ S$$

which is over two orders of magnitude less than the conductance we found for the device utilizing a carbon nanotube. From this alone, it is clear to see the current interest in further developing technology that utilizes ballistic transport.

1.7 Contact Resistances

Not mentioned in the above discussion of using graphene and carbon nanotubes in future nanoscale devices is the importance contact resistances. In the previous example, we naïvely assumed that there was no contribution to the overall device resistance from the interfacial regions between the carbon nanotube and the source and drain electrodes. In fact, engineering these devices with minimal contact resistances is an area of current technological challenge and interest.[21]

When two metals are brought into direct contact, an ohmic contact is typically formed between them. This type of junction is a non-rectifying junction, meaning charge is free to flow in both directions with very little resistance between the two materials. These are referred to as ohmic contacts because the electrical junction between the two materials obeys Ohm's law and has a linear current-voltage curve.

Any type of contact of junction that does not exhibit a linear current-voltage curve is called a non-ohmic contact. Often at a metal-semiconductor junction, a rectifying potential energy barrier known as a Schottky barrier is formed. This happens due to the fact that when a metal is brought into contact with a semiconductor, the wavefunction of an electron in the metal must match the wavefunction of an electron in the semiconductor at the interface. This boundary condition is met through band-bending, which forces what are known as metal-induced gaps states to occur in the semiconductor near the interface at

energies that, in the bulk of the semiconductor, are forbidden. Charge is then exchanged between the two materials and a rectifying energy barrier is formed.

This effect is especially relevant to the fabrication of graphene and carbon nanotube devices that are to be contacted by metallic electrodes. In such devices, there are two barriers formed: one at the source electrode and another at the drain electrode. Using traditional doping techniques, such substitutional doping of boron or phosphorus, to engineer ohmic contacts has not been successful in these one- and two-dimensional systems thus far. However, other approaches have achieved some success.[13]

A different type of doping method, one in which atoms or molecules were selectively adsorbed near each of the contact regions in carbon nanotube devices while using a central gate, was successful in improving device operation. Another method has utilized a double gate geometry where one gate was used to selectively thin the Schottky barriers and the other was used to control the gate voltage local to the channel. Other methods that are also being currently explored include reducing the channel width, using wrap-around gates to increase the gate coupling in a device, and the utilization of high-k dielectrics.[13] In later chapters, nanostructures comprising a carbon nanotube channel contacted, in crystallographic alignment, with two graphene electrodes will be presented. As previously mentioned, enhanced electrical coupling between such devices is expected and should lead to significantly reduced contact resistance. In these low-dimensional systems where lattices are commensurate, the typical junction band bending phenomena as previously mentioned are not necessarily relevant, as the conservation of crystal momentum is nontrivial needs to be taken into account.

One additional source of contact resistance that is present and unique to these low-dimensional systems making contact with three-dimensional contacts is quantized contact resistance. For example, electrons move through a carbon nanotube confined to one dimension around its circumference. This confinement produces discrete states that overlap the continuous states in metal electrodes. This mismatch between the number of states that can transport charge in the two materials leads to a quantized contact resistance,

$$R_q = \frac{h}{2e^2 M}$$

where M is the number of states in the carbon nanotube that lie between the Fermi levels of the electrodes. For a metallic nanotube, $M = 2$ and results in a quantized contact resistance of 6.45 kΩ.[13]

1.8 Strain-Induced Effects in Graphene

As we have seen, graphene possesses incredible electrical as well as mechanical properties. Though the electrical properties and mechanical properties are each impressive in their own right, in graphene there is a lot of interesting physics to be explored at the interface between these two fields.

Though graphene does not intrinsically possess a band gap, engineering a band gap has been the focus of a large body of research. Techniques include chemical functionalization, laser irradiation, using multiple layers of graphene, and lateral confinement by creating nanoribbons in graphene, each achieving varying degrees of success.

It has recently been reported that a band gap can be opened in graphene through uniaxial strain and physical deformation in the lattice.[22] Surprisingly, it has also been reported that complex strain distributions, such as applying multiple stretch and/or compression directions in graphene, both in and out of the graphene plane, can produce extremely large pseudo-magnetic fields in excess of 10T. This means that not only can energy gaps be opened and increased in graphene through this technique, but the electrons can be made to move in the graphene as though it were exposed to an extremely large external magnetic field. Utilizing the pseudo-magnetic field, it may be possible to induce topological insulator-type behavior in graphene, and well as observing the quantum Hall effect.[23]

Copyright © David Patrick Hunley 2015

CHAPTER 2: Electrostatic Force Microscopy and Electrical Isolation of Etched Few-Layer Graphene Nano-Domains

2.1 Introduction

Few-layer graphene (FLG) is an atomically-thin material having many beneficial properties, such as high carrier mobility, high thermal conductivity, and tremendous strength, which make it a potentially useful material for future nanoscale devices and integrated circuits.[24-30] To achieve this goal of utilizing FLG in nano-electronics requires the ability to construct nanoscale structures out of it.[24] To date there have been a number of approaches investigated to achieving nanoscale FLG.[31-48] One such approach which has received attention is the catalytic etching of few-layer graphene.[49] This catalytic etching has long been known to result in crystallographically-defined etched domains and tracks in bulk graphite.[50] It has recently been found that many of the remarkable etch patterns obtained within bulk graphite persist to the FLG domain as well[49] -- even when the films are supported on amorphous insulating substrates.[49,51] The fact that the crystallographic etch patterns can be obtained on insulating substrates indicates that catalytic etching could be a way to construct nanoscale electrically-isolated FLG segments useful for devices. While there have been a number of investigations probing the electrical properties of nanostructured FLG,[36,37,52-54] further measurements are required to understand and assess the effects of nanoscale processing and confinement. This is particularly true for nanoscale FLG obtained through catalytic etching that can be difficult to probe due to the close proximity of the nanoscale domains.

Here we use electrostatic force microscopy (EFM) to investigate catalytically-etched bi-layer graphene samples.[55] EFM has recently been used to probe variations of the surface potential of FLG as its thickness varies.[56] In contrast to this previous work, we find an EFM signal that varies significantly between nanoscale FLG domains even though they have the same thickness. We obtain evidence that the change in the EFM response is due to changes in the capacitive coupling as the size of the nanoscale FLG domains is reduced. Furthermore, the fact that the EFM signal changes abruptly in going between adjacent domains gives a lower-bound estimate of their electrical isolation.

2.2 Experimental Details

2.2.1 Sample Preparation

The catalytically etched graphene samples used in this investigation were prepared through mechanical exfoliation onto p^+-doped silicon substrates having a 300 nm thermal oxide layer,[57] followed by processing in a chemical vapor deposition (CVD) furnace.[49,51] Prior to the exfoliation, the substrates were cleaned through ultrasonication in acetone, isopropyl alcohol, then deionized water for 3 minutes each using a Branson 2510 Bransonic Ultrasonic Cleaner. The substrates were then subjected to UV ozone (UVO) cleaning in a NovaScan PSD Series Digital UV Ozone System for 15 minutes. After this, kish graphite was exfoliated onto the substrates, followed by spin coating a 2.4 mg/mL solution of NiCl in water which later forms the nickel catalyst nanoparticles after thermal processing. Samples were then placed in a Thermo Scientific Lindberg Model TF55035C CVD furnace with MKS Type 247D Mass-Flow Controllers where they were annealed at 500° C for 30 min and then immediately heated to 1000° C for 120 min. Throughout the furnace processing, gas flows of 850 and 150 sccm of Ar and H_2, respectively, were maintained. The furnace temperature was increased using a controlled ramp rate of 50° C per min followed by the high-temperature processing, after which the sample was allowed to passively cool to room temperature within the furnace. The processed sample contains FLG flakes which all have etch tracks with varying amounts of additional carbon nanotube (CNT) growth on their surfaces. This variation in CNT growth is likely due to the greater local variations of catalyst material resulting from spin-coating[51] in comparison to evaporation.[58,59] In the investigation that follows we focus in detail on a region of the sample containing only etch tracks with negligible amounts of CNTs grown on top of the FLG.[51,58,59]

2.2.2 EFM Measurements of Graphene

We start with a bi-layer region (as shown in Fig. 1(a)) that has considerable etching and appears, according to atomic force microscopy (AFM), to have several electrically isolated regions. Atomic force microscopy and EFM of the samples were performed with an Asylum Research MFP-3D AFM. The probes used in these measurements were Multi75E-G probes from NanoAndMore USA and have nominal tip radii <25 nm. The EFM method we utilize is a two-pass technique consisting of a conducting tip where the first pass obtains the topography and the second retraces the topography a fixed height of 36 nm above the surface. During the second pass the cantilever is driven close to resonance using the dithering piezo with a fixed applied bias between the tip and the doped Si back-gate substrate while the phase shift of the driven cantilever is measured. Figure 2.1(b) shows such an EFM phase image acquired with a 7 V tip-substrate bias of the same etched bi-layer region as in Fig. 2.1(a). This image clearly shows that the various bi-layer regions have very different phase shifts for a constant bias. This difference in EFM response between electrically isolated bi-layer regions is further demonstrated by investigating the phase response as a function of bias. Figure 2.1(c) shows such a comparison of the phase versus bias for the two regions within the square blocks in Fig. 2.1(b). Both regions show a parabolic phase response having their minima located at the same bias but with different concavities. This EFM behavior is distinct from previous measurements over multilayer graphene which, in contrast, show a constant concavity for such phase plots, but with minima that occur at varying voltages depending on the few-layer-graphene thickness.[56]

2.3 Investigating Nano-Domains in Graphene

The EFM measurements can be understood by approximating the cantilever response as due to a total capacitance (C_T), a surface potential (φ_S), an applied electrochemical potential to the tip relative to back-gate (V_{app}), and a work function difference between the tip and back-gate (ΔW). This provides a force gradient for the tip as a function of its vertical height (z) above the sample that alters the cantilever's resonance frequency.[60] For a cantilever driven at a fixed frequency near its resonance above a

conducting sample surface, the change in the oscillatory phase is related to the force gradient through

$$\Delta\varphi \cong \frac{Q}{k}F'(z_0) = \frac{Q}{2k}\left(V_{app} - \varphi_S - \Delta W\right)^2 C_T''(z_0), \qquad \text{Eq. 2.1}$$

where Q is the oscillator quality factor and k is the effective spring constant. For large-area graphene samples, which are relevant to the experiments in Ref [[56]], the only term which varies appreciably for a constant tip-FLG height and tip material is the surface potential of the FLG which depends on its thickness. This results in nearly identical parabolic phase curves as a function of potential which are displaced according to the varying surface potential of the FLG,[56] in agreement with Eq. (2.1).

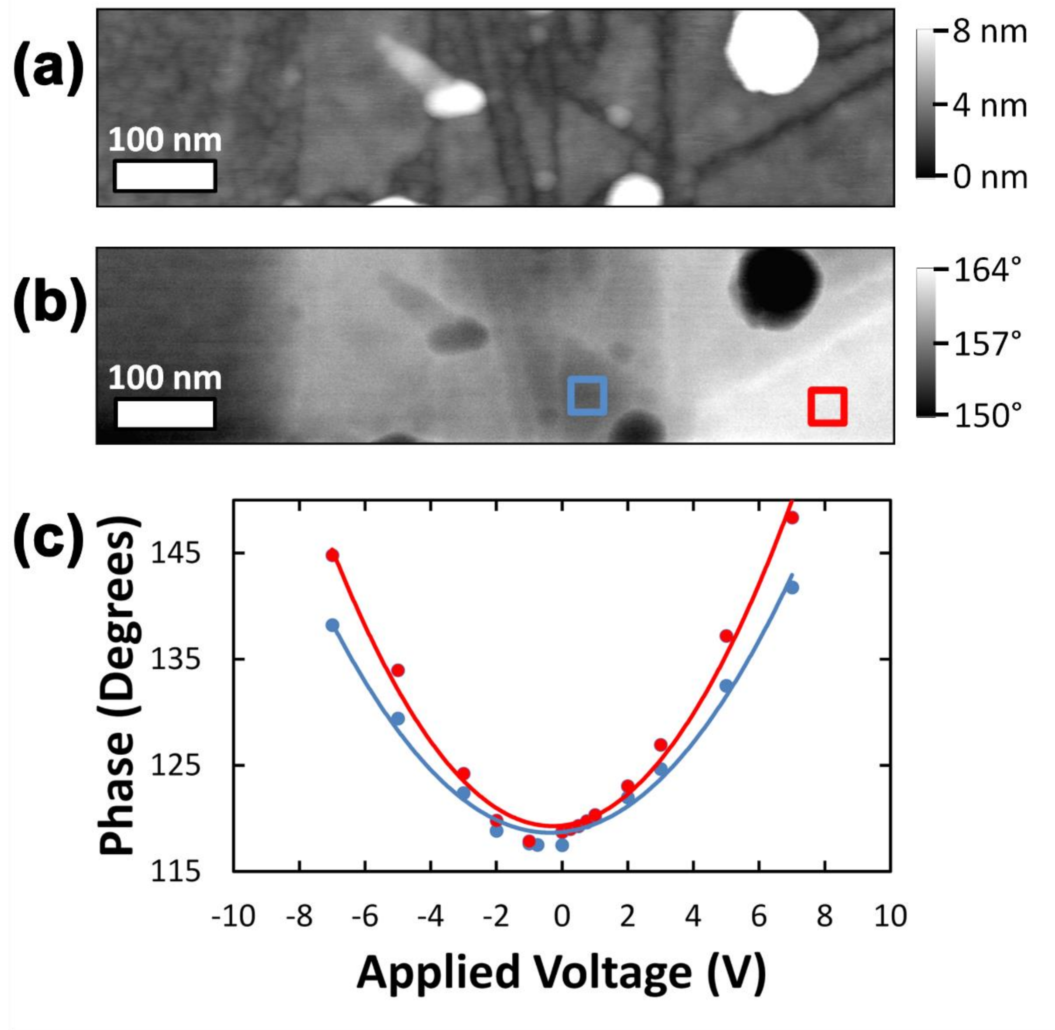

Figure 2.1. (a) Atomic force microscope topography image of a bi-layer graphene (light grey) sample which has been catalytically etched with Ni nanoparticles. The etch tracks down to the insulating SiO_2 are the darker lines, the round white regions are catalyst particles, and the left region is exposed SiO_2 substrate. (b) EFM image of the same region taken at constant 7 V that shows a signal varying for different etched domains. (c) Spatial averages of the signals within the blue and red boxes in (b) at varying applied tip voltages with quadratic fits. The red and blue data and in (c) correspond to the respective red and blue boxed regions in (b).

For the samples considered here, where all the FLG segments are bi-layer, the surface potential is relatively constant for the etched domains, and thus the phase-shift parabolas should all have the same voltage minima. However, different lateral positions above the sample should result in a variation of $C_T''(z_0)$ due to differences in the capacitive coupling to the geometrically varying shapes of etched FLG below. This should result in

parabolic phase-shift curves with different shapes but with minima located at the same voltage, like that shown in Fig. 2.1(c). Since the electrical coupling is strongest between the tip and the FLG directly below it, the geometry of this closest etched domain should make the greatest contribution to the curvature of the phase parabola. Evidence that this effect is the source of the different phase responses observed in Figs. 2.1(b) and 2.1(c) is obtained by plotting the quadratic fitting coefficients of the EFM parabolas as a function of the surface area of the graphene segments below the tip, as shown in Fig. 2.2.

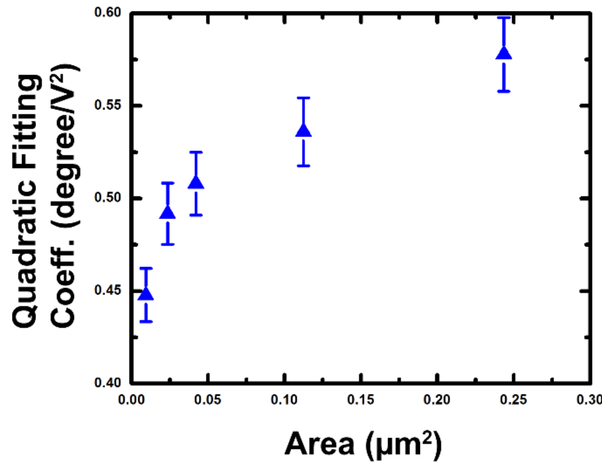

Figure 2.2. The quadratic fitting coefficient of the EFM phase curves plotted against the surface area of the bi-layer graphene domain size directly below the tip (error bars estimated from fits).

2.4 Comparison to Finite Element Simulations

To understand this variation of the quadratic EFM response as a function of area, we have performed finite-element simulations of a tip over various geometrical arrangements of conducting sheets. The simulations were performed with a cylindrically-symmetric arrangement where the tip is located along the central vertical axis of the computational volume, given by a cylinder of height 5300 nm and radius 2820.95 nm. The cylindrical symmetry allows for the simulation of the fields within the entire volume to be simplified to that of a two-dimensional slice that significantly increases the speed and precision of the computations. A back conducting plane is placed on the lower surface of the cylindrical space with various arrangements of FLG domains located 300 nm above it,

as seen in the vicinity of the tip in Fig. 2.3(a). The simulated conducting tip is given a total height of 4260 nm, a realistic radius of curvature of 25 nm and conical opening angle (as measured from the central axis) of 25 degrees, and its end is located a lift height z above the plane containing the FLG domains.

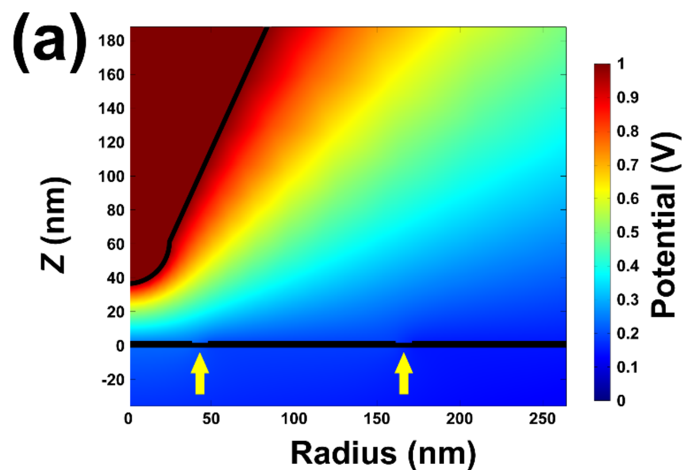
(a)
Z (nm)
Radius (nm)
Potential (V)

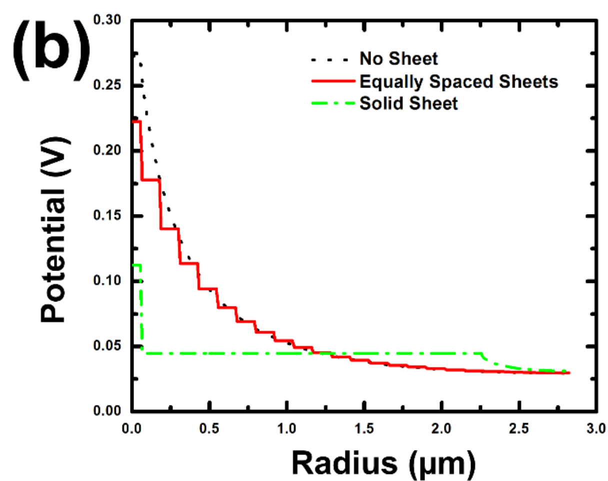
(b)
No Sheet
Equally Spaced Sheets
Solid Sheet
Potential (V)
Radius (μm)

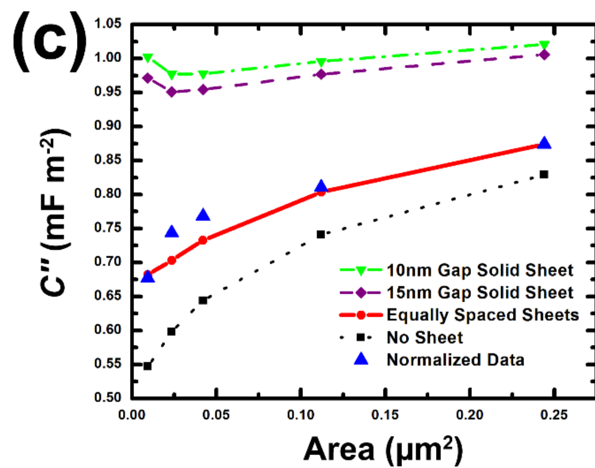
(c)
10nm Gap Solid Sheet
15nm Gap Solid Sheet
Equally Spaced Sheets
No Sheet
Normalized Data
C" (mF m-2)
Area (μm2)

Figure 2.3. Finite element simulations of the electrostatic interactions between the EFM tip and the etched FLG sample. (a) Cross-sectional slice of the simulation in the vicinity of the tip with etched FLG located on the plane $z = 0$. Yellow arrows point to etch tracks and a conducting plane exists at $z = -300$ nm. (b) The potential on the plane $z = 0$ for various FLG arrangements with central one of radius 54.4 nm. 'No Sheet' does not have additional FLG, 'Solid Sheet' has a single surrounding FLG sheet separated with a 10 nm gap and an outside radius of 2251 nm, and 'Equally Spaced Sheets' has a series of FLG rings of width 113 nm each separated by 10 nm. (c) C_T'' determined by the simulations as a function of the area of the domain directly below the tip. The experimental data from Fig. 2.2 is plotted on this curve with a single scaling factor.

The first arrangement we consider consists of a single FLG domain of a specified area separated with a single 10 nm gap from a continuous larger surrounding domain with an outside radius of 2251 nm. The green dot-dashed line in Figure 2.3(b) is the potential distribution along the radial direction of the FLG plane for a tip height of 36 nm resulting in a significant voltage drop across the 10 nm gap. By performing simulations at various tip heights from 32 to 40 nm we are able to estimate C_T'' at $z_0 = 36$ nm. The top dot-dashed green curve in Fig. 2.3(c) shows the results of such a computation as a function of the inner FLG domain area. While there is a clear dependence of C_T''on area, the 4.30% change over this range, defined as $\left({C_T''}_{max} - {C_T''}_{min}\right)/{C_T''}_{max}$, is not sufficient to account for the 22.5% change we observe in our measurements. This discrepancy does not appear to be due to a variation in etch track width, as the use of a 15 nm gap (which is larger than the size determine experimentally through AFM) in the calculations has only a minimal affect on the results, as seen by the purple dashed line in Fig. 2.3(c). In contrast, computations without an outside FLG sheet show a 34.0% change of C_T'' over the same range of areas (plotted as the dotted black curve in Fig. 2.3(c)), which is even greater than experimentally observed. This suggests that the FLG not directly below the tip affects the overall capacitance to an intermediate level between these two extreme scenarios. Direct support for this is obtained by simulating the surrounding etched FLG regions as concentric circular sheets of width 113 nm (*i.e.*, a typical size for an etched domain in these samples) spaced by 10 nm gaps. This results in a 22.0% change of C_T'' shown by the solid red line in Fig. 2.3(c) that is in good agreement with the measured data (plotted as the blue triangles). A radial plot of the potential on the graphene surface for this intermediate scenario (the solid red line in Fig. 2.3b) shows a series of drops at the etched gaps that are

largest close to the tip and that approach the profile without an outside sheet (the black dotted line) away from the tip. This suggests that the domain geometry not directly below the tip gives a non-negligible contribution to the EFM measurements. The scatter of the experimental data off of the simulated curve in Fig. 2.3(c) is likely due to variation in these nearby FLG domain arrangements not directly below the tip. Future experiments using coaxial EFM tips[61] might make it possible to shield the capacitive coupling to only the single closest etched FLG domain.

In the above simulations of C_T'' we have ignored effects due to the cantilever itself which can be important in EFM force measurements.[62,63] This is justified in our EFM force gradient measurements, as is seen by using a parallel-plate approximation for the cantilever,[64] where its width ($W = 28\ \mu$m), length ($L = 225\ \mu$m), and tip height ($h = 17\ \mu$m) are inserted into $C_{cant} = WL\epsilon_0/h$, $C'_{cant} \sim -\frac{WL\epsilon_0}{h^2} = -1.93 \times 10^{-10}$ F/m, and $C''_{cant} \sim 2WL\epsilon_0/h^3 = 2.27 \times 10^{-5}$ F/m^2. Although this C'_{cant} has a larger magnitude than the one we simulate, the estimate of C''_{cant} is only $\sim$3% of the value we compute, and can thus be neglected in the force gradient EFM measurements. In addition, our simulations only take the geometrical aspects of the capacitive coupling in the EFM measurements into account, and neglect the local surface potential. For large area FLG films that provide a surface with a nearly constant surface potential (like in the previous EFM measurements of FLG[56]) the minima of the phase parabola should directly reflect the surface potential. In contrast, when the size of the FLG conducting region is small enough such that the tip appreciably couples directly to the back conducting plane, the phase minimum will not in general be directly related to the surface potential of the conducting FLG film.

2.5 Modeling Resistance between Isolated Nano-Domains

The fact that the EFM phase response changes abruptly for adjacent etched bi-layer graphene segments in Fig. 2.1 permits a lower estimate of the resistive barriers provided by the etch tracks. For the etched system to act as electrically separated conducting FLG domains that maintain the voltage drops seen in Fig. 2.3(b), the resistance between them must be large enough to prevent their electrical equilibration over the time scale probed by

EFM. Thus, the RC time scale for electrical equilibration must be greater than the characteristic EFM probing time (τ) of the experiments as represented by the simplified two-capacitor circuit model in Fig. 2.4. In this model, the EFM probe is positioned over the first FLG domain (G_1) such that the tip only appreciably couples to it. An adjacent etched domain (G_2) having an overall different capacitive coupling to the environment is connected to G_1 through possible parasitic residual conductance across the etch tracks. Using this model, it can be shown that when either the scan time (the time over which the tip is located above a particular domain) or the oscillation time of the cantilever is less than the RC equilibration time that abrupt changes in EFM signal are possible in switching the location of the tip between G_1 and G_2.

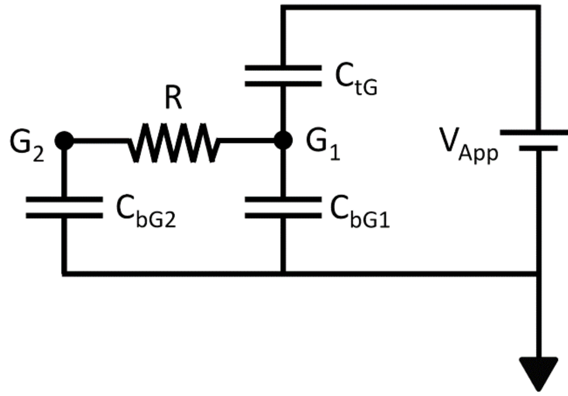

Figure 2.4. A simplified circuit diagram that approximates the electrostatic force microscopy measurement when the tip is over one nano-domain (G_1) and is separated by an etch track to another domain (G_2). In the model, the tip-graphene capacitance to a domain is C_{tG}, the two capacitances to the environment are C_{bG1} and C_{bG2}, and the parasitic conductance between the two domains is represented by the resistor R.

2.6 Relevant Time Scales

Here we consider the relevant time scales in EFM measurements using the simplified RC circuit model in Fig. 2.4. In this model we will assume that the only capacitance which varies as the tip height ($z = z_0 + \Delta z$) changes is $C_{tG} = \frac{A\epsilon_0}{z}$, where we have simplified the tip graphene interaction as a parallel plate capacitor. While this is an oversimplification, this model captures the relevant time scales probed by the EFM

measurements. In this model, z_0 is the average height of the tip, Δz is the change in its height due to the oscillation, and A is the area of the tip capacitor in this simplified model.

We will consider the relationships between the two measurement time scales and the RC equilibration time constant (τ_{RC}) of the two-FLG domain system. The two measurement time scales are the scan time (τ_s), which is the time that the tip is over a specific FLG domain, and the oscillation time (τ_{osc}), which is the period of oscillation of the tip. For EFM measurements we generally have $\tau_s > \tau_{osc}$ so that changes in the resonance properties due to electrostatic interactions over different FLG domains can be discerned from each other. Thus, there are only three cases to consider for the time scales: (1) $\tau_s > \tau_{osc} > \tau_{RC}$, (2) $\tau_{RC} > \tau_s > \tau_{osc}$, and (3) $\tau_s > \tau_{RC} > \tau_{osc}$. To address these three cases, we will assume that initially both FLG domains (G_1 and G_2) are charge neutral before the tip approaches. When the tip is over one of the domains, we will also assume that it couples only to that domain with a value of $C_{tG} = \frac{A\epsilon_0}{z}$. To gain insight into the time scale relations and equilibration of the domains, it is useful to consider the force on the tip as due to the charge density (σ) on its surface. This gives a force on the tip of $F = -\frac{\sigma^2}{2\epsilon_0}A$.

Case 1: $\tau_s > \tau_{osc} > \tau_{RC}$

In this case the equilibration between the two capacitors C_{bG1} and C_{bG2} is much faster than any changes from the probe, so the resistor acts as a short. This gives for the charge density on the capacitor C_{tG},

$$\sigma = V_{App}\left\{\frac{z_0+\Delta z}{\epsilon_0} + \frac{A}{C_{bG1}+C_{bG2}}\right\}^{-1}, \qquad \text{Eq. 2.2a}$$

and a resulting force gradient of,

$$F'(z_0) = \left(\frac{\partial F}{\partial(\Delta z)}\right)_{\Delta z=0} = \frac{\left(V_{App}\right)^2}{(A\epsilon_0)^2}\left\{\frac{1}{C_{tG0}} + \frac{1}{C_{bG1}+C_{bG2}}\right\}^{-3}. \qquad \text{Eq. 2.2b}$$

The relation for when the tip is located over $G2$ can be obtained by exchanging C_{bG1} and C_{bG2} in Eq. 2.2a above. By performing the exchange $C_{bG1} \Leftrightarrow C_{bG2}$, this relation for the force gradient remains the same – indicating that abrupt changes to the EFM measurement in going between adjacent domains *do not occur*.

Case 2: $\tau_{RC} > \tau_s > \tau_{osc}$

In this case the resistor acts like an open in the circuit, so that we can completely remove C_{bG2} from the derivation, which yields the following relations for the charge density,

$$\sigma = V_{App}\left\{\frac{z_0+\Delta z}{\epsilon_0} + \frac{A}{C_{bG1}}\right\}^{-1}, \qquad \text{Eq. 2.3a}$$

and for the force gradient,

$$F'(z_0) = \frac{\left(V_{App}\right)^2}{(A\epsilon_0)^2}\left\{\frac{1}{C_{tG0}} + \frac{1}{C_{bG1}}\right\}^{-3}. \qquad \text{Eq. 2.3b}$$

However, in this case performing the exchange $C_{bG1} \Leftrightarrow C_{bG2}$ in Eq. 2.3b gives different functions – indicating that abrupt changes to the EFM measurement in going between adjacent domains *can occur*.

Case 3: $\tau_s > \tau_{RC} > \tau_{osc}$

In this case we must consider a constant charge on C_{tG} given by $Q_t = Q_1 + Q_2$ due to equilibrium being setup due to long scan time, where Q_1 and Q_2 are respectively the charges on the capacitors C_{bG1} and C_{bG2}. The movement of the tip occurs too fast to allow appreciable charge to flow through the resistor, so under changes of Δz we have $Q_t = Q_1 + q_1 + Q_2$, where the Q_1 and Q_2 are the same values obtained with the tip fixed while q_1 is an additional charge exchanged between C_{bG1} and C_{tG} consistent with V_{App}. This gives the following results,

$$\sigma = V_{App}\left\{\frac{z_0+\Delta z}{\epsilon_0} + \frac{A}{C_{bG1}}\right\}^{-1}\left(1 + \frac{AC_{bG2}}{C_{bG1}(C_{bG1}+C_{bG2})}\left\{\frac{z_0}{\epsilon_0} + \frac{A}{C_{bG1}+C_{bG2}}\right\}^{-1}\right), \qquad \text{Eq. 2.4a}$$

and,

$$F'(z_0) = \frac{\left(V_{App}\right)^2}{(A\epsilon_0)^2}\left\{\frac{1}{C_{tG0}} + \frac{1}{C_{bG1}}\right\}^{-3}\left(1 + \frac{C_{bG2}}{C_{bG1}} \cdot \frac{C_{tG0}}{C_{tG0}+C_{bG1}+C_{bG2}}\right)^2. \qquad \text{Eq. 2.4b}$$

In this case, performing the exchange $C_{bG1} \Leftrightarrow C_{bG2}$ in Eq. 2.4b also gives different functions – indicating that abrupt changes to the EFM measurement in going between adjacent domains *can occur*.

A specific example demonstrating that abrupt changes are possible is for a case where $C_{tG0} \ll C_{bG1} \ll C_{bG2}$, which yields the following approximate solutions for the tip over the two domains,

$$[F'(z_0)]_{G1} \approx \frac{(V_{App})^2}{(A\epsilon_0)^2}(C_{tG0})^3\left[1 - \frac{C_{tG0}}{C_{bG1}}\right], \qquad \text{Eq. 2.5a}$$

and,

$$[F'(z_0)]_{G2} \approx \frac{(V_{App})^2}{(A\epsilon_0)^2}(C_{tG0})^3\left[1 - 3\frac{C_{tG0}}{C_{bG2}}\right] \approx \frac{(V_{App})^2}{(A\epsilon_0)^2}(C_{tG0})^3. \qquad \text{Eq. 2.5b}$$

Thus, for abrupt changes in the EFM force gradient measurement to be observed, τ_{RC} must be larger than either τ_s or τ_{osc}. Since in general $\tau_s > \tau_{osc}$, a conservative lower-bound choice of the relevant measurement time scale for detecting abrupt changes to the EFM measurement is $\tau = \tau_{osc}$, as is used in the next section.

2.7 Lower-Bound Estimate of Etch-Track Resistance

To obtain a lower-bound of the etch-track resistance we use the shortest of these scales, which is the oscillation time and is given by $\tau = 2\pi/\omega_0$, where ω_0 is the resonance frequency of the 67.461 kHz probes. The capacitance of a domain consisting of an outside perimeter of $l = 342$ nm is estimated as 1.41×10^{-17} F by using the simulations discussed above in Fig. 2.3 consisting of equally-spaced sheets. The resistance between etched segments is given by $R = \rho_{gap}/l$, where ρ_{gap} is the resistivity of the gap (and not a bulk resistivity despite the similar units) which yields the entire resistance across it when divided by its length, l. A lower-bound to the gap resistivity can therefore be estimated from the RC time-constant using the above values to obtain $\rho_{gap} \gtrsim l\tau/C = 3 \times 10^{14}\ \Omega \cdot \text{nm}$. This extremely large gap resistivity indicates that the samples we have synthesized yield electrically isolated bi-layer regions.

2.8 Conclusions

In conclusion, we have made an EFM investigation of nanostructured bi-layer graphene samples that are formed by catalytic etching along narrow (approximately 10 nm wide) tracks. The measurements show a variation in the quadratic term of the EFM phase signal for different nano-domains of bi-layer graphene. Quantitative comparison to simulations indicates that the change in quadratic behavior is due to a decrease in the second derivative of the overall capacitive coupling as the closest nano-domain becomes smaller. The fact that abrupt capacitance variations can be measured across etch tracks indicates that the nano-domains have strong electrical isolation. Modeling the system as a RC circuit permits a lower estimate of the electrical isolation between etched nano-domains. This calculation gives a lower-bound estimate to the gap resistivity of $3 \times 10^{14}\ \Omega \cdot$ nm between two bi-layer graphene regions separated by an approximately 10 nm wide etch track. This extremely large gap resistivity suggests that catalytic etch tracks within FLG samples are sufficient for providing electrical isolation between separate nano-domains that could permit their use in constructing atomically-thin nanogap electrodes,[44,47,65] interconnects,[52,54] and nanoribbons.[36,53]

Copyright © David Patrick Hunley 2015

CHAPTER 3: Crystallographically Aligned Carbon Nanotubes Grown on Few-Layer Graphene Films

3.1 Introduction

Carbon nanotubes (NTs) and graphene have tremendous potential for future nanoscale applications due to their remarkable physical properties, such as high carrier mobility and mechanical strength.[12,66] To realize the potential of these two closely related materials, both comprising sp^2-bonded honey-comb structured carbon sheets, significant improvements to the crystallographic control over their construction, orientation, and placement at the nanoscale are required.[67] Towards this goal, a number of techniques have been utilized to precisely control the orientation and placement of NTs, such as aligned growth utilizing atomic step-edge templates,[68,69] single-crystal templates,[70-72] flow-alignment,[73,74] electric-field alignment,[75] and combinations of the above techniques yielding novel structures such as serpentines.[76-78] Crystallographic nanoscale control over the construction of graphene and few-layer graphene (FLG) structures has seen progress through nano-lithographic methods,[36] crystallographic catalytic etching,[49,51,79] etch masks made from nanowires and metallic nanojunctions,[33] localized etching with scanning probes,[80,81] ultrasonication,[38,82] and plasma etching of NTs.[39,45] Additional recent efforts in precision nanofabrication have been directed towards the goal of directly growing NTs from carbon sources, such as graphene oxide[83] and reduced graphene oxide,[84] without the need of a feedstock gas. Although NTs have been shown to have a chirality dependent adhesion to graphene,[85] most previous investigations focused on the interactions between NTs and graphene in its bulk graphite form;[86-96] with some of this work showing that NTs grown through laser ablation can be oriented along specific bulk graphite crystal axes.[93]

Here we report the growth of NTs on FLG films using catalytic chemical vapor deposition (CVD) without a carbon feedstock gas. We find that NTs grow along specific crystallographic orientations of the FLG films. Moreover, this crystallographic alignment becomes significantly more pronounced on thinner films that are less than approximately 6 atomic layers thick.[97] The orientations of the NTs are 30° offset from crystallographic etch directions occurring in graphene,[49,50,98] indicating that the NTs lie along the armchair

directions of the FLG lattice. A striking feature of the NTs on FLG is that they make occasional abrupt 60° or 120° changes in direction along the other armchair orientations. These abrupt changes in crystallographic direction also occur when NTs encounter one another, which is indicative of a tip-growth mechanism along the surface of the FLG.

3.2 Experimental Details

Crystallographically aligned NTs on FLG samples were prepared on p^+-doped silicon substrates having a 300 nm thermal oxide layer. The substrates were ultrasonicated in acetone, isopropyl alcohol, and deionized water for 3 minutes each using a Branson 2510 Bransonic Ultrasonic Cleaner. The substrates were then subjected to UV ozone (UVO) cleaning for 15 minutes in a NovaScan PSD Series Digital UV Ozone System. Highly-ordered pyrolytic graphite (HOPG) was then mechanically exfoliated onto the substrates.[57] Catalyst material was deposited onto the substrate using electron-beam evaporation of a nominally 0.2 angstrom thick film of Ni to form catalyst particles. Samples were then placed in a chemical vapor deposition (CVD) furnace (Thermo Scientific Lindberg Model TF55035C) with a gas flow of 850 and 150 sccm of Ar and H_2 (determined with MKS Mass-Flo Controllers with MKS Type 247D Four-Channel Readout), respectively, where they were annealed at 500° C for 30-60 min and then immediately heated to 900° C for 60 min in order to grow the NTs. Temperatures were achieved in both steps using a controlled ramp rate of 50° C per min. Immediately following the growth period, the samples were allowed to cool to room temperature.

Control experiments were performed in the slightly modified (from above) gas flows of 700 sccm Ar and 150 sccm H_2 in order to determine the effects of a 2500 sccm CH_4 feedstock gas. Two sets of control samples were prepared; with and without an additional tape residue removing step performed prior to Ni evaporation. The tape residue removal was performed in the CVD system at 400° C for 1 hour with a gas mixture of 340 sccm Ar and 380 sccm of H2.

AFM height measurement, imaging, and nanomanipulation were performed with an Asylum Research MFP-3d AFM. AFM height measurment and imaging were performed in intermittent contact mode. Nanomanipulation of NTs was performed in

contact mode using the Asylum Research MicroAngelo™ nanolithography and nanomanipulation package.

SEM imaging was performed with a Zeiss Supra 35 field-emission SEM with a Gemini Column. Raman spectroscopy measurements were performed with a Renishaw 100 confocal micro-Raman system with a CCD detector, 633 nm excitation of HeNe laser was focused to ~1 □m spot size with a 100x objective. Spectra were acquired using a 60 second integration time.

Histogram analysis was performed by first digitizing the locations of NTs and/or etch tracks with the use of a MatLab code we developed. This code allows us to trace over a digital image of NTs and etch tracks with a series of short straight lines down to approximately 1 nm in length. The code stores the length, direction, and position of each NT and etch track within an analyzed region. Histograms are generated by summing the total length for all the lines that fall within a specific angular bin.

3.3 Results of Nanotube Growth Process

Figure 3.1 shows a scanning electron microscopy (SEM) image of NTs grown on a FLG film ~1.0 nm thick (region "A" in the figure), as measured by atomic force microscopy (AFM). The lines in Fig. 3.1 are NTs which were grown at the elevated temperatures inside the CVD furnace with an Ar and H_2 gas mixture without the need for a carbon feeding gas (see details in Methods section below). Unordered NT growth on FLG without feeding gas at elevated temperatures has previously been attributed to residual carbon on the sample surface.[51,99] In contrast to this previous work, our cleaning and catalyst preparation methods promote crystallographically-oriented NT growth on FLG samples. Control experiments utilizing an additional methane feedstock gas show inhibited NT growth on the FLG and long NTs only on the exposed SiO_2 substrate. Removal of tape residue using a 400° C furnace cleaning step prior to catalyst evaporation[100] and using a pristine CVD quartz tube make negligible differences to the amount of NT growth, indicating that the carbon source originates from the FLG and graphite exfoliated onto the wafer. In addition, the NTs in the figure each have a single bright spot at one end, which is likely a catalyst particle. The NT diameters are in the 4 nm to 10 nm range, as determined

by AFM measurements. Also evident in Fig. 3.1 are etch tracks formed through catalytic hydrogenation of the FLG film.[49]

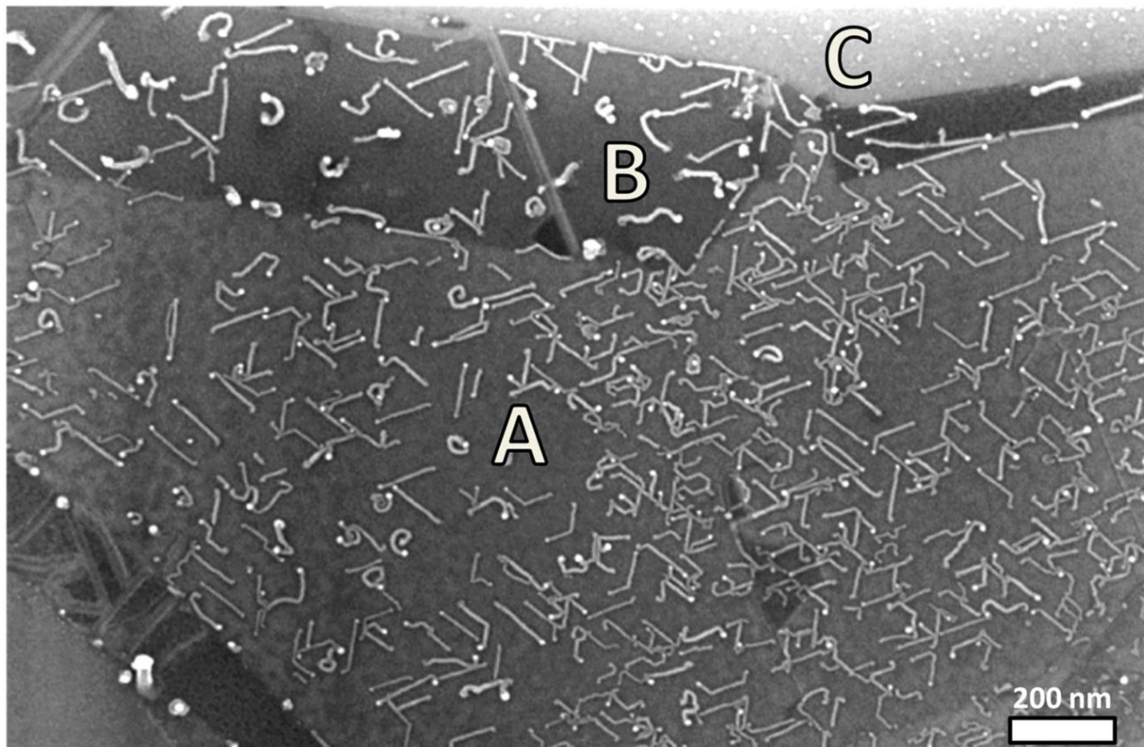

Figure 3.1. SEM image of NTs aligned to the crystallographic axes of FLG. The region exhibiting the most crystallographic alignment, labeled A in the figure, is ~ 1.0 nm thick as measured by AFM. The thicker region, labeled B, is ~2.5 nm thick and produced fewer and less aligned NTs than region A. Region C is an exposed portion of the underlying SiO_2 substrate.

3.4 Determination of the Crystallographic Direction of Growth

To determine the crystallographic orientation of the NTs, we statistically analyzed their growth on a ~ 0.4 nm thick FLG flake (Fig. 3.2). This sample contains a significant number of etch tracks and NTs which permit a statistical analysis of their orientations. Figure 3.2a shows an AFM phase contrast image of the sample, which serves to simultaneously determine the orientation and position of both the NTs and the etch tracks. In this phase image, NTs have a greater contrast on the graphene than the etch tracks, while the etch tracks appear as the longer, fainter lines. Figure 3.2b shows histograms of the total

lengths of all NTs (solid blue line) and etch tracks (dashed red line) in Fig. 3.2a versus angle. Each of these histograms show a series of distinct peaks at 60° intervals, with the two sets offset by 30°. Since nickel catalyst particles have long been known to etch graphite predominantly along the zigzag axes,[50] for track widths like those in Fig. 3.2 which are in the majority ~10 nm or greater,[79,98] we deduce that NT formation is mostly occurring along the armchair directions. Future ultra-high resolution electron microscopy of suspended nanotube on FLG samples would be particularly useful to independently confirm and elucidate their crystallographic characteristics.

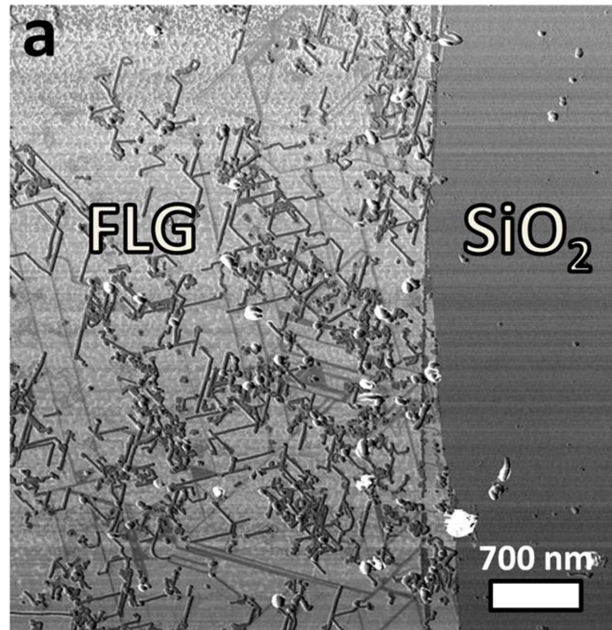

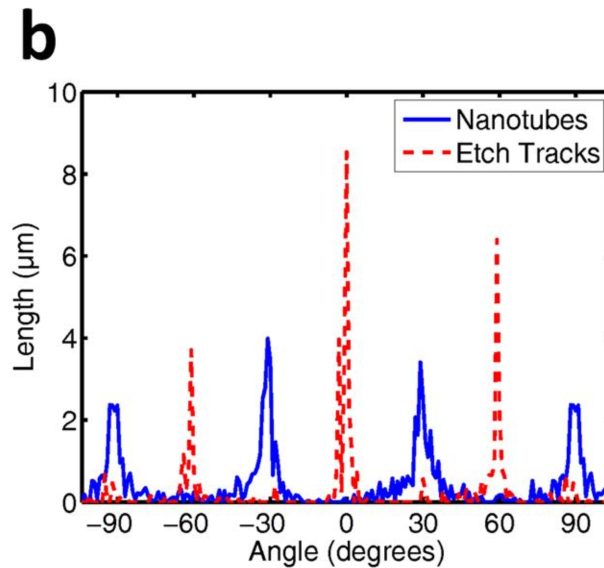

Figure 3.2. (a) AFM phase image of NTs and etch tracks in graphene. In the image, NTs have a higher contrast on the graphene while the etch tracks are the fainter lines. (b) Histograms generated from the AFM phase image of the total length of all NTs and etch tracks along a given angle, with an angular bin size of 1°. Etch tracks tend to occur every 60°, as represented by the peaks in the histograms, while NT histogram peaks are offset by 30°. Data beyond ± 90° are repeated in order to clearly view the peak located at 90°.

3.5 Thickness Dependence of Nanotube Alignment

The crystallographically-aligned growth of NTs on FLG becomes less pronounced as the flake thickness increases. For FLG thicker than about five atomic layers, the crystallographic alignment of CVD-grown NTs is substantially decreased. This thickness-dependent growth is illustrated by the single flake of FLG shown in Fig. 3.3a. This flake contains three regions that have thicknesses of 4.7 nm (i), 1.8 nm (ii), and 0.4 nm (iii). Detailed images of the FLG flake and the boundaries of the three regions (i-iii) are shown in the SEM images of Figs. 3.3b – 3.3d. The corresponding histograms of length versus angle are plotted in Fig. 3.3a. The size of the regions in Figs. 3.3b – 3.3d is chosen to include roughly the same amount of total NT length, in order to permit a valid statistical comparison between the three regions. Care was also taken not to select regions where NT growth may have been affected by FLG edges. The histograms in Fig. 3.3a show that under the same growth conditions, the NT alignment along the crystallographic axes of the FLG becomes much more pronounced for flakes less than ~6 atomic layers thick. A detailed AFM height analysis of more than 40 NTs in each of the three regions shows only a very slight change in average NT diameter for the various FLG thicknesses (from 6.2 ± 0.7 nm for the thinnest layer to 7.9 ± 1.6 nm for the thickest layer).

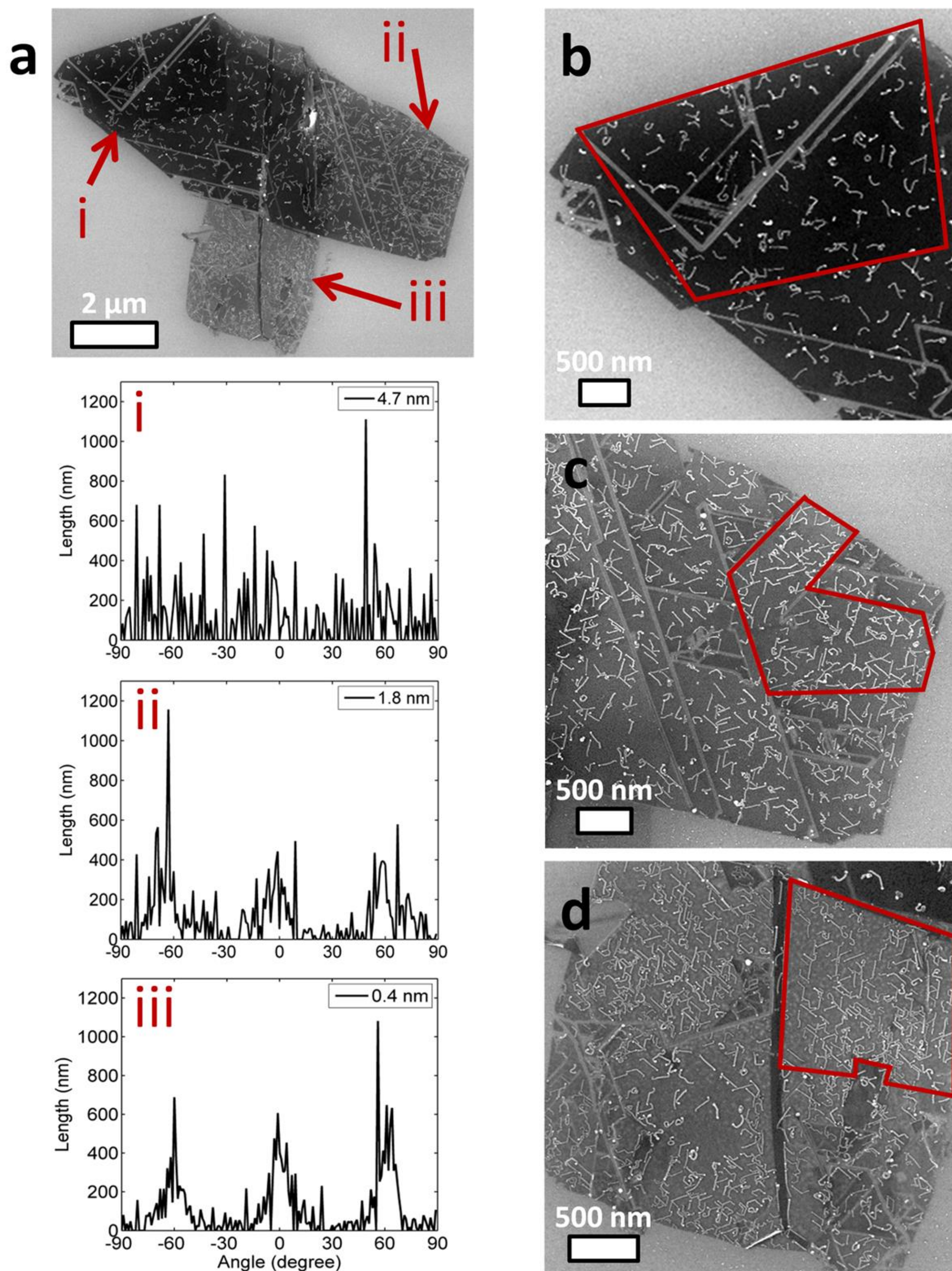

Figure 3.3. (a) SEM image of NTs grown on regions of a contiguous flake of FLG with thicknesses 4.7 nm (i), 1.8 nm (ii), and 0.4 nm (iii). The corresponding histograms generated from the three regions show that crystallographic alignment increases as FLG thickness decreases. (b-d) Higher resolution SEM images showing details of the three locations with the regions used for the histogram analysis outlined in red.

3.6 Unique Nanotube Morphologies

In addition to their pronounced crystallographic alignment on thin FLG films, we also find that NTs grown on FLG show abrupt changes in their direction of alignment to the underlying graphene lattice, usually from one armchair direction to another. This change in orientation produces kinks of 60° and 120° in otherwise straight NTs, as seen in Figs. 3.4a and 3.4b. Some of these abrupt changes seem to occur independently without interactions between NTs (as pointed to by the red solid arrows in Figs. 3.4a and 3.4b), while others result when one NT comes into contact with another (pointed to by the yellow dashed arrow in Fig. 3.4a). The abrupt changes in direction without NT intersections may be due to interactions between the growing NT-catalyst structure and defects or impurities in the FLG or SiO_2 substrate.

The interaction between growing NTs on FLG can also result in intricate patterns. Examples of such patterns are shown in Figs. 3.4c and 3.4d, where a growing NT has been bounded by two other NTs to form a crystallographic back-and-forth pattern. This suggests that the NTs grow through a surface-bound, tip-growth mechanism since it would be highly improbable for a fixed catalyst particle to produce such a structure precisely fitting between two other NTs. The formation of such back-and-forth patterns also indicates that the catalyst particles on FLG must remain very close to the surface (within a few nanometers) since NTs less than 10 nm in diameter act as effective barriers to the growth of other NTs.

Such a surface-bound tip-growth mechanism has previously been observed on faceted and atomic steps where nanoparticles slide along the surface leaving a NT behind in its wake.[68,101] Although the intricate patterns we observe support this NT growth process, future *in situ* electron microscopy experiments would be useful to definitively determine the mechanism.

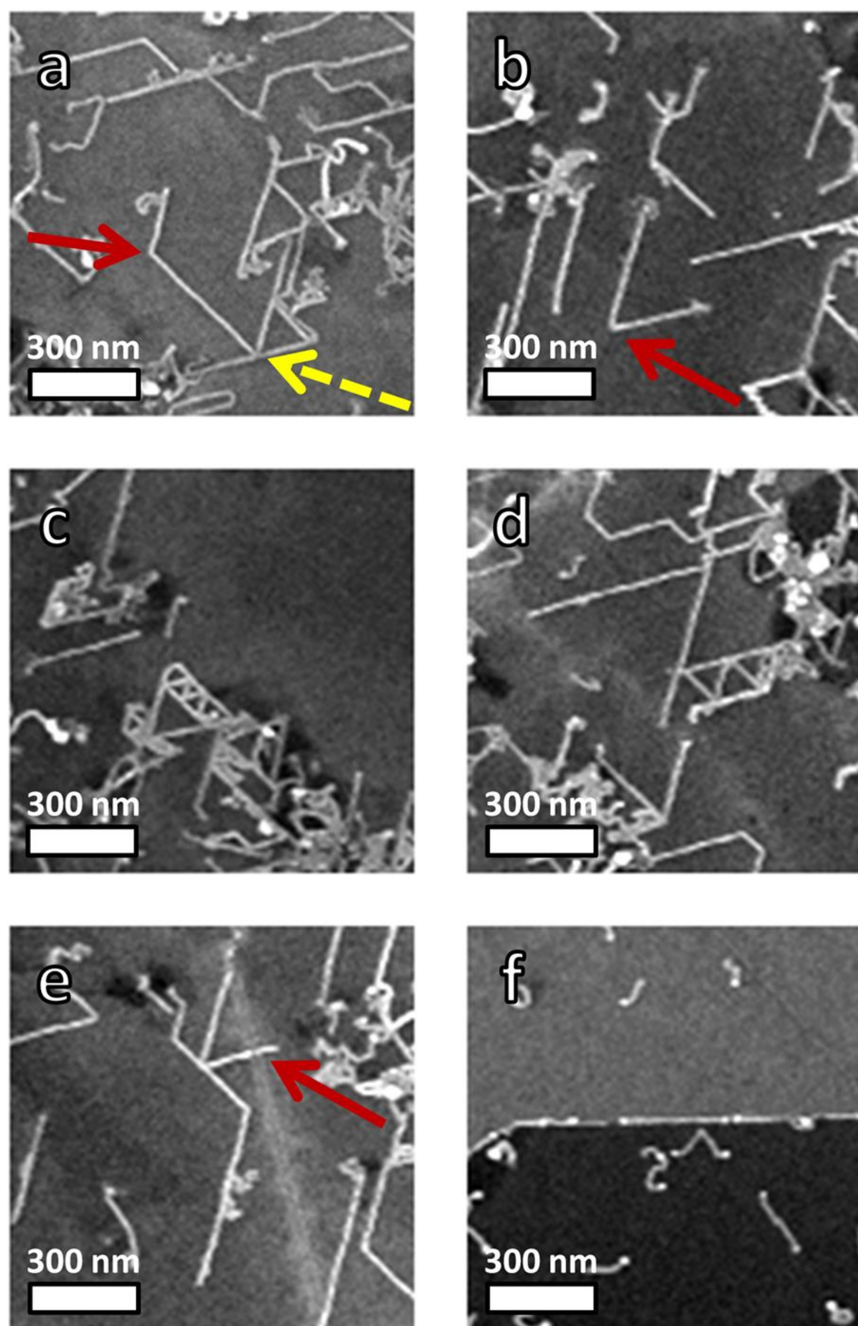

Figure 3.4. SEM images of NTs showing abrupt changes in crystallographic alignment. (a-b) NTs showing abrupt changes in direction on a FLG film ~ 0.4 nm thick, as determined by AFM. Red solid arrows point to NTs that abruptly change direction to an alternate crystal axis without interaction with other NTs, while yellow dashed arrow points to a NT that deflects away from another NT. (c-d) A growing NT caught between two parallel NTs can be deflected back and forth to create a zigzag-patterned NT, appearing like a sequence of equilateral triangles. (e) Crystallographically-aligned NT that is etched through by a catalyst particle. The location of the etch track through the NT is pointed to by the solid red arrow. (f) NTs grown along a step edge between two FLG regions of ~ 0.5 nm and ~ 2.5 nm thicknesses.

We also observe that NTs do not tend to cross etch tracks. Figure 3.4e shows a rare occurrence of a NT and etch track intersection, but with the NT having a cut in it. This suggests that the NT was formed first and a nanoparticle cut through it while forming an etch track at a later time. In addition, when a NT reaches a step edge between regions of differing FLG thickness, the nanotube will grow along the edge, as seen in Fig. 3.4f at the intersection between a ~ 0.5 nm and a ~ 2.5 nm region.

The typical bending radius we observe at the kinks of the NTs is less than the ~10 nm lateral resolution of the SEM and AFM images. This upper bound to the bending radius is extremely small compared to the ~ micron scale bending radii typically observed for NTs when the growth and alignment is understood to involve the lifting up of the catalyst particle from the surface of the substrate.[73,74,76-78] Such a small radius of curvature could indicate that the NTs change crystal direction abruptly rather than bend, which may have potential use in forming NT junctions.[102] Kinked NT growth has been reported along step edges on miscut quartz[69] and along various preferred crystallographic directions on Y-cut and Z-cut quartz substrates due to angular dependent van der Waals interactions.[71,76] NT growth on Z-cut quartz shows similarity to the growth geometries we observe on FLG substrates, with NTs having abrupt changes in direction between the three preferred growth axes which are separated by 60° intervals.

The crystallographic alignment of the NTs along the armchair directions of the FLG could indicate the prevalence of zigzag-oriented NTs. The interaction energy between a carbon nanotube and a graphitic substrate is dependent on the relative orientation of their lattice structures,[85,86,90] with the difference in interaction energy for aligned and misaligned nanotubes being on the order of 10 meV per nanometer of tube length.[92] This interaction energy could play a role during the catalytic formation since the catalyst particle remains within several nanometers to the surface of the FLG sheet. Moreover, since the catalyst particle remains close to the FLG surface during NT growth, the interactions between the catalyst particle and the FLG could also be important in the growth of crystallographically aligned NTs. Recent work has found significant electrostatic screening variations within FLG of various thicknesses,[56] and its interactions with metallic nanoparticles.[103] Such electrostatic interactions may play a role in the variation of crystallographic alignment for various thicknesses of FLG, as found here in Fig. 3.3.

Recent work on single-crystal sapphire has demonstrated that the chirality and diameter of NTs can be influenced by the crystallographic surface of the substrate.[72] Although this supports the possibility that zigzag-oriented NTs may be prevalent on our samples, another recent report on single-crystal quartz has found that chirality and diameter are instead not dependent on the crystalline substrate, even when the NTs are well aligned along specific crystal axes.[71] Thus, future experiments having either atomic resolution or sensitivity to chirality will be required to determine whether the crystal structure of the NTs themselves are influenced by the FLG support.

3.7 Potential for Transferring Nanotubes to Insulating Substrates

To utilize the NTs in electronics could require their isolation on insulating substrates away from the FLG support on which they are grown. To demonstrate that these NTs could be transferred to insulating substrates we have utilized an AFM tip to drag them off of the FLG flakes and onto the nearby SiO_2 substrate. Figure 3.5 shows the before (a) and after (b) AFM height images of NTs which have been dragged from an ~ 1.1 nm thick FLG onto the exposed SiO_2 with the AFM strokes represented by the arrows. This physical transfer of the NTs shows that they are not covalently bound to the FLG surface.

Figure 3.5c shows another region on the same FLG sample where ~ 10 adjacent strokes of an AFM tip (as indicated by the arrows) have dragged NTs completely off of the FLG and onto the nearby SiO_2 to two separate locations. Figure 3.5d shows micro-Raman spectra taken at the three circled regions marked in Fig. 3.5c. The Raman measurements taken over the NTs and FLG (region 1) show three distinct peaks in Fig. 3.5d that correspond to the well-known D, G, and G′ bands characteristic of sp^2 bonded carbon allotropes.[104] Raman measurements over the clump of NTs that were dragged from the FLG and displaced over the SiO_2 substrate (region 3) show a similar sp^2 bonded carbon response, whereas a control experiment over the SiO_2 (region 2) shows no appreciable Raman response. These results are an indication that the NTs we observe are in fact comprised of sp^2 bonded carbon. Moreover, in Fig. 3.5e, a detailed comparison of the G peaks of regions 1 and 3 shows that the shape is significantly more complex for the isolated NTs over the SiO_2.

When the NTs are isolated away from the FLG, which contributes a large single-Lorentzian background peak (upper curve), the multi-Lorentzian peak typical of carbon NTs is revealed (lower curve).[104]

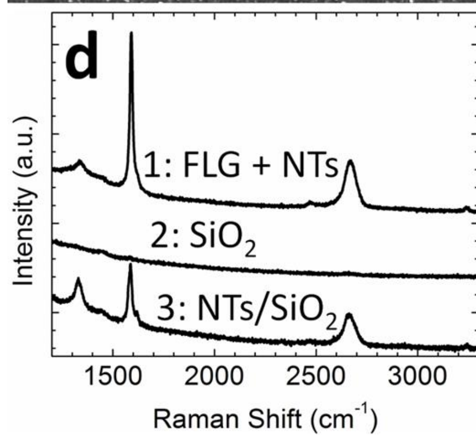
d
1: FLG + NTs
2: SiO$_2$
3: NTs/SiO$_2$
Intensity (a.u.)
1500
2000
2500
3000
Raman Shift (cm^{-1})

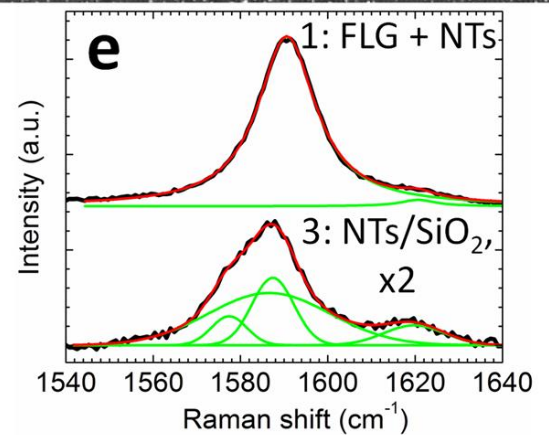
e
1: FLG + NTs
3: NTs/SiO$_2$,
x2
Intensity (a.u.)
1540
1560
1580
1600
1620
1640
Raman shift (cm^{-1})

Figure 3.5. (a) AFM height image of NTs on ~ 1.1 nm thick FLG before application of the AFM strokes represented by the arrows. (b) AFM image of same region after application of the AFM strokes showing NTs displaced off of the FLG substrate. (c) AFM image of two regions of the same sample where ~ 10 AFM strokes have moved a large number of NTs have been moved through nanomanipulation with an AFM tip in the directions indicated by the arrows. Inset shows an AFM image of the sample before the NTs were moved. (d) Micro-Raman spectra of the three regions circled in (c). (e) Expanded view of G band peaks comparing detailed signal from region containing NTs on FLG (region 1) to the region containing the deposited NTs on SiO_2 (region 3). The signal from the isolated NTs in region 3 is multiplied by a factor of 2. Red curves are fits comprising the sum of the Lorentzian line shapes plotted in green.

3.8 Conclusions

In summary, we report the CVD growth, without a feedstock gas, of NTs that are aligned to the crystal lattice of an underlying FLG support. Due to the presence of simultaneously produced etch tracks in the FLG, we can establish the relative crystallographic orientation of the NTs and we find that the majority of the alignment is along the armchair axes of the FLG, suggesting the prevalence of zigzag NTs. This crystallographic alignment appears much more pronounced in FLG films thinner than 6 atomic layers, indicating that electrostatic interactions with the catalyst particles may have a role in the NT growth mechanism. We have also observed NTs with sharp kinks having angles of 60° and 120°. These kinks can occur independently without the NTs interacting with each other. The sharp kinks are also formed at locations where NTs intersect and interact with each other resulting in crystallographic patterns, indicative of a tip-growth mechanism where catalyst particles remain within several nanometers of the FLG surface. These crystallographically oriented geometries could prove useful as kinked NT junction structures for future nanoelectronic applications.[102] To achieve such electronic applications, it would be useful to move the resulting NTs to an insulating substrate. We have demonstrated that NT transfer to an insulating substrate is possible by successfully dragging them with an AFM tip.

This dragging technique has been used to isolate a group of NTs away from the FLG support in order perform Raman spectroscopy, which confirms that the NTs are made of sp^2 bonded carbon. Other more elaborate methods for nanoscale transfer that are currently being developed[105] might be capable of precisely placing the NTs on insulating substrates without disturbing their as-grown geometrical arrangements.

Copyright © David Patrick Hunley 2015

CHAPTER 4: Integrated Nanotubes, Etch Tracks, and Nanoribbons in Crystallographic Alignment to a Graphene Lattice

4.1 Introduction

One of the ultimate goals driving the fields of nanoscience and nanotechnology has been the attainment of atomically-precise construction of intricate integrated systems consisting of materials with diverse behavior. Specifically, it is desirable to have high-performance conductors, semiconductors, and insulators integrated into complex atomically-precise arrangements.[106] The importance of atomic precision in nanoscale synthesis is further supported by the fact that there has been work indicating that the precise crystal orientation and interface quality becomes increasingly important as the individual nanomaterial components are reduced in size.[107-113]

Over the last few decades, a number of materials have attracted attention for future use in electronics as these nanomaterial components. One such component is the carbon nanotube (CNT), a form of sp^2 carbon that has a band-gap determined by its diameter and wrapping vector which leads to a wide variation of its possible transport properties -- including both semiconducting and conducting behaviors.[12] CNTs have received considerable attention due, in part, to their high electrical mobility and thermal conductivity among other fascinating properties. Another potential nano-electronic building block is graphene, which is a two-dimensional form of the same sp^2 honeycomb structure contained in CNTs.[66] While graphene has many of the same potential advantages as CNTs, such as high carrier mobility, unless it is confined to segments ~10 nm in size or less it does not contain an appreciable band-gap[29] in comparison to small-radius semiconducting CNTs.[12] As such, graphene and few-layer graphene (FLG) may find a more obvious application in future electronics as nanoscale atomically-thin conducting interconnects and leads.[44,47,65,114,115] Due to its strength[116] and resistance to electrical breakdown,[52,117] graphene is also attractive as a nanoscale conductor for its potential in sustaining large electrical current densities. A third material that may find use in future nano-electronics is the insulator SiO_2. Due to the ubiquitous use of SiO_2 in modern

electronics,[118] this material, or perhaps an alternative high-κ material,[119] could likely find an integral use in future nano-electronic architectures.

The ability to integrate graphene, CNTs, and a dielectric like SiO_2 into ordered nanoscale systems would represent a promising step towards achieving the integration of diverse nanomaterial components into intricate architectures. Towards this goal, it has recently been discovered that FLG situated on insulating SiO_2 surfaces can be catalytically-etched along specific crystal directions with tracks having widths of order 10 nm or less.[49] This is significant because it demonstrates the successful integration of nanoscale graphene and insulating regions having specific crystal orientations with respect to the graphene lattice. Moreover, when two etch tracks are closely spaced, their tendency to align along specific crystal directions can result in the formation of nanoribbons with crystallographic orientation relative to the rest of the graphene lattice.[49,51] In other work, CNTs have recently been shown to grow along specific crystal orientations on the surface of a FLG substrate.[58,59] While these ~5-6 nm diameter CNTs are slightly too large to have an appreciable band-gap useful for many applications, this result is a step towards achieving the successful integration of a semiconducting nano-material and a conductor with crystallographic orientation. These above-mentioned results have demonstrated integration between two of the three desired components -- CNTs, FLG, and a dielectric -- though the successful nanoscale integration with crystallographic orientational order of all three has yet to be achieved.

4.2. Experimental Details

The fabrication of these integrated, atomic-scale systems is achieved through the implementation of multiple processing steps.[120] First, p^+-doped silicon substrates having a 300 nm thermal oxide layer are cleaned through ultrasonication in acetone, isopropyl alcohol, and deionized water for 3 minutes each using a Branson 2510 Bransonic Ultrasonic Cleaner. The substrates are then subjected to UV ozone (UVO) cleaning in a NovaScan PSD Series Digital UV Ozone System for 15 minutes. Next, kish graphite is exfoliated onto the substrates, followed by the electron beam evaporation of a nominally 0.02 nm layer of nickel. Samples are then placed in a Thermo Scientific Lindberg Model

TF55035C CVD furnace with MKS Type 247D Mass-Flo Controllers where they are annealed at 500° C for 30 min to facilitate the formation of nickel catalyst nanoparticles. Immediately following this step, samples are heated to 1000° C for 60 min. Throughout the entire CVD furnace processing, gas flows of 850 and 150 sccm of Ar and H_2, respectively, are maintained. The furnace temperature is increased using a controlled ramp rate of 50° C per min. After the high-temperature processing step, the samples are allowed to passively cool to room temperature within the furnace.

Atomic force microscopy (AFM) imaging of the samples was performed with an Asylum Research MFP-3D AFM in tapping mode using Tap300Al-G probes from NanoAndMore USA and have nominal tip radii <10 nm. The AFM was used in the experiments for imaging and determining an estimate of the FLG thicknesses. Scanning electron microscopy (SEM) imaging was performed with a Zeiss Supra 35 field-emission SEM with a Gemini column.

4.3 Bridging Nanogaps with Nanotubes

Here we demonstrate the successful integration of FLG, CNTs, and etch tracks exposing SiO_2 into nanoscale systems with precise crystallographic orientations. Specifically, CNTs are grown across nanogap etch tracks and nanoribbons formed within few-layer graphene films as a result of chemical vapor deposition (CVD) processing. Due to the fact that these three nanoscale components align along specific directions of a single few-layer graphene lattice, their relative orientations are locked into precise values. This provides a potential route to achieve precise orientation of conductors, insulators, and semiconductors with nanoscale intricacy. Furthermore, the fact that the integrated alignment of CNTs and graphene occurs with minimal apparent influence from the underlying SiO_2 substrate suggests that it could also be achievable on other high-performance insulators, such as high-κ dielectric materials that might play an important role as nanoscale building blocks in future electronics. Our results also suggest that the integrated formation can be achieved by growing CNTs directly over nanogap etch tracks and nanoribbons while maintaining crystallographic orientation with the underlying FLG. We have computed estimates of the vibrational energy of CNTs that indicate that multi-

walled CNTs (MWNTs) and single-walled CNTs (SWNTs) should be capable of maintaining atomic registry with an underlying graphene lattice as they grow across a typical etch track, in agreement with our experimental results. These calculations also suggest that the observed integrated crystallographic alignment could be achievable for much smaller diameter semiconducting CNTs having larger band-gaps, as long as small catalyst particles can be stabilized on FLG.

Figure 4.1a shows an atomic force microscope height image of a 1.3 nm layer thick FLG sample. The sample has had both catalytic etching and CNT growth performed on it through the CVD processing. The straight dark lines are the catalytic etch tracks down to the underlying SiO_2 substrate. For comparison to the etched regions, an exposed portion of the underlying substrate is observable at the lower-left of this AFM image. The white lines are CNTs that have grown on top of the FLG. While an applied feedstock gas can be used to control the growth of CNTs on the surface of FLG,[59] the samples discussed here were prepared without one, as has been previously reported.[51,58,59] For this case, when an applied feedstock is not applied, the specific source of carbon has not yet been determined; though the likely ones are the nearby catalytic etching (both inside and outside the view of the image in figure 4.1a) and possible residual surface contamination due to processing. Regardless of the specific source of carbon, the CNTs do not appear to be produced by catalyst particles that have been involved in the formation of etch tracks, and *vice versa*.

As has been reported previously,[58] both the etch tracks and CNTs preferentially form along specific crystal axes of the graphene -- the etch tracks along the three zigzag directions and the CNTs along the three armchair directions of graphene. A histogram of overall length versus angle of the CNTs and the etch tracks in figure 4.1a is plotted in figure 4.1b, which clearly shows their preferred crystallographic orientations to the FLG lattice.

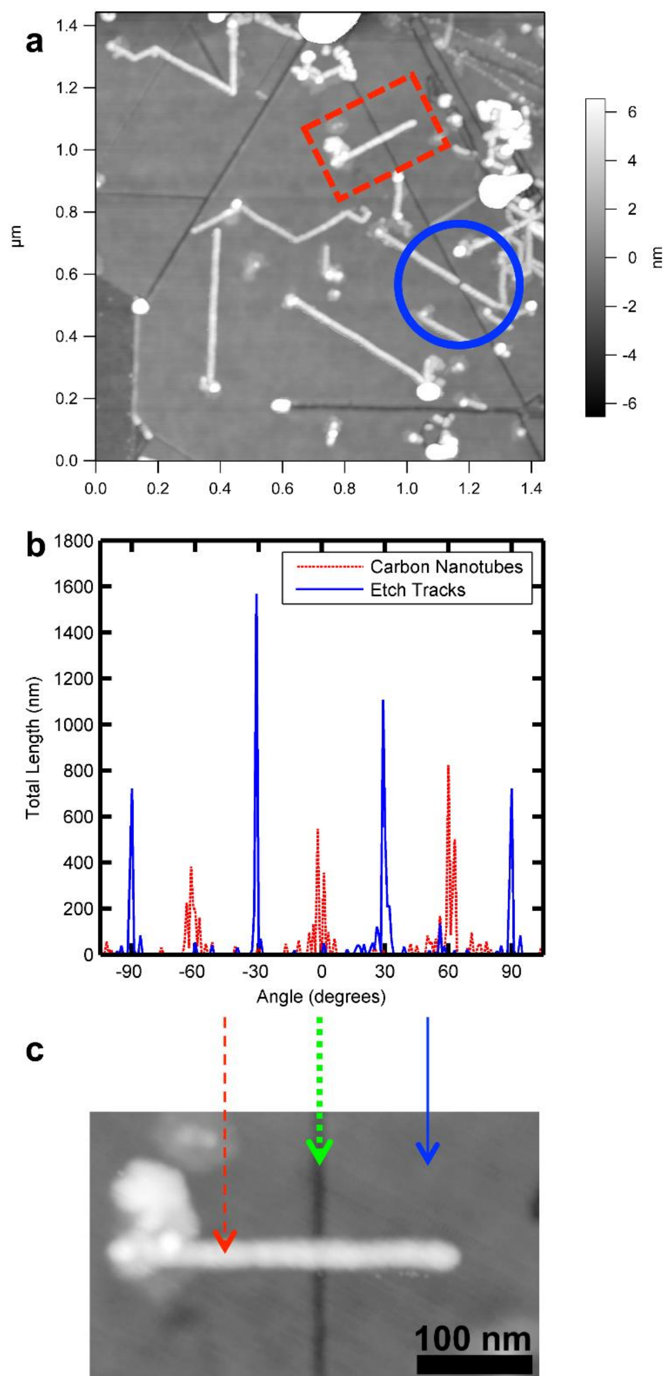

Figure 4.1. AFM image of a CNT traversing a graphene nanogap etch track. (a) A 1.3 nm FLG sample with etched tracks (dark grey) and CNTs (white lines). The CNT circled by the blue line has been sliced by the catalyst particle that etched the adjacent track. The CNT inside the red dashed rectangle traverses an adjacent etch track without having been sliced. (b) A histogram of length versus angle for the CNTs and etch tracks in (a). (c) Magnified view of the dashed square region in (a). The arrows in (c) point to the FLG (solid blue), a CNT (dashed red), and the exposed SiO_2 evident through the etch track (dotted green).

Due to these preferred crystal orientations, there are only a limited number of angles in which the etch tracks and CNTs will typically intersect. Previously, it had been observed that CNTs can be cut at these intersections.[58] That is, a catalyst particle may simultaneously act to cut the FLG into two regions with an etch track and to slice a CNT on the surface into two pieces. Evidence for this dual etching process is observed in the blue circled region in figure 4.1a, where the CNT appears to have been cut into two separate pieces directly at the location of the underlying etch track. While such a system comprises a CNT and some FLG in close proximity to insulating SiO_2, it does not represent an integration of these three components into an arrangement that is likely to be of use for future nano-electronics.[106] In this same image we observe a distinctly different integration within the dashed red rectangle of these three components with significantly greater potential for future nano-electronics. In this second region, the CNT completely traverses the etch track without being cut by a catalyst particle, as is clearly apparent by the enlarged AFM image of that region in figure 4.1c. The arrows in figure 4.1c point to the 1.3 nm layer FLG (solid blue), the CNT (dashed red), and the exposed SiO_2 (dotted green).

The preferred crystallographic orientations of the CNTs and etch tracks result in a limited number of preferred angles in which their integration is obtained. The preferred orientation is clearly evident in the thicker 3.8 nm thick FLG sample shown in figure 4.2 that has two nearby CNTs that traverse the same etch track. In the scanning electron microscope (SEM) image of this sample, the FLG is the dark region (pointed to by the solid blue arrow), the CNTs are the lightest lines (pointed to by the dashed red arrows), and the etch tracks exposing the underlying SiO_2 substrate are the grey lines (pointed to by the dotted green arrow). The striking result is that two nearby CNTs traverse the etch track in the exact same direction. The fact that the CNT is being locked into specific crystal directions of the underlying FLG lattice is evident by the abrupt changes in direction occurring in multiples of 60 degrees. While thicker FLG samples tend to show less crystallographic alignment of the CNTs when grown using nearly identical conditions,[58] this 3.8 nm thick sample still contains several localized regions demonstrating this crystallographic alignment of CNTs. We determine that the traversed etch track in figure 4.2 is along the armchair direction due to the fact that it is 30 degrees offset from the dominant one (which is along the zigzag axis[50]) within the FLG flake. Thus, we conclude

that the CNTs are aligned to a common armchair axis of the FLG which is, however, along a different direction to the etch track.

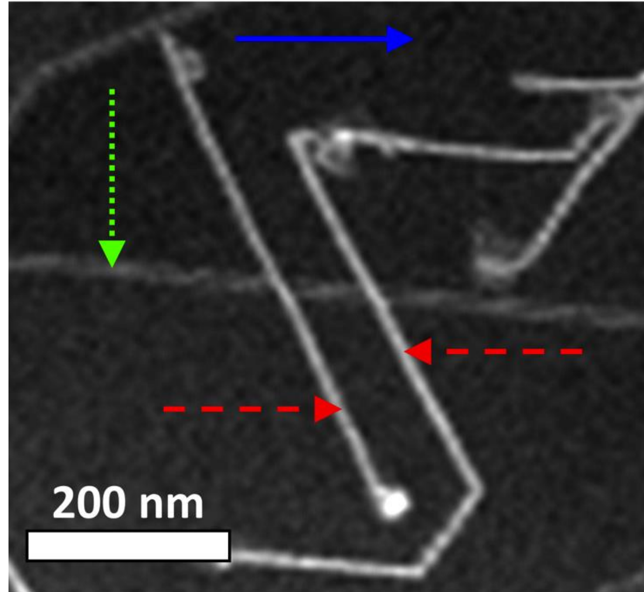

Figure 4.2. SEM image of two parallel CNTs traversing an armchair-directed etched FLG nanogap. The 3.8 nm thick FLG is the dark region (solid blue arrow), the CNTs are the lightest lines (dashed red arrows), and the etch tracks exposing the underlying SiO_2 substrate are the grey lines (dotted green arrow).

Nanoribbons can also be integrated into crystallographically-oriented structures consisting of CNTs, graphene, and insulating SiO_2 tracks. Figure 4.3 shows an SEM image of another region of the same sample in figure 4.2 consisting of a crystallographically-oriented FLG nanoribbon (pointed to by the solid blue arrow) that has been formed through two closely spaced etch tracks (pointed to by the dotted green arrows) which expose the underlying SiO_2 substrate. A CNT (pointed to by the dashed red arrow) clearly extends between two separate FLG regions traversing both etch tracks and the imbedded nanoribbon. Since the etch tracks are along the zigzag axis, we conclude that the CNT is along an armchair direction since it makes an approximately 90 degree angle with the nanoribbon.

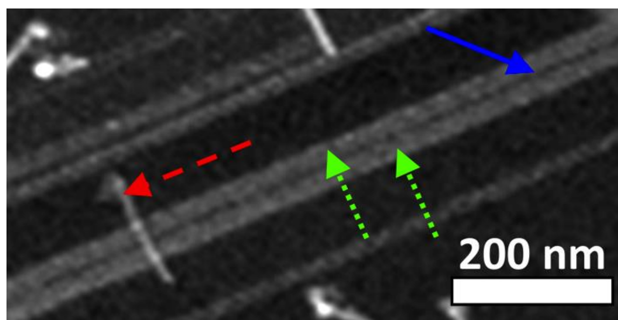

Figure 4.3. SEM image of a nanotube traversing two closely spaced etch tracks that bound a FLG nanoribbon. The dark line is the FLG nanoribbon (solid blue arrow) that has been formed through the two closely spaced etch tracks (dotted green arrows) that expose the underlying SiO_2 substrate. The lightest line is the CNT (dashed red arrow) while the other dark regions are 3.8 nm thick FLG.

4.4 Potential Growth Mechanisms

There are several possible mechanisms by which CNTs and etched graphene can be integrated together to form the intricate nanoscale structures we observe in figure 4.1, 4.2, and 4.3. Possible mechanisms include routes where (1) the CNT growth occurs first followed by etching of the underlying FLG (*i.e.*, growth followed by etching (GFE)), or (2) the etching of the FLG occurs first followed by CNT growth over the etch tracks (*i.e.*, etching followed by growth (EFG)). Since both etching and CNT growth both occur during the same CVD processing steps in our experiments, we are not able to decisively determine which of these mechanisms is involved in the construction of the integrated CNT-FLG nanoscale systems we observe. That being said, the fact that the sample in figure 4.1a consists of one CNT (within the blue circle) that has been cut by a catalyst particle performing etching while another (within the red square) has not, suggests different mechanisms are involved in these two regions. Moreover, the EFG mechanism has the advantage in the formation of integrated nanoscale structures because in this sequence the CNT cannot be damaged or etched into two pieces as the catalyst particle moves past it. To realize this advantage of the EFG mechanism, the CNT must be capable of remaining rigidly aligned to the lattice of the underlying FLG as it crosses the etched void in order to remain in crystallographic orientation on both sides of the gap.

In order to determine whether the EFG mechanism could be involved in constructing integrated CNT-FLG structures like the ones we observe, we use Euler-Bernoulli beam theory[121] on the model illustrated in figure 4.4a. In this model we assume that a CNT is growing across a nanogap from left to right between two pieces of FLG. As the CNT grows in length across the gap it requires less energy for its tip to make a displacement δ. If the thermal energy fluctuations are sufficient to cause a large enough displacement δ, we argue that the CNT will not remain crystallographic on the right side of the gap as it grows. This energy scale delineates a critical boundary between crystallographic and non-crystallographic growth of the CNT as it is integrated with an etch track in the FLG. While the required displacement δ required to disturb crystallographic growth is likely dependent on the detailed interactions between a growing CNT and the underlying FLG, which are as yet still not well understood, we can set it to a typical graphene lattice constant (*i.e.*, $\delta = 0.246$ nm) in order to estimate this critical parameter boundary.

In this calculation of the critical parameter boundary, we make two other simplifications. The first is that the CNT remains rigidly fixed to the FLG surface on the left side and only bends in the gap region. The second assumption is that the entire mass of the Ni catalyst particle (with a diameter set equal to the CNT diameter) is concentrated at a single point on the end of the CNT. With these simplifications, the CNT is described by the time-dependent Euler-Bernoulli relation $\frac{\partial^4 y}{\partial x^4} = -\mu \frac{\partial^2 y}{\partial t^2}$, where μ is the mass per unit length of the CNT, I is the moment of inertia, and E is the elastic modulus. With one clamped end and a point mass on the other, the CNT is subjected to the four boundary conditions $y(0) = 0$, $y'(0) = 0$, $y''(W) = 0$, and $y'''(W) = -\frac{m{\omega_n}^2}{EI} y(W)$, where m is the mass of the catalyst particle and ω_n is the frequency of the nth free oscillatory mode of the CNT. This leads to a transcendental relation,

$$1 + cosh(\zeta_n)cos(\zeta_n) + \frac{2m}{\mu W^4}{\zeta_n}^4\{sinh(\zeta_n)cos(\zeta_n) - cosh(\zeta_n)sin(\zeta_n)\} = 0,$$

where $\zeta_n = \left(\frac{\mu{\omega_n}^2}{EI}\right)^{1/4} W$ and the zeros determine the natural oscillating frequencies ω_n of the CNT with a catalyst particle attached. Solving the time-dependent Euler-Bernoulli relation subjected to the boundary conditions yields for the first mode the solution, $y_1(x) =$

$A\left\{cosh\left(\frac{\zeta_1 x}{W}\right) - cos\left(\frac{\zeta_1 x}{W}\right) + \frac{(cosh(\zeta_1)+cos(\zeta_1))\left(sin\left(\frac{\zeta_1 x}{W}\right)-sinh\left(\frac{\zeta_1 x}{W}\right)\right)}{sinh(\zeta_1)+sin(\zeta_1)}\right\}$, where A is a free constant we use to require that the critical CNT tip displacement $\delta = y_1(W)$, assuming higher-energy modes do not contribute. Once the functional form $y_1(x)$ of the CNT displacement is fully determined, we compute its elastic energy at its extremum, $U = \int_0^W \frac{EI}{2}\left(\frac{\partial^2 y_1}{\partial x^2}\right)^2 dx$, which we estimate as the total energy stored in the vibrating CNT.

We compute this estimate of the energy of vibration for various widths, W, of the nanogap and radii of the CNTs for both MWCNTs and SWCNTs. To achieve the MWCNT calculation, we determine the moment of inertia assuming a solid rod, a mass density given by $\mu = \pi r^2 \rho$ where ρ is the average mass per unit volume for graphite, and an elastic modulus given by $E = 1.28$ TPa.[122] For the SWCNT calculation, the rod must be modeled as an atomically-thin-walled graphene tube. Theoretical work has previously shown that the flexural rigidity (D) and the in-plane stiffness ($C = hE$) of a single graphene sheet can be consistently described through the use of an effective thickness of $h = 0.066$ nm and an elastic modulus of $E = 5.5$ TPa.[123,124] For the following SWCNT calculation we will use this effective thickness and elastic modulus relevant for a single shell graphene tube. Since the bending of a thin-walled tube depends to lowest order only on C, the results we obtain are approximately the same as using the parameters consistent with bulk graphite, *i.e.*, $E = 1.28$ TPa and $h = 0.34$ nm. In addition, for the SWCNT case the mass density is given by $\mu = 2\pi r\sigma$ where σ is the average mass per unit area for graphene.

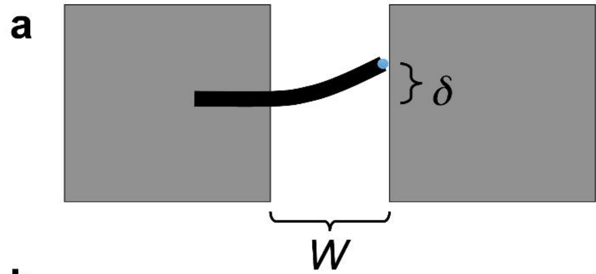
a
δ
W

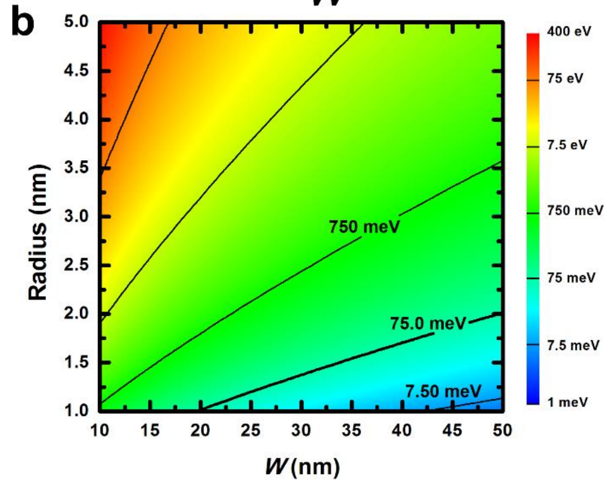
b
Radius (nm)
W (nm)
750 meV
75.0 meV
7.50 meV
400 eV
75 eV
7.5 eV
750 meV
75 meV
7.5 meV
1 meV

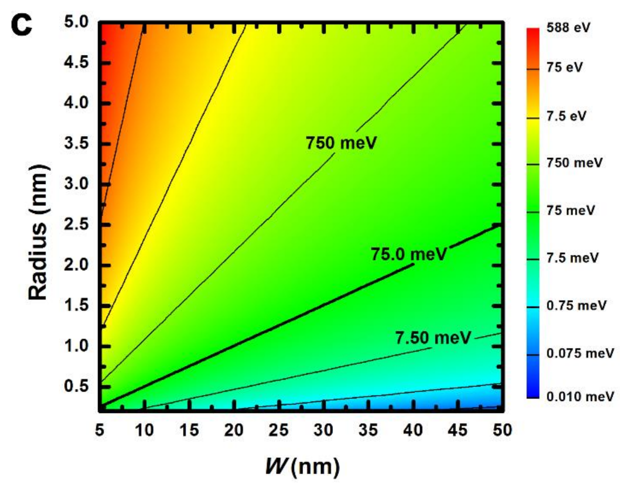
c
Radius (nm)
W (nm)
750 meV
75.0 meV
7.50 meV
588 eV
75 eV
7.5 eV
750 meV
75 meV
7.5 meV
0.75 meV
0.075 meV
0.010 meV

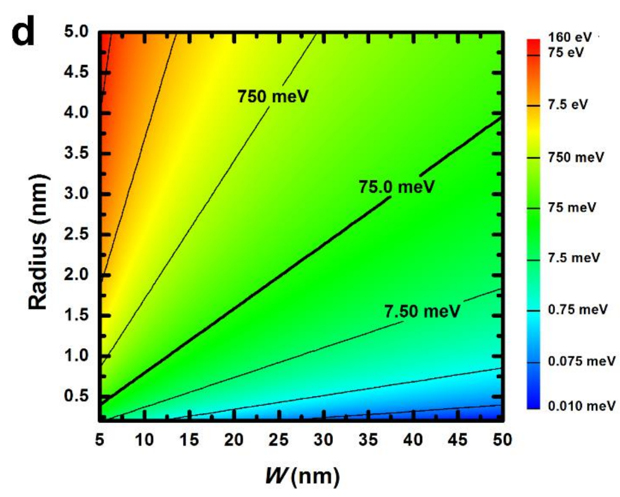
d
Radius (nm)
W (nm)
750 meV
75.0 meV
7.50 meV
160 eV
75 eV
7.5 eV
750 meV
75 meV
7.5 meV
0.75 meV
0.075 meV
0.010 meV

Figure 4.4. (a) Model of a CNT traversing a FLG nanogap. The width of the FLG nanogap is W and the deflection of the CNT tip with catalyst particle is δ. (b) The calculated energy based on the model in (a) for the lowest energy mode of oscillation for a MWCNT to vibrate its tip by $\delta = 0.246$ nm as a function of CNT radius and nanogap width. (c) The calculated energy for the lowest energy mode of oscillation for a SWCNT to vibrate its tip by $\delta = 0.246$ nm as a function of CNT radius and nanogap width using the parameters $h = 0.066$ nm and $E = 5.5$ TPa. (d) Calculation of the energy for a SWCNT to vibrate its tip by $\delta = 0.246$ nm using a conservative choice of parameters with $h = 0.066$ nm and $E = 1.28$ TPa. Bold solid lines in (b), (c), and (d) are equal to the value of 75.0 meV.

Figure 4.4b and 4.4c show the calculated energies of the lowest energy mode for the MWCNT (figure 4.4b) and the SWCNT (figure 4.4c) cases. In both figures, a bold line is drawn at 75.0 meV, which is the approximate temperature scale of the furnace during processing. The upper-left region of the grey-scale plot is the regime of larger diameter CNTs and shorter etched FLG nanogaps. The diameters ($\gtrsim$ 5-6 nm) of the CNTs we experimentally observe integrated with FLG nanogaps of various widths in Figs. 4.1-4.3 are well within this high-energy regime -- supporting the view that the integrated structures we observe could have been formed through the EFG mechanism. According to figure 4.4b, as the nanogap is increased in size and the CNT radius is decreased, the energy required to significantly deflect the end of the CNT is reduced. However, this significant deflection is only relevant for nanogaps much larger than the ones etched in our samples or for CNTs with a much smaller radius. The calculations for the SWCNT case are qualitatively similar to the MWCNT case, but with a lower energy required for deflection. That said, the energy for deflection is calculated to be significantly greater than the processing temperature for SWCNTs with radii similar to the ones we observe across relatively large ($W \lesssim$ 30 nm) nanogaps.

To truly integrate semiconducting SWCNTs across FLG nanogaps, it is desirable to utilize the smallest radius CNTs that have the largest band-gaps. Although our calculations show a decreasing energy for deflection with radius, for the narrowest etched FLG nanogaps experimentally observed where W approaches 5 nm, CNTs with radii below 0.5 nm should still exceed the thermal energy scale. Thus, our calculations suggest that the smallest radii CNTs could be crystallographically integrated with extremely short

($\lesssim$5 nm width) FLG nanogaps. Even the results of a conservative estimate of the thermal energy, such as the one shown in figure 4.4d that uses an effective thin wall of $h = 0.066$ nm and the lower elastic modulus of bulk graphite of $E = 1.28$ TPa, gives a value greater than 75.0 meV for CNTs with radii below $0.5\ nm$ growing across ~$5\ nm$ nanogaps. The success of this conservative estimate demonstrates that the precise choice of physical parameters in our model does not alter our conclusions.

4.5 Conclusion

While we have previously obtained FLG nanogaps approaching the required width, the CNTs we have so far grown are typically between 5-6 nm in diameter on the thinnest FLG. This limitation on the width of the CNT diameter is likely due to the fact that the catalyst particles used to grow them are formed in thermal equilibrium with the underlying FLG, prior to CNT growth. Currently, it is thought that the cohesive energy within the nanoparticle competes with the electrostatic interactions with the FLG to drive such the system to form an equilibrium size that is typically greater than ~5 nm.[103] This could explain why the method we have used produces CNTs with radii typically in this 5-6 nm regime.[58] To overcome this CNT size limitation in the future, one might be able to utilize catalyst particles which are not allowed to come into equilibrium with the underlying FLG prior to CNT growth -- thus permitting the diameters of the catalyst particles (and thus the CNTs) to be smaller. Finally, to achieve the ultimate limits in device-scaling utilizing the CNT-FLG systems discussed here, it would be desirable to achieve this integration with single-layer graphene. While clean crystallographic catalytic etching has been reported on single-layer graphene,[51] such tracks are usually not as straight as those on FLG, which leaves another future avenue for improving this integrated system beyond the work presented here.

In summary, we have synthesized integrated systems of CNTs and FLG nanogap etch tracks and nanoribbons consisting of preferred crystallographic orientations of the graphene lattice. The fact that the crystallographic orientations are not strongly influenced by an underlying SiO_2 substrate suggests that this intricate integration could potentially be extended to other dielectrics. Our calculations support a mechanism for integration

whereby a CNT grows directly across an etched FLG nanogap with crystallographic orientation maintained in the process. A comparison to the thermal energy scale suggests this process could also be achievable for the smallest diameter semiconducting CNTs. Thus, this work could represent a step towards achieving intricately-ordered integrated nanoscale systems consisting of conducting, semiconducting, and insulating components.

Copyright © David Patrick Hunley 2015

CHAPTER 5: Friction, Adhesion, and Elasticity of Graphene Edges

5.1 Introduction

Graphene has tremendous potential for use in a wide range of applications owing to its incredible mechanical, thermal, and electronic properties.[57,66,125,126] The structural properties of graphene edges are expected to play an important role in electrical and thermal transport,[25,127] particularly as the dimensions of graphene elements are reduced to the nanoscale.[32,33,49,128] In addition, strain within graphene can induce an effective local magnetic field[129-133] making recently proposed strain effects in the vicinity of graphene edges particularly important in determining transport properties of graphene nanostructures,[129,134-137] while recent theoretical work has also raised the possibility that strain along the graphene edge could inhibit quantum Hall effect physics.[135,138] Although recent investigations of the mechanical properties of bulk graphene have demonstrated its tremendous strength[116] and low friction,[139-142] such characteristics have been relatively unexplored in the vicinity of its edges.

Lateral force microscopy (LFM), which is the measurement of torsional deflections of a cantilever as it is dragged over a surface, has been used over the last few decades to probe nanometer-scale frictional and topographic features.[143] Although it has long been known that there are significant increases in lateral force signals at atomic scale steps,[144,145] the source of these increases has been of ongoing debate.[141,146-148] Elimination of these localized increases, while maintaining the overall atomic-scale surface topography, could have significant implications towards the realization of low-friction micro- and nano-electromechanical systems.

Here we report on frictional, adhesive, and elastic characteristics of graphene edges through the use of lateral force microscopy.[149] LFM reveals a significant local frictional increase at the exposed edges of graphene, whereas a single overlapping layer of graphene nearly completely removes this local frictional increase. This result indicates graphene could be an ideal, atomically thin coating for reducing local friction associated with atomic steps. Direct comparison between LFM and atomic force microscopy (AFM) measurements shows that the local forces on the scanning probe are successfully modeled

with a vertical adhesion in the vicinity of the atomic-scale graphene steps. Taking this adhesion into account allows for the surface topography of graphene to be determined through low-load LFM measurements and also provides a new low-load LFM calibration method. Through the use of carefully maintained scanning probe tips, we also observe evidence of elastic straining of graphene edges, which behave as nanoscale springs. Estimates of the strain energy are consistent with out-of-plane bending of graphene edges when sharp LFM tips are dragged into them. The elastic response we observe represents the reversible straining of graphene edges and could represent a possible route for reversibly tuning the electronic properties of graphene.

5.2 Experimental Details

The graphene samples were prepared through mechanical exfoliation of kish graphite onto silicon substrates with a 300 nm oxide layer.[57] Prior to exfoliation, the substrates were placed in an ultrasonic cleaner in acetone, isopropyl alcohol, and deionized water for 3 minutes each. This was followed by UV-ozone cleaning. After exfoliation, few-layer graphene films were initially identified through optical microscopy. The number of atomic layers was then determined through both Raman spectroscopy and AFM height measurements. The graphene films did not undergo any further processing.

The LFM measurements were performed with an Asylum Research MFP-3D atomic force microscope in ambient laboratory conditions (at a temperature of 20 ± 3 C° and a relative humidity of 20 ± 3 %). We used PPP-LFMR probes, manufactured by Nanosensors, which have nominal values of 0.2 N/m and 23 kHz for the force constant and resonant frequency, respectively. As usual in LFM, the scan angle is selected such that the cantilever beam is perpendicular to the fast scanning direction. Light from an infrared laser is reflected off the back of the cantilever and onto a four-quadrant position sensitive detector (PSD) in order to monitor both lateral and vertical deflections of the probe. When the tip is scanned across the sample surface, lateral forces cause the cantilever to undergo torsional rotation. This deflects the laser spot in the horizontal direction at the PSD. Simultaneously, the vertical deflection is maintained through closed-loop feedback control which provides topographical information of the scanned region. In these experiments, we

utilized probes which minimized crosstalk between the horizontal and vertical laser spot deflections.[150]

Measurement of the adhesion force is done by bringing the tip into contact with the sample surface then retracting it while monitoring the deflection voltage to determine the force required to snap the tip off the sample surface. Details of these adhesion measurements and their relation to scanning probe tip properties are discussed in Appendix A. Overall, we find that differences in the tip-graphene and tip-SiO_2 adhesion forces are negligible. The net load F_{net} is defined as the sum of the vertical applied load L by the scanning probe cantilever and the adhesion force A between the tip and sample. Applying a negative load L is possible by first bringing the tip into contact with the sample surface then allowing the adhesion force to maintain contact when the negative load is applied.

5.3 AFM and LFM of Graphene Edges

To investigate the mechanical and frictional characteristics of graphene edges we focus on graphene crosses where one graphene layer obliquely overlaps a second layer. Such crosses occasionally occur during the mechanical exfoliation processes and provide two different edges for comparison -- one exposed and the other covered by a layer of graphene. Figure 5.1a shows an atomic force microscopy (AFM) contact-mode height scan of a cross formed from two single layers of graphene that produced four distinct regions – two that are one atomic layer thick, a bilayer region, and the exposed SiO_2.

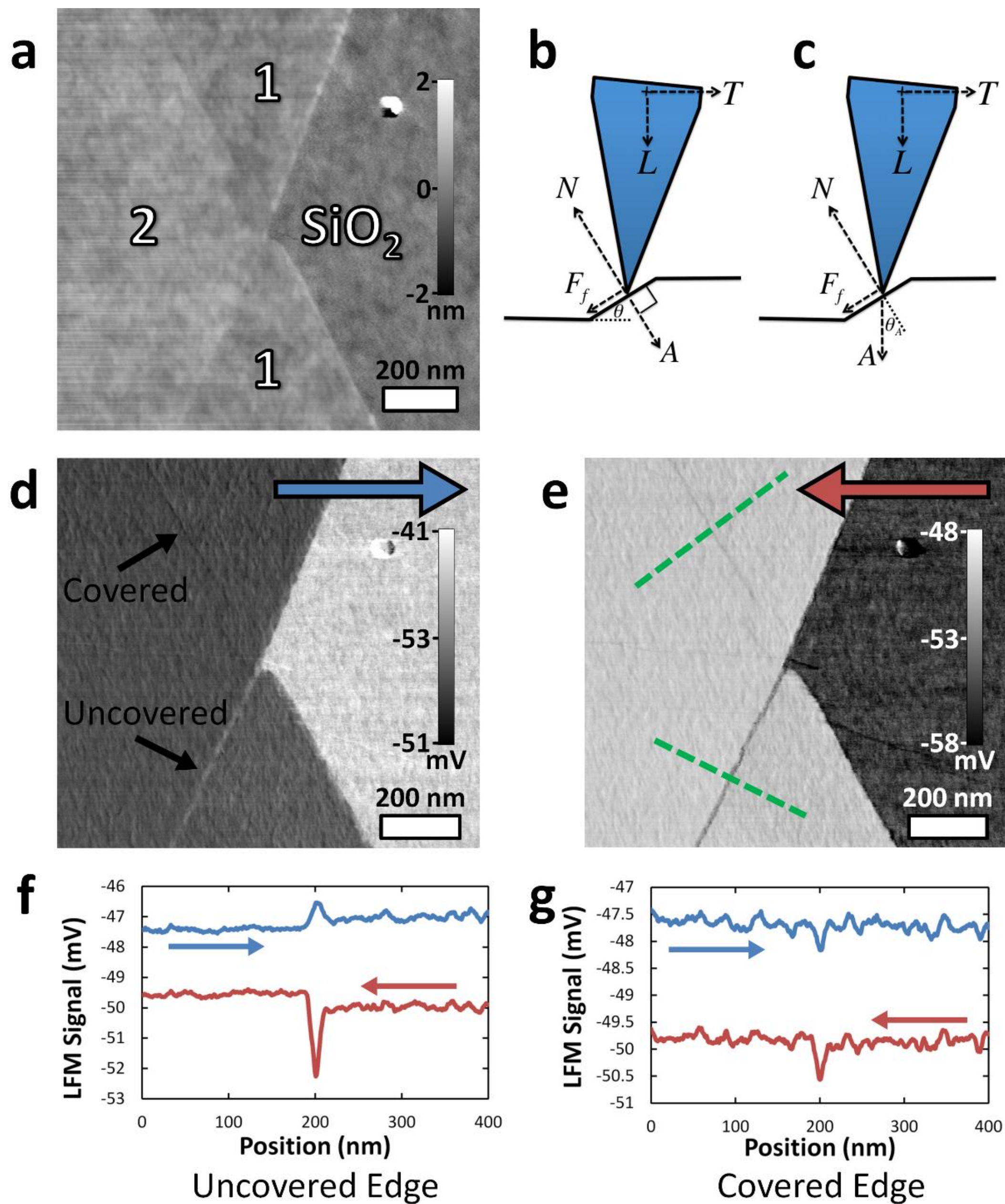

Figure 5.1. AFM and LFM of graphene crosses. **a,** Contact mode AFM height image of a graphene cross. **b-c,** Schematic diagram of LFM model with the adhesion directed normal (**b**) to the local surface and vertically (**c**) as the tip is dragged over a step. **d-e,** LFM scan image formed while scanning the tip in the "trace" direction (left to right) (**d**) and in the "retrace" direction (right to left) (**e**). **f-g,** Line scans taken from (**e**) along the green dashed lines for the uncovered (**f**) and covered (**g**) edges. Data represent the average of 150 adjacent line scans over a width of 146 nm. The data in **d-g** were taken with a net load F_{net} of 9.0 nN, where F_{net} is defined as the sum of the 6.7 nN load L applied by the cantilever tip and the 2.3 nN adhesion A of the tip to the surface determined through independent force plots.

Although the AFM height image of Fig. 5.1a does not show discernible differences between the boundaries, LFM (Figs. 5.1b and 5.1c) clearly distinguishes between the two types of edges. Figures 5.1d and 5.1e show the lateral signals simultaneously measured with the contact-mode data in Fig. 5.1a. Figure 5.1d corresponds to the "trace" image (scanning left to right) and Fig. 5.1e corresponds to the "retrace" image (scanning right to left). In both the trace and retrace LFM images, the uncovered edge has much greater contrast than the covered edge. Moreover, the uncovered edge shows both a positive and negative torsional deflection of the lateral probe depending on scan direction whereas the covered edge produces the same LFM deflection regardless of scan direction, clearly discernible in the line scans in Figs. 5.1f and 5.1g. These LFM measurements allow for the easy identification of covered or uncovered step edges, enabling one to determine the stacking arrangements and folds of few-layer graphene systems.

5.4 Quantifying LFM Forces

To quantify these results, we model the forces on an LFM tip as shown in Figs. 5.1b and 5.1c over a surface having a local incline angle θ (with details of this model discussed in Appendix B). The forces on the tip are balanced by the forces and moments applied to the cantilever and will sum to zero assuming the tip is not accelerating. The forces applied to the cantilever are the transverse force T and the load force L while the resulting moment causes the torsional rotation of the cantilever. We model the tip sample interaction as a normal reaction force N and a frictional force obeying Amonton's law $F_f = \mu N$. In descriptions of interactions between macroscopic inclines and scanning probe tips,[151,152] the adhesion A is typically modeled as an attractive force directed normal to the incline, as in Fig. 5.1b. However, this choice is not necessarily valid for very short inclines that occur for atomic scale changes in topography, so we allow A to have a variable direction ranging from the local surface normal (Fig. 5.1b) to the vertical direction where $\theta = \theta_A$ (Fig. 5.1c). In the small angle approximation discussed in detail in Appendix B, the above model gives the local coefficient of friction,

$$\mu = \frac{\alpha W_V}{(L+A)}, \qquad \text{Eq. 5.1}$$

which depends on the difference between trace and retrace LFM voltage measurements ($2W_V = (V_t - V_r)$) and an LFM calibration coefficient α that converts the measured voltage to the lateral force on the cantilever tip. The model also gives the local incline assuming normal directed adhesion,

$$\theta = \frac{\alpha \Delta_{V_0}}{L + (L + A)\mu^2}, \qquad \text{Eq. 5.2}$$

while for vertical adhesion,

$$\theta = \frac{\alpha \Delta_{V_0}}{(L + A)(1 + \mu^2)}. \qquad \text{Eq. 5.3}$$

These equations depend on the average of the trace and retrace voltage measurements ($\Delta_{V_0} = (V_t + V_r)/2 - V_0$) with a zero offset ($V_0$) estimated by averaging $(V_t + V_r)/2$ over a flat region.

Figures 5.2a and 5.2b show, respectively, LFM scans of an uncovered graphene edge and an edge covered by a single layer of graphene which (along with the LFM trace measurements not shown) is used to determine a spatially varying W_V and Δ_{V_0} and, thus, the local frictional variations and surface topography through Eqs. (1-3). Fig 5.2c is the coefficient of friction as a function of position for the uncovered edge for net loads ranging from 1.1 – 8.1 nN, showing that there is a substantial increase in the friction near the step edge for these loads. This contrasts the behavior at the covered edge, Fig. 5.2d, where we find that there is essentially no signature of a local increase in friction (estimated as a reduction of more than 90%). This result indicates graphene could be an ideal, atomically thin coating for reducing local friction associated with atomic steps.

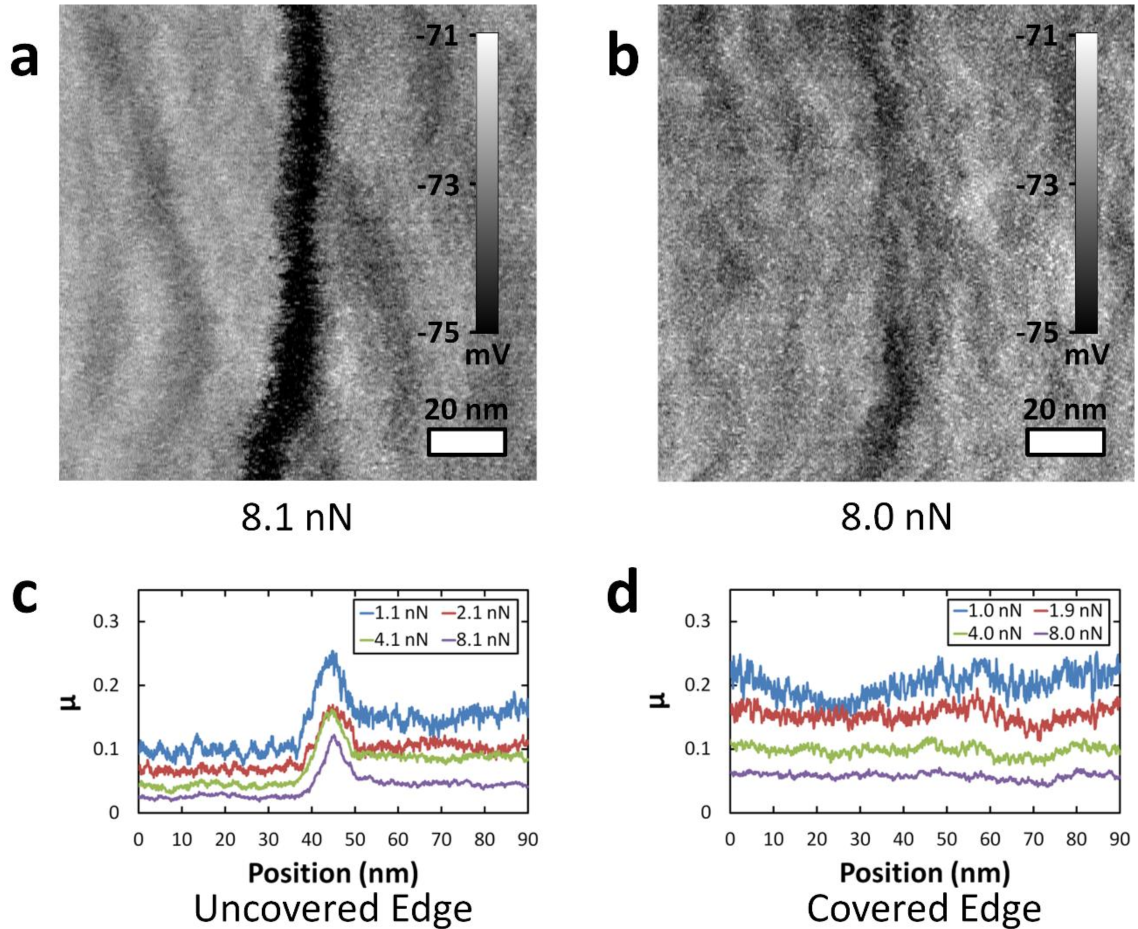

Figure 5.2. Local frictional characteristics of graphene edges. **a-b,** LFM retrace scans of an uncovered (**a**) and covered (**b**) graphene edge. For both scan regions the bi-layer graphene is on the left and the single layer is on the right. F_{net} for the scan in **a** is 8.1 nN with a 2.8 nN adhesion while the scan in **b** is 8.0 nN with a 2.6 nN adhesion. **c-d,** Analysis of line scan data from **a** and **b** at various loads using Eq. 5.1 in text. Data represent the average of 50 adjacent line scans over a width of 20 nm. The graphene edges correspond to a location in the middle of these plots (between 40 and 50 nm along the x-axis). The friction of the bi-layer region varies between **b** and **c** due to the change in scan angle (kept normal to the edge under investigation), which is consistent with recent reports of anisotropic frictional behavior of graphene surfaces.[140]

5.5 Novel Low-Load LFM Calibration Technique

The determination of the local topography from the LFM response is shown in Fig. 5.3 using both adhesion models (Eqs. (2) and (3)). Assuming a normally directed adhesion (Figs. 5.3a and 5.3b) erroneously suggests a topography over the graphene edge that is strongly dependent on L. In contrast, the vertically directed adhesion model results in a

topography which is remarkably consistent over the same range of applied loads (Figs. 5.3c and 5.3d). This is a strong indication that the adhesion forces remain predominantly in the vertical direction as the tip traverses the atomic step edges. These topographic determinations also show excellent agreement with the simultaneously determined AFM height measurements for covered edges, uncovered edges, and regions of graphene that conform to the undulations of the substrate, as demonstrated by the agreement to the spatial derivative of the height measurements (black line) in Figs. 5.3c and 5.3d. Since the term $1 + \mu^2 \approx 1$ for low friction graphene surfaces, the AFM height measurements can be directly compared to the LFM Δ_{V_0} values to obtain the α calibration coefficient. This represents a new low-load LFM calibration method (compared to other techniques[151,152]) that is sensitive to correct modeling of adhesion forces.

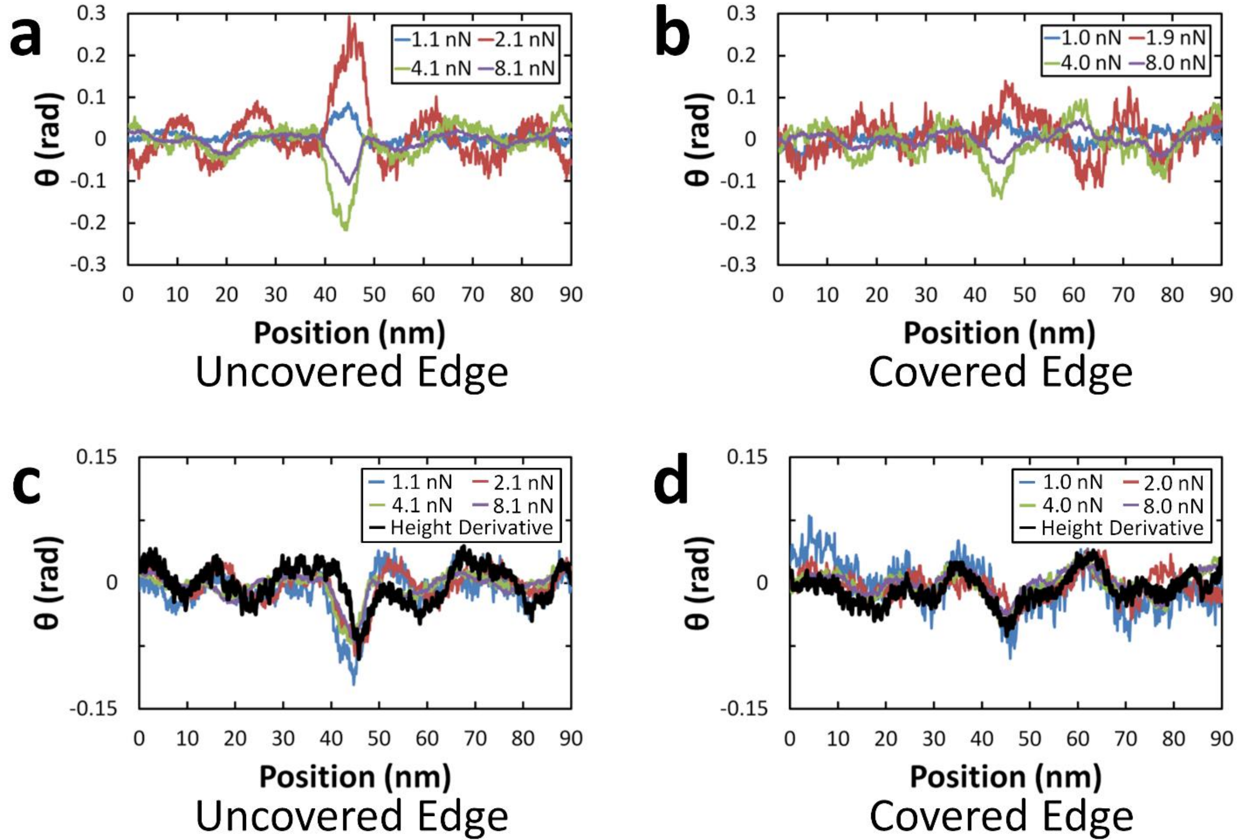

Figure 5.3. Topography of graphene edges determined through LFM. **a-b,** Analysis of line scan data from Fig. 5.2 at various loads using the normal adhesion model, Eq. 5.2 in text. **c-d,** Analysis of line scan data from Fig. 5.2 at various loads using the vertical adhesion model, Eq. 5.3 in text. The black line is the spatial derivative of the AFM height measurements. Data represent the average of 50 adjacent line scans over a width of 20 nm. The graphene edges correspond to a location in the middle of these plots (between 40 and 50 nm along the x-axis).

5.6 Flexing an Exposed Graphene Edge

The above measurements were all performed with tips that were previously scanned laterally over regions of SiO_2 substrate resulting in tips with adhesions of 2.0 - 3.0 nN, a value consistent with previous reports.[142,148] When we utilize tips that are scanned with low normal loads restricted only to the graphene regions, we observe lower adhesion forces of ~1.0 nN. These carefully maintained tips also show strongly altered LFM characteristics over exposed graphene edges. Figure 5.4a is a retrace scan of an exposed graphene edge, demonstrating an abrupt change in the lateral force as the tip moves up over the atomic

step (going from a mono-layer to a bi-layer region). A single line scan (Fig. 5.4b) reveals that as the tip is dragged into the graphene edge in the retrace direction, the LFM signal increases approximately linearly followed by an abrupt reduction in force at a location approximately 10 nm to the left. These LFM signals indicate that we are straining the exposed graphene edge as the tip moves up the step followed by a release of the stored elastic energy. These signals are repeatable over hundreds of trace/retrace cycles of the LFM tip (as in Fig. 5.4a) without noticeable displacement of the graphene edge, indicating that the edge is being elastically strained.

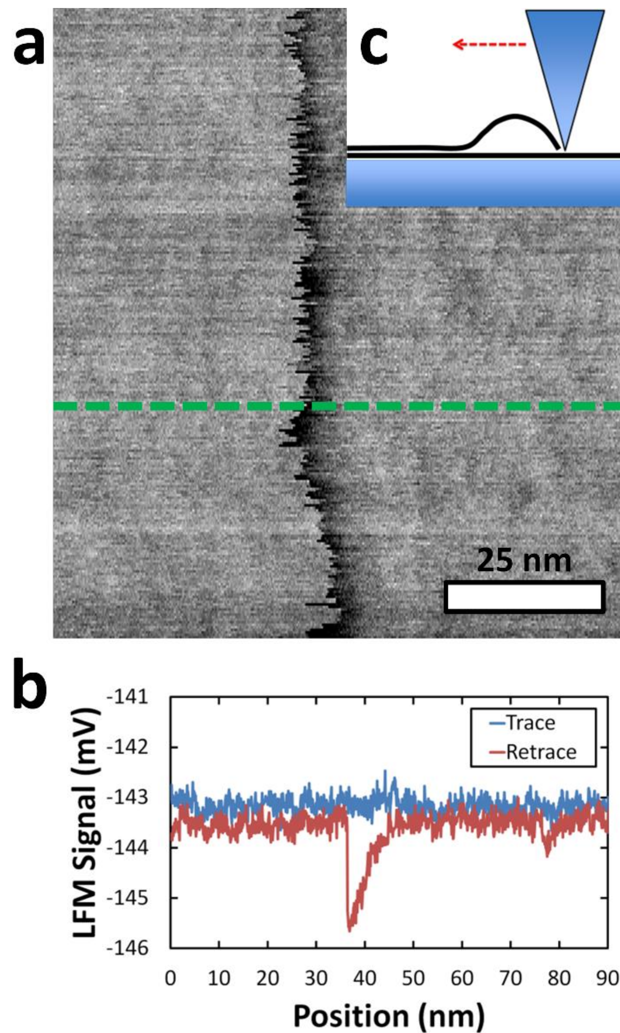

Figure 5.4. Elastic response of graphene edge. **a,** LFM retrace scan of a graphene edge. Bi-layer region is on the left, and single layer region is on the right. **b**, Single LFM scan lines in the trace and retrace directions as the tip is dragged across the edge. **c,** Schematic model of the tip causing out-of-plane strain of the edge as the tip is dragged towards it, to the right.

5.7 Spring Constant of Graphene Edges

The effective spring constant, k, for flexing the graphene edge is estimated from the linear LFM response to be ~ 0.29 ± 0.11 N/m. This spring constant value of the graphene edge is nearly two orders of magnitude smaller than the torsional spring constant of the LFM tip $k_{tip} = GJ/(l(h + t/2)^2) \approx 24$ N/m,[151] where $G = 64$ Pa is the shear modulus of silicon, J is the torsion constant (approximated as $0.3wt^3$, where w is the 48 μm width and t is the 1 μm thickness of the cantilever), l is the 225 μm length of the cantilever, and h is the 12.5 μm height of the cantilever. Since $k \ll k_{tip}$, the vast majority of the deflection occurs within the graphene when the tip is laterally pressed against the graphene edge.

5.8 Modeling the Observed Stick-Slip

The stick-slip response of the graphene edge when laterally scanning with well-maintained, sharp tips can be qualitatively understood through extension of a recently proposed effective potential under low normal loads in the vicinity of an atomic step, $U = E\{-erf(x/b_1) + erf([x - c]/b_2)\}$.[146] In this model E is a constant of order an eV, b_1 is the effective barrier width at the edge ($x \equiv 0$) which should be on the order of the tip apex radius, and b_2 and c are constants larger than b_1 which represent a slow recovery of the potential. Assuming that such a potential describes the graphene edge, even when it has been flexed, the value of x represents the relative position of the tip to the graphene edge. Stick-slip motion of this relative coordinate as the tip moves into the edge (in the $-\hat{x}$ direction) will occur at points where $\frac{d^2U}{dx^2} = -k$. Assuming reasonable values of $E = 2$ eV and $10b_1 = b_2 = c$ in the above potential with the observed spring constant of $k \approx 0.3$ N/m yields stick-slip behavior for $b_1 \lesssim 1$ nm. For atomic-scale effective barriers with $b_1 \approx 0.1$ nm the stick slip distance is ≈ 11 nm -- in good agreement with our experiments. As the effective tip apex and barrier width increase beyond 1 nm, the relative edge-tip distance is instead smoothly varying as the tip moves up the edge. This suggests that the smoothly varying lateral signal we observe for worn tips is due to their larger effective tip apex radii; a view also supported by their increased adhesion to the sample surface.

Covered edges do not show stick-slip flexing for the same well-maintained sharp tips and normal loads that cause this large ($\sim 10\ nm$) stick-slip flexing of uncovered edges. This suggests that a single covering layer of graphene increases the effective barrier width and/or decreases its depth to suppress stick-slip. The covering layer may also similarly act to suppress much smaller atomic-scale stick-slip displacements of the edge as a large-diameter worn tip (like the ones used to obtain the data in Figs. 5.1-5.3) moves over it. The reduction of atomic-scale stick-slip should likewise lead to the concomitant decrease in friction,[153] which could be the source of the significantly reduced friction observed for worn tips over covered edges in comparison to uncovered edges seen in Fig 5.2.

5.9 Graphene Flexing Modes

The energy stored in the large ($\sim 10\ nm$) uncovered graphene edge strain using well-maintained sharp tips is approximately $k(10\ nm)^2/2 \approx 90\ eV$. Estimates of possible in-plane strain energy are too large to account for this observed edge displacement. In-plane strain energy can be estimated with a two-dimensional model as $\frac{\pi L}{8}\frac{E}{1-\nu^2}x^2$ where E ($\approx$ 1.02 TPa) is Young's modulus, L ($\approx$ 0.34 nm) is the thickness of graphene, and ν ($\approx$ 0.24) is the Poisson ratio for graphene[154] -- giving an energy of $9000\ eV$ for $x \approx 10$ nm displacement.[153]

In contrast, out-of-plane distortions (as represented in Fig. 5.4c) are much more consistent with our measurements. Although a detailed determination of possible out-of-plane strain energy is a subtle issue,[154] we obtain a rough estimate of it by considering the sum of the energy stored in bending a ~ 10 nm region of graphene in addition to the van der Waals (vdW) adhesion energy over this same region. The bending energy can be estimated through $2C\int dxdy(d^2u/dx^2)^2$, where u is the deflection and C (1.2 eV) is the bending stiffness.[155] Assuming a uniform bending radius of ~ 9 nm yields an energy of ~5 eV. An estimate of the adhesion energy over a ~ 10 nm diameter region can be estimated from the vdW adhesion energy (1.6×10^{18} eV/m^2)[155] to be ~130 eV. Since the sum of these out-of-plane energies is the same order of magnitude as our measurements, our observed edge strain is consistent with such a mode of deformation. Considering the large

effects that such a strain can have on the transport properties of graphene,[130] the elastic response we observe represents a possible route for reversibly tuning the electronic properties of graphene.

It has also recently been suggested that out-of-plain elastic strain over the bulk portions of few-layer graphene samples could play an important role in the frictional dissipation for sharp asperities.[156] Likewise, the out-of-plane elastic strain indicated by our experiments could lead to additional modes of frictional energy dissipation at graphene edges.

5.10 Conclusions

We have observed frictional, adhesive, and elastic characteristics of graphene edges through the use of LFM. By focusing on single overlapping graphene layers (graphene crosses), LFM has revealed a significant local frictional increase at the exposed edges of graphene. In contrast, an edge covered by a single overlapping layer of graphene nearly completely removes this local frictional increase, indicating that graphene could be an ideal, atomically thin coating for reducing local friction associated with atomic steps. Experimental comparison of LFM and AFM revealed that the local adhesion in the vicinity of graphene edges is directed vertically downwards. Taking this vertical adhesion into account allows for the surface topography of graphene to be determined through low-load LFM measurements and also provides a new low-load LFM calibration method. Through the use of low-adhesion scanning probe tips, we also observed evidence of elastic straining of graphene edges that act like nanoscale springs. Estimates of the strain energy are consistent with out-of-plane bending of graphene edges when atomically sharp LFM tips are dragged into them which causes a single large (~ 10 nm) stick-slip event. The elastic response we observe represents the reversible straining of graphene edges and could have application in future nanoscale electro-mechanical devices.

Copyright © David Patrick Hunley 2015

CHAPTER 6: Analytical Model for Self-Heating in Nanowire Geometries

6.1 Introduction

There has recently been considerable interest in understanding and controlling the local temperature increases within electrically driven nanoscale wires and metallic interconnects. As electronic components are reduced in size with a simultaneous increase in complexity of their integrated circuitry, Joule heating is expected to be a limiting factor to device performance and lifetime. To this end, there have been a number of recent investigations of electrical fatigue and breakdown of nanowire devices constructed from a variety of materials for potential future nano-electronic components.[157,158] Controlled electrical breakdown is also currently being explored as a possible route to achieving molecular-scale electronic devices. Applying large currents to metallic wires can lead to nanoscale junctions and nanogaps on the molecular scale due to thermal degradation and electromigration of electrodes.[33,43,159-174] In addition to traditional metallic and semiconducting material components, graphene and organic-based devices are areas of intense current research, with organic devices in particular facing significant challenges with thermal stability.[175,176] Moreover, Joule heating has recently been utilized as an effective method to clean the surfaces of few-layer graphene devices[126,177] which have great potential for use in future nano-electronics.[84]

Thus, the development of novel nanowire devices could receive benefit from improved understanding and modeling of their Joule heating. To this end, there have recently been several analytic diffusive models proposed for describing the local temperature increases due to Joule heating of nanoscale interconnects.[178,179] Although some of these models take heat spreading below the nanowire into account, they generally ignore the heat spreading within the contact pads to the nanowire. Since the region of the contact-nanowire interface can have large temperature and material gradients they are, as a result, likely locations of device failure.[157,158] Thus, modeling the temperature in the vicinity of the contact-nanowire interface is particularly important for understanding device fatigue and failure, in addition to developing nanogap device formation.

Here we present an analytical diffusive model of Joule heating in a nanowire that incorporates the heat spreading both below the nanowire and within the contact region.[180] The heat spreading below the nanowire is achieved by matching the linear heat flow near the nanowire-insulator interface with a radially symmetric spreading solution through an interpolation function. A similar method is used to model the spreading in the contacts. We compare our analytical model with finite-element simulations and find excellent agreement over a wider range of system parameters compared to other recent models. A comparison to other models and the simulations indicates that our heat-spreading model is particularly useful for cases when the width of the nanowire is less than the thermal healing length of the contacts and when the thermal resistance of the contact is appreciable relative to the thermal resistance of the nanowire.

6.2 Model of Heat Generation in a Nanowire Field Effect Transistor

The system we model is schematically shown in Fig. 6.1a, where two large contact pads of width W_c and thickness τ_c are electrically connected to a nanowire of width W, thickness τ_n, and length L situated on an insulating substrate of thickness d located on top of a conducting back gate at ambient temperature. Within an infinitesimal slice of the nanowire dx along the length of the wire (as shown in Fig. 6.1b) the rate of heat generation within the slice (dQ_r/dt) is equal to the heat lost to the surrounding medium at steady state. This heat lost can be broken up into that conducted away through the substrate (dQ_s/dt) and through the nanowire itself (dQ_n/dt).

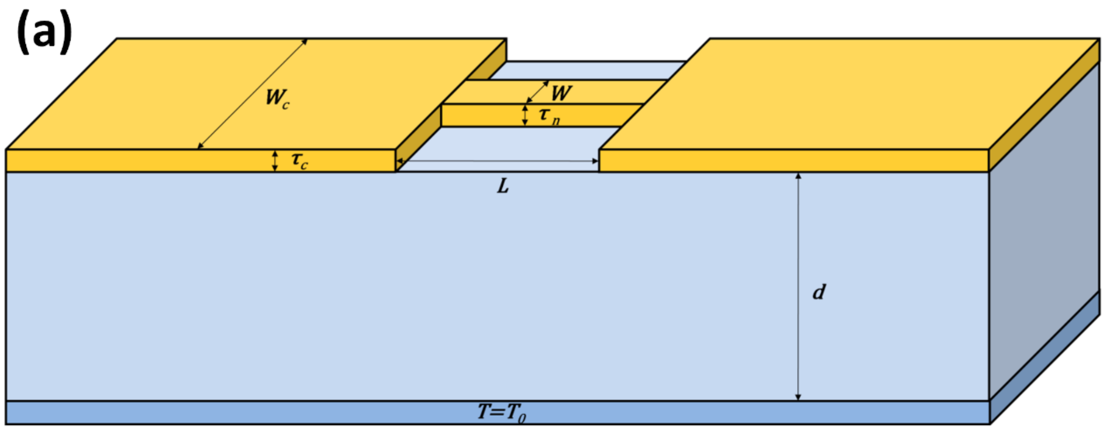
(a)
W_c
W
τ_n
τ_c
L
d
$T=T_0$

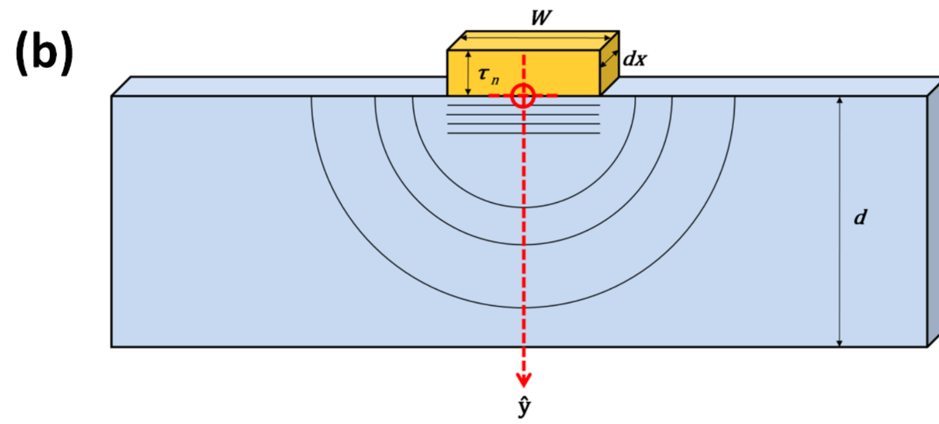
(b)
W
dx
τ_n
d
$\hat{y}$

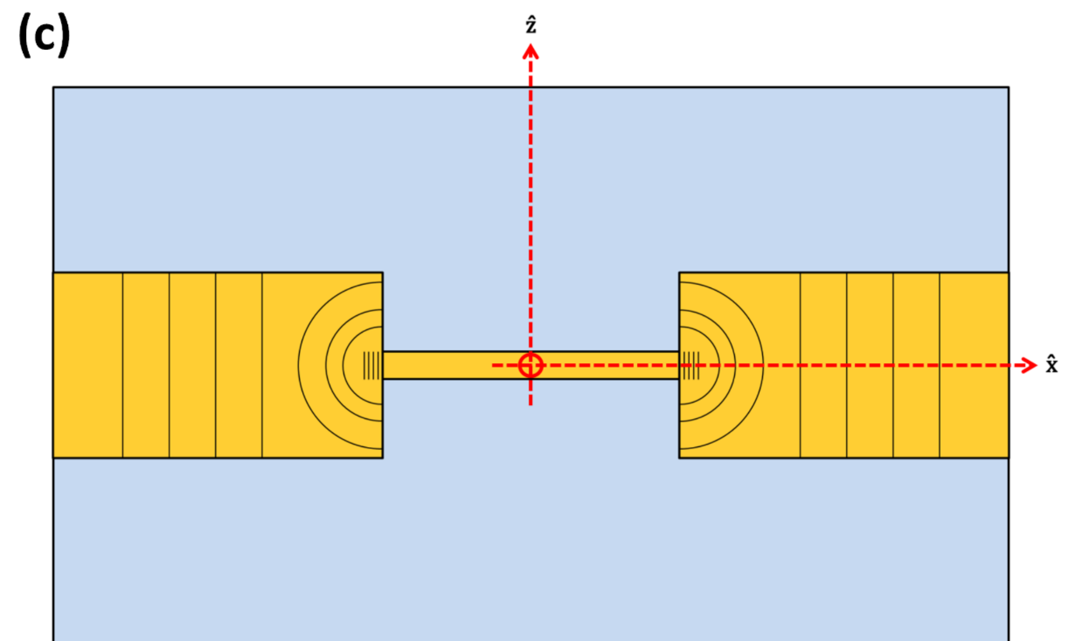
(c)
$\hat{z}$
$\hat{x}$

Figure 6.1. (a) Metallic nanowire geometry and electrodes shown in yellow, electrically insulating material of thickness d below the nanowire, and an electrically conducting back-plane at ambient temperature T_0 on the bottom. (b) Cross-sectional slice of the nanowire with direction of the $\hat{y}$-axis shown. The parallel lines directly below the nanowire represent the approximate behavior of the isotherms in the vicinity of the nanowire while the radial lines represent those farther below. (c) Top view of the nanowire and contacts showing the $\hat{x}$ and $\hat{z}$ axes. The straight lines near the nanowire-contact interface, the radial lines within the contacts, and the farther spaced parallel lines deep within the contact represent approximate expected isotherms.

Due to the typical geometries and temperatures involved in such devices, radiative heat losses are negligible. Thus, at steady state,

$$0 = \frac{dQ_r}{dt} - \frac{dQ_s}{dt} - \frac{dQ_n}{dt} = J^2 \rho W \tau_n dx - \frac{dQ_s}{dt} - \frac{dQ_n}{dt}, \qquad \text{Eq. 6.1}$$

where $J^2 \rho W \tau_n dx$ is the joule heating from the applied current density J in the infinitesimal slice of nanowire having electrical resistivity ρ. Assuming that each infinitesimal slice of nanowire has a uniform cross-sectional temperature,

$$\frac{dQ_n}{dt} \approx -(k_n \nabla^2 T(x,0)) W \tau_n dx = -(k_n \nabla^2 \Delta T(x)) W \tau_n dx, \qquad \text{Eq. 6.2}$$

where k_n is the thermal conductivity of the nanowire and $\Delta T(x) = T(x,0) - T_0$ is the temperature difference between the wire and the ambient back-gate temperature. The rate of heat loss through the substrate, dQ_s/dt, can be approximated as

$$\frac{dQ_s}{dt} = -K_s \Delta T(x), \qquad \text{Eq. 6.3}$$

where K_s is the net thermal conductance from the nanowire slice at temperature T to the substrate at temperature T_0 and we assume no thermal resistance at the interface.

6.3 Assumptions and Boundary Conditions

Assuming negligible heat is conducted along the nanowire ($\hat{x}$) direction within the substrate, K_s can be approximated as follows. For thick substrates ($d \gg W$) the temperature within the substrate is determined by a radial heat flow far from the wire ($y \gg W$) as shown in Fig. 6.1b and can be approximated as

$$T(x,y) = -\frac{dQ_s}{dt}\frac{\ln(y)}{k_s \pi dx} + f(x), \qquad \text{Eq. 6.4}$$

where k_s is the thermal conductivity of the substrate and $f(x)$ is an x-dependent function. However, near the wire ($y \ll W$), Eq. (6.4) has an unphysical divergence which does not agree with the expected linear temperature dependence,

$$T(x,y) = -\frac{dQ_s}{dt}\frac{y}{k_s W dx} + T(x,0). \qquad \text{Eq. 6.5}$$

To match the behaviors at both extremes, we introduce a change of variables through

$$s(y) = y + \gamma e^{-\frac{2y}{W}}, \qquad \text{Eq. 6.6}$$

which interpolates between Eqs. (6.4) and (6.5). By substituting $s(y)$ for y in Eq. (6.5) we obtain

$$T(x,y) = -\frac{dQ_s}{dt}\frac{\ln(s)}{k_s \pi dx} + f(x), \qquad \text{Eq. 6.7}$$

which behaves as Eq. (4) for $y \gg W$ and has the correct linear dependence for $y \ll W$. Expanding Eq. (6.7) to linear order for small y and matching the terms in Eq. (6.5) requires that

$$\gamma = \frac{W}{2+\pi}, \qquad \text{Eq. 6.8}$$

and

$$f(x) = T(x,0) + \frac{dQ_s}{dt}\frac{1}{k_s \pi dx} ln\left(\frac{W}{2+\pi}\right). \qquad \text{Eq. 6.9}$$

Inserting these constants into Eq. (6.7) and setting the temperature at $y = d$ to be the ambient back-gate temperature T_0 yields

$$\frac{dQ_s}{dt} = \frac{k_s \pi}{\ln\left(\frac{d}{W}(2+\pi) + e^{-\frac{2d}{W}}\right)} dx \Delta T(x). \qquad \text{Eq. 6.10}$$

Equations (6.2) and (6.10) can now be inserted into (6.1) to obtain the approximate steady state heat equation for the nanowire,

$$\nabla^2 \Delta T(x) - m_1^2 \Delta T(x) + \frac{Q}{k_n} = 0, \qquad \text{Eq. 6.11}$$

where

$$Q = J^2\rho, \tag{Eq. 6.12}$$

and

$$m_1^2 = \frac{k_s\pi}{W\tau_n k_n \ln\left(\frac{d}{W}(2+\pi)+e^{-\frac{2d}{W}}\right)}. \tag{Eq. 6.13}$$

In the wider contact region we follow a similar derivation but with two modifications. First, heat generated in the contact can be neglected due to the significantly reduced current density so that $Q = 0$. Second, we assume that the width of the contact, W_C, is much greater than the thickness of the oxide layer, as is often the case. This implies that the heat flow into the substrate from the contact is approximately one-dimensional at each location (*i.e.*, heat spreading from the contact down through the substrate can be ignored). Therefore, the steady state heat equation for the contact is

$$\nabla^2\Delta T(x) - m_2^2\Delta T(x) = 0, \tag{Eq. 6.14}$$

where

$$m_2^2 = \frac{k_s}{k_c\tau_c d}. \tag{Eq. 6. 15}$$

Assuming that the temperature gradients in the nanowire are predominantly along the $\hat{x}$ direction, and since the maximum temperature occurs at the center of the wire, we use the one dimensional solution to Eq. (6.11),

$$\Delta T(x) = Ae^{m_1x} + Ae^{-m_1x} + \frac{Q}{k_n m_1^2} = 2A\cosh(m_1x) + \frac{Q}{k_n m_1^2}, \tag{Eq. 6.16}$$

where A is a constant chosen to satisfy the boundary conditions and $1/m_1$ is the thermal healing length along the nanowire.

The temperature profile in the contact can be broken up into three regions for each contact. We assume that the temperature variations in the contact closest to the nanowire remain approximately one-dimensional along the $\hat{x}$ direction and then smoothly changes over to a radial two-dimensional behavior moving away from the nanowire. In the radial two-dimensional region we can write Eq. (14) as

$$r^2\frac{d^2\Delta T}{dr^2} + r\frac{d\Delta T}{dr} - m_2^2 r^2\Delta T = 0, \tag{Eq. 6.17}$$

which has the modified Bessel functions of order zero, $I_0(rm_2)$ and $K_0(rm_2)$, as its two solutions. Since we expect the temperature to decay for large r, and $I_0(rm_2) \to \infty$ as $r \to \infty$, we only use the K_0 Bessel function.

In order to smoothly interpolate between the K_0 Bessel function and the one-dimensional behavior at the nanowire we again use a change of variables where

$$s_C(r) = r + \gamma_C e^{-\frac{2r}{W}}. \qquad \text{Eq. 6.18}$$

Since $K_0 \sim -\ln(r) + constant$ for small r, we again find that $\gamma_C = \gamma = \frac{W}{2+\pi}$, assuming that negligible heat is sunk into the substrate over the small region of the interpolation. Thus, an approximate function that describes the temperature profile of the contact in the vicinity of the nanowire is

$$\Delta T = BK_0(m_2 s_C), \qquad \text{Eq. 6.19}$$

where B is a constant determined by the boundary conditions. For portions of the contact further from the nanowire than $W_C/2$, we assume that the temperature profile is again one-dimensional. This gives an exponentially decreasing function for the temperature profile in this region,

$$\Delta T = Ce^{-m_2 x}, \qquad \text{Eq. 6.20}$$

where C is another constant determined by the boundary conditions.

To summarize, the temperature along the length of the device can be written as

$$\Delta T(x) = 2A\cosh(m_1 x) + \frac{Q}{k_n m_1^2} \qquad \text{for } |x| \le L/2, \qquad \text{Eq. 6.21}$$

$$\Delta T(x) = BK_0\left(m_2\left(|x| - \frac{L}{2} + \frac{W}{2+\pi}e^{-2(|x|-L/2)/W}\right)\right) \qquad \text{Eq. 6.22}$$

for

$$L/2 < |x| \le W_C/2,$$

and

$$\Delta T(x) = Ce^{-m_2\left(|x| - \frac{W_C}{2}\right)}, \qquad \text{for } W_C/2 < \pm x, \qquad \text{Eq. 6.23}$$

where the $\hat{x}$-axis zero is located at the center of the nanowire and the solutions are assumed symmetric about this point. We determine the three constants A, B, and C by requiring three boundary conditions. The first two are that $\Delta T(x)$ be continuous across the boundaries at $L/2$ and $W_C/2$. A third boundary condition is that heat flows from the nanowire to the contact in the vicinity of the boundary at $L/2$, resulting in the condition,

$$I^2 R_c + W\left(\tau_n k_n \frac{d\Delta T_n}{dx} - \tau_c k_c \frac{d\Delta T_c}{dx}\right) = 0, \quad \text{Eq. 6.24}$$

where R_c is the electrical contact resistance between the nanowire and the contact electrodes, and $\frac{d\Delta T_n}{dx}$ and $\frac{d\Delta T_c}{dx}$ are the temperature gradients on (respectively) the nanowire and contact sides of the boundary. In the case where R_c is negligible and the thicknesses and thermal conductivities of the nanowire and contacts are the same, equation (6.24) reduces to the requirement that the temperature vary smoothly across the boundary at $x = \pm L/2$, *i.e.*, that the temperature gradient be continuous.

6.4 Comparisons to Finite Element Simulations

For comparison to our model, we have performed finite element simulations of metallic nanowires of length $L = 1.0\ \mu$m connected to electrodes as in Fig. 6.1 assuming that the thicknesses and thermal conductivities of the contacts and nanowires are equal, such that $\tau_c = \tau_n = \tau = 20\ nm$ and $k_c = k_n = k = 109.3 \frac{W}{m\cdot K}$, while the thermal conductivity of the electrically insulating substrate is $k_s = 1.38\ \frac{W}{m\cdot K}$ and the contact width is $W_C = 3\ \mu$m. Figure 6.2a shows a cross-sectional temperature map of the simulation results through the center of a metallic nanowire of width $W = 20$ nm and an electrical insulator thickness of $d = 300$ nm. In this figure the higher temperatures are represented by red near the nanowire, with the lower temperatures represented by blue in the region of the back conducting plane located near the lower edge of the map. The isothermal lines in this figure clearly demonstrate the radial heat flow within the intermediate region of the electrical insulator (*i.e.*, not too close to the nanowire or the back conductor) as assumed in the above derivations (see Eq. (4) and Fig. 6.1b). Figure 6.2b shows the top-view temperature map of the same simulation in the plane $y = 0$ which also clearly demonstrates

the radial symmetry of the temperature decrease moving away from the nanowire within the contacts, as assumed above in the derivations (see Eq. (17) and Fig. 6.1c).

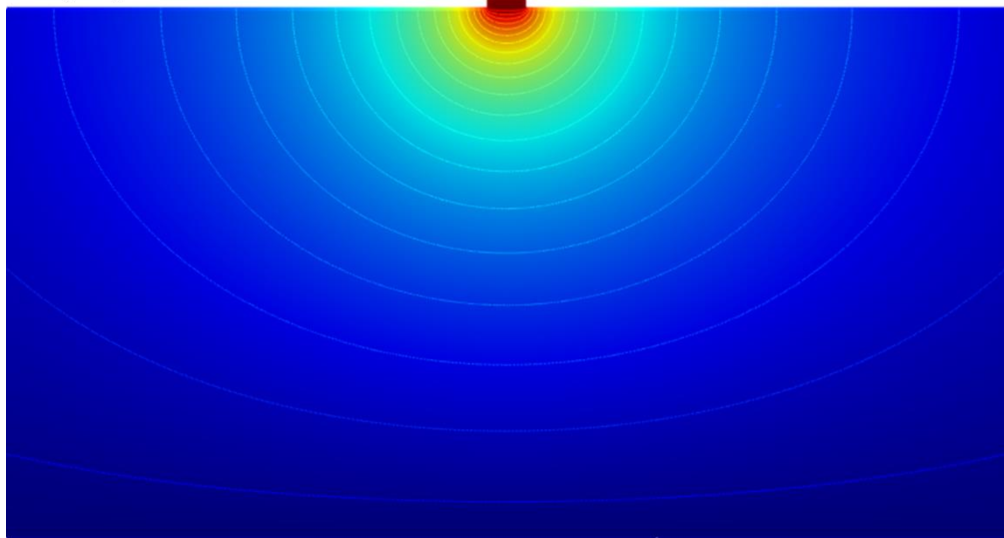

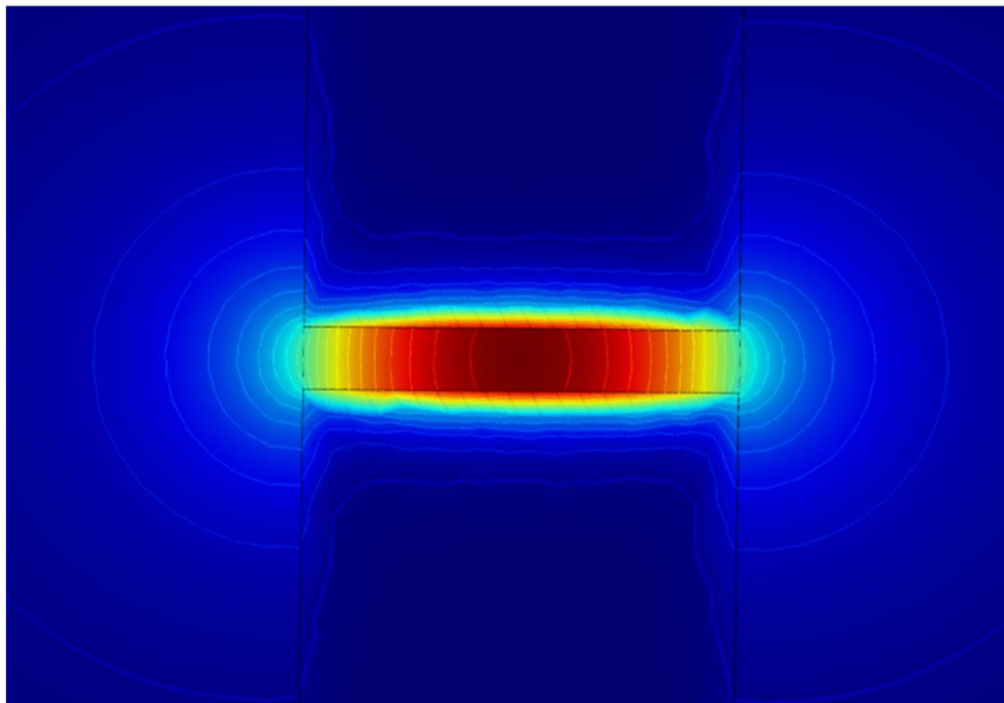

Figure 6.2. (a) Finite-element simulation (cross-sectional view) showing isothermal lines due to the Joule heat generated in the nanowire and flowing into the electrically insulating substrate. The nanowire has $\tau = 20$ nm, $W = 20$ nm, while the electrically insulating substrate has $d = 300$ nm. (b) Finite element simulation (top view) showing isothermal lines due to the heat generated and flowing into the contacts.

6.5 Electrical Current Studies

Figure 6.3 shows a comparison of our model (Eqs. (6.21-6.23)) represented as solid lines to simulations for four applied currents ranging from 0.5 mA to 2.0 mA. The data shown are the temperature rises due to Joule heating along the $\hat{x}$-axis (or length of the nanowire). Excellent agreement between the simulations and our model are observed over this current range.

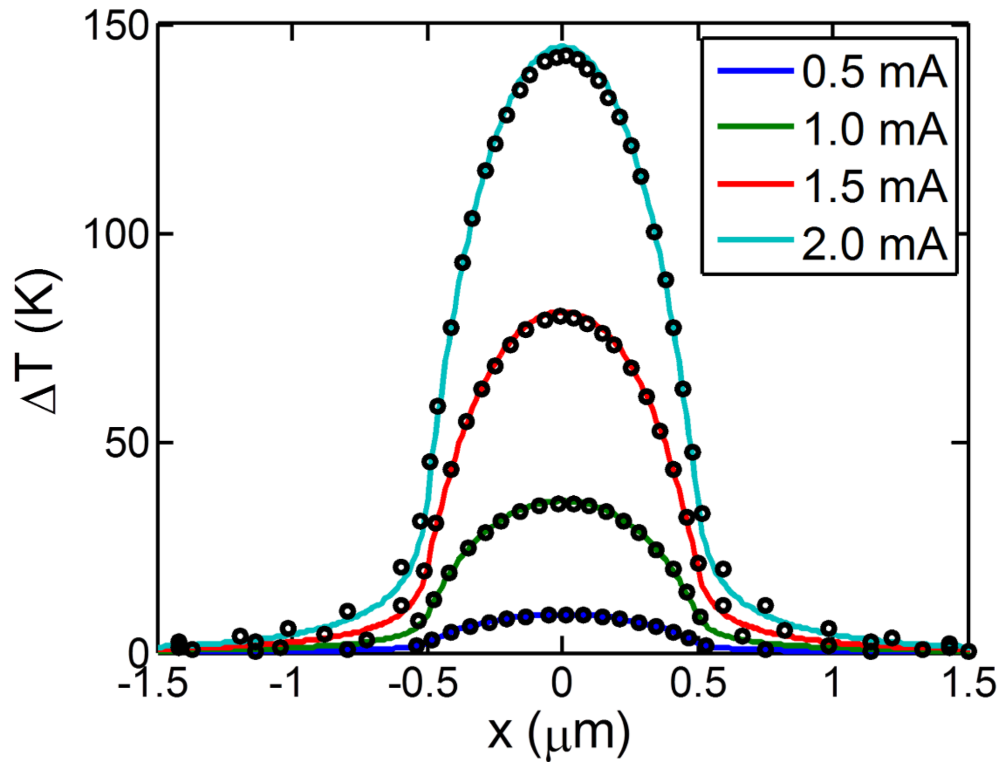

Figure 6.3. Plot of temperature rise versus position for a range of applied current densities for a nanowire. The nanowire has $\tau = 20$ nm, $W = 50$ nm, while the electrically insulating substrate has $d = 200$ nm. The model (Eqs. (6.21-6.23)) is represented by the colored lines while the finite element simulations are represented by the small circles.

6.6 Nanowire Width and Oxide Thickness Studies

Figure 6.4 shows a comparison of our model (blue solid lines) to simulations (small circles) for nanowires having various widths (from 20 to 200 nm) and insulator thicknesses (of either 20 or 200 nm) as denoted. The quality of these fits is evident from a comparison to other nanowire Joule heating models that have recently been used.

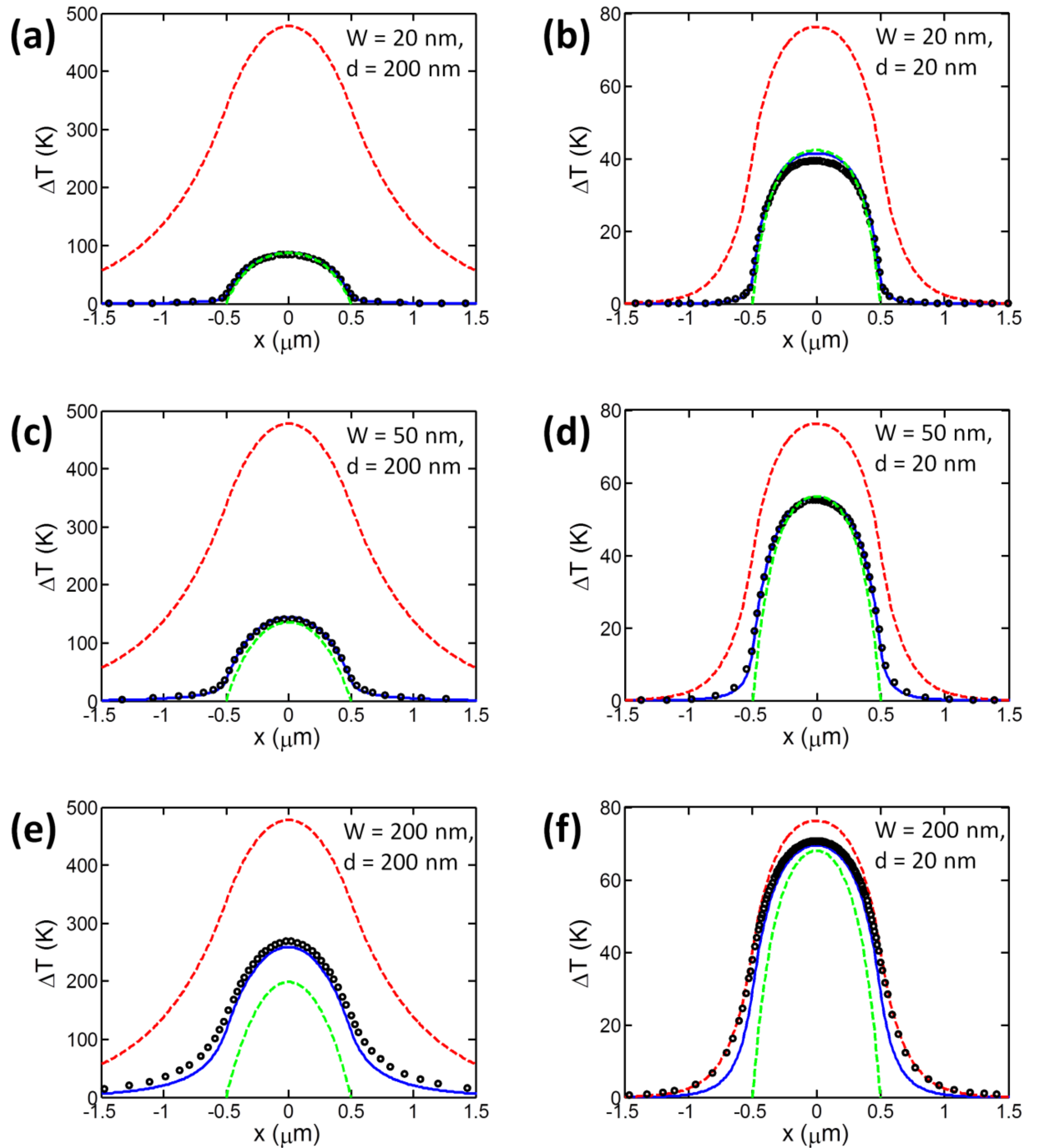

Figure 6.4. Simulations (small circles) and our model (solid-blue lines) for nanowires of given widths, W, and electrical insulator thicknesses, d. Other recent models are shown as dashed lines. A 'non-spreading' that does not model the heat spreading below the nanowire or within the contact is shown as the upper-red dashed lines in each panel. A 'clamped' model that assumes the contacts are fixed at the ambient temperature is shown as the lower-green dashed lines. All nanowires have $\tau = 20$ nm, $L = 1.0\ \mu$m, $k_c = k_n = k = 109.3\ \frac{W}{m \cdot K}$, and $W_C = 3\ \mu m$, while the electrically insulating substrate has $k_s = 1.38\ \frac{W}{m \cdot K}$.

6.7 Significant Improvement over Other Models

One such model that has been used to describe the breakdown of metallic nanowires having the same thickness and material properties as the contacts uses a solution of the heat equation without considering any spreading below the nanowire (as observed in our simulations in Fig. 6.2a) or within the contact (as in Fig. 6.2b).[164,178,179] This 'non-spreading' model for the exact same material properties and geometries is shown in Fig. 6.4 as the upper-red dashed line in each panel.

Another recent model with which we make comparison has been used to describe the Joule heating and breakdown of carbon nanotubes[181,182] and graphene nanoribbons.[52,183] While this model takes into account heat spreading below the nanowire and through the electrically insulating substrate, it assumes that the temperature of the contacts is clamped at a constant ambient temperature. This 'clamped' model employs an empirical formula for the heat spreading below the wire which results in a healing length of $1/m_1$ which is nearly identical to the one we derive above. This healing length can then be inserted into the clamped solution for the temperature rise,[182] $\Delta T(x) = \frac{J^2 \rho}{k_n m_1^2}\left[1 - \frac{cosh(m_1 x)}{cosh(m_1 L/2)}\right]$. This model is shown as the lower-dashed green lines in each of the panels in Fig. 6.4.

From Fig. 6.4, it is clear that our model is superior to the 'clamped' or 'non-spreading' ones at correctly describing the temperature rise of the nanowires over a range of nanowire geometrical parameters. This improvement is even more striking in the vicinity of the nanowire-contact interface as seen in the three images in Fig. 6.5 that focus on these regions.

6.8 Geometrical Regimes of Validity

The regimes of validity of the models plotted in Figs. 6.4 and 6.5 can be understood by considering the relevant length scales in the nanowire system. The two relevant thermal length scales are the healing length within the nanowire ($L_H = 1/m_1$) and within the contact pad ($L_{HC} = 1/m_2$). For the diffusive model we have used to be applicable, both the phonon and electron mean free paths within the nanowire should be shorter than L_H while the mean free path for phonons within the contact should be shorter than L_{HC}.

When L_{HC} is larger than the width W of the nanowire, the heat spreading within the contact must be taken into account. Table 6.1 shows the ratio of L_{Hc}/W for the nanowire geometries in Fig. 6.4. For Figs. 6.4a-6.4e, $L_{Hc}/W > 1$ implying that heat spreading within the contact is significant for these cases, which is also consistent with the poor fits of the 'non-spreading' model in comparison to ours. In contrast, parameters for Fig. 6.4f have $L_{Hc}/W > 1$ indicating that spreading is not significant and is supported by the fact that the 'non-spreading' model and our model perform similarly well for these parameters.

It is also important to consider the locations (*i.e.*, whether within the nanowire or within the contact) of the temperature drops for determining the regimes of validity for the various models. These temperature drops can be estimated by defining the thermal resistances of the nanowire (R_n^{Th}) and the contacts (R_c^{Th}). These thermal resistances will act in series, so their relative magnitudes will determine the location of greatest temperature drop. The thermal resistance of the nanowire can be estimated as $R_n^{Th} \approx L_H/(W\tau_n k_n)$ for cases where $L > L_H$ (as is the case for all the nanowires investigated here). The thermal resistance of the contact can be estimated as $R_c^{Th} \approx 1/(\tau_c k_c)$ for the case where $L_{Hc}/W > 1$ and $R_c^{Th} \approx L_{Hc}/(W\tau_c k_c)$ for $L_{Hc}/W < 1$. The larger the ratio R_c^{Th}/R_n^{Th}, the greater the temperature drop within the contacts. In such cases where R_c^{Th}/R_n^{Th} is large, modeling the heat flow within the contact (as our model does) becomes more important. This is supported by the results shown in Fig. 6.4 where the clamped model performs significantly worse than ours for the parameters of Figs. 6.4e and 6.4f that have the largest values for R_c^{Th}/R_n^{Th} (see Table 6.1).

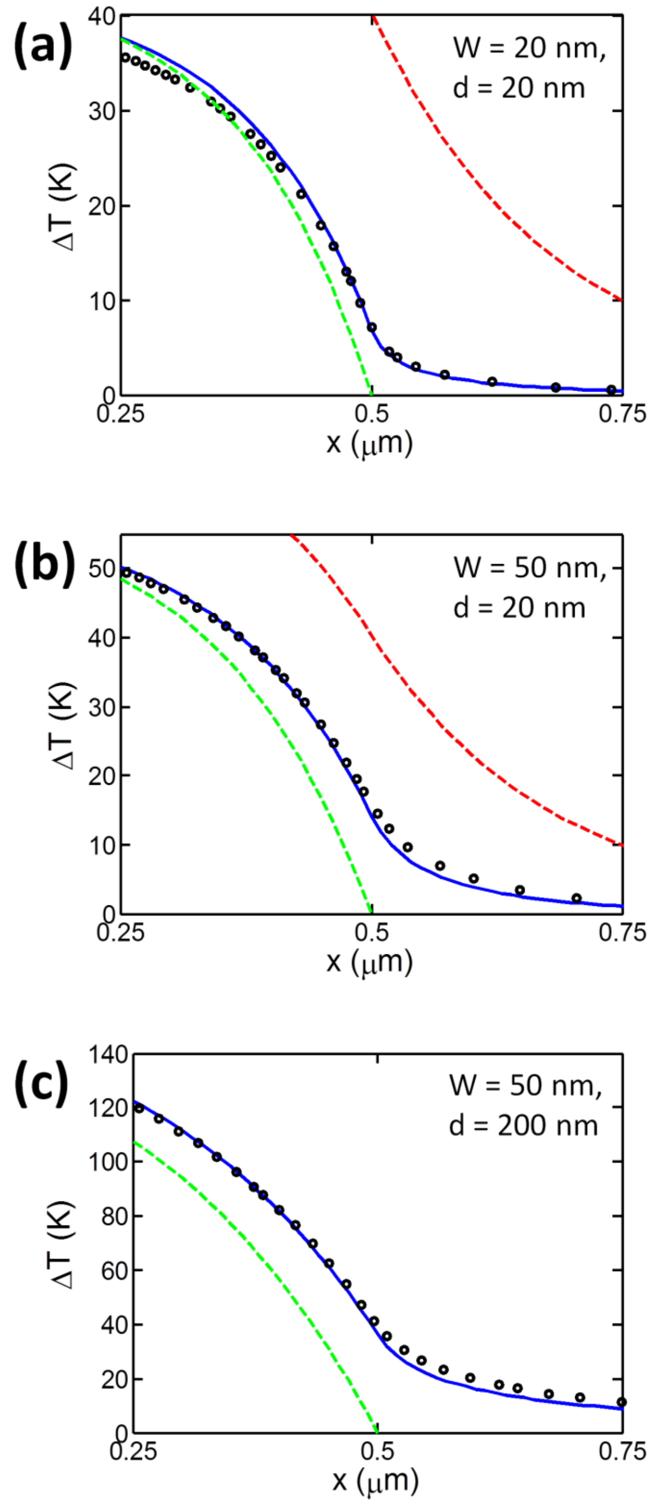

Figure 6.5. Simulations (small circles) focusing on the contact region for nanowires of given widths, W, and electrical insulator thicknesses, d. Our model (solid-blue lines), a 'non-spreading' model (red upper dashed lines), and 'clamped' model (green lower dashed lines) are shown for comparison.

Table 6.1. Thermal healing lengths L_H for the nanowires of widths W and electrical insulator thicknesses d in Fig. 6.4. Also tabulated are the ratios (L_{Hc}/W) of the thermal healing lengths within the contact pads to the nanowire widths and the ratios (R_c^{Th}/R_n^{Th}) of the thermal resistances of the contacts to those of the nanowires.

W (nm)	d (nm)	L_H (nm)	L_{Hc}/W	R_c^{Th}/R_n^{Th}
20.0	200.0	202	28.6	0.099
20.0	20.0	131	9.03	0.152
50.0	200.0	280	11.4	0.178
50.0	20.0	154	3.61	0.324
200.0	200.0	416	2.86	0.481
200.0	20.0	173	0.903	1.05

6.9 Temperature-dependent Resistivities

So far, we have assumed temperature independent material parameters for the nanowire, as is typically assumed in thermal modeling of nanowire systems.[164,178,179,181,182] This assumption is valid for small temperature rises over which the material parameters can be taken as approximately constant. For cases where the electrical resistance of the nanowire can be approximated with a linear temperature dependence, $\rho \approx \rho_0(1+\alpha\Delta T)$, the thermal conductivity of the nanowire can be estimated as a constant according to the Wiedemann-Franz law.[184] This scenario should arise when the scattering of electrons off phonons dominates the electrical resistivity in comparison to scattering off of defects or the nanowire surfaces. Such a scenario results in an additional term linear in ΔT in Eq. (6.11) and can be solved using the same method we discuss above (in section II). This additional term results in a thermal healing length for the nanowire given by $L_H = 1/\sqrt{{m_1}^2 - J^2\rho_0\alpha/k_n}$ which depends on the applied current density. Figure 6.6 shows a comparison of our model with (upper green line) and without (lower blue line) a linear temperature dependence to the electrical resistivity. The small circles on each of the curves are finite-element simulations using the exact same parameters, which demonstrates that

our model can be directly extended to cases where the material parameters can be linearized to obtain a differential equation in the form of Eq. (6.11).

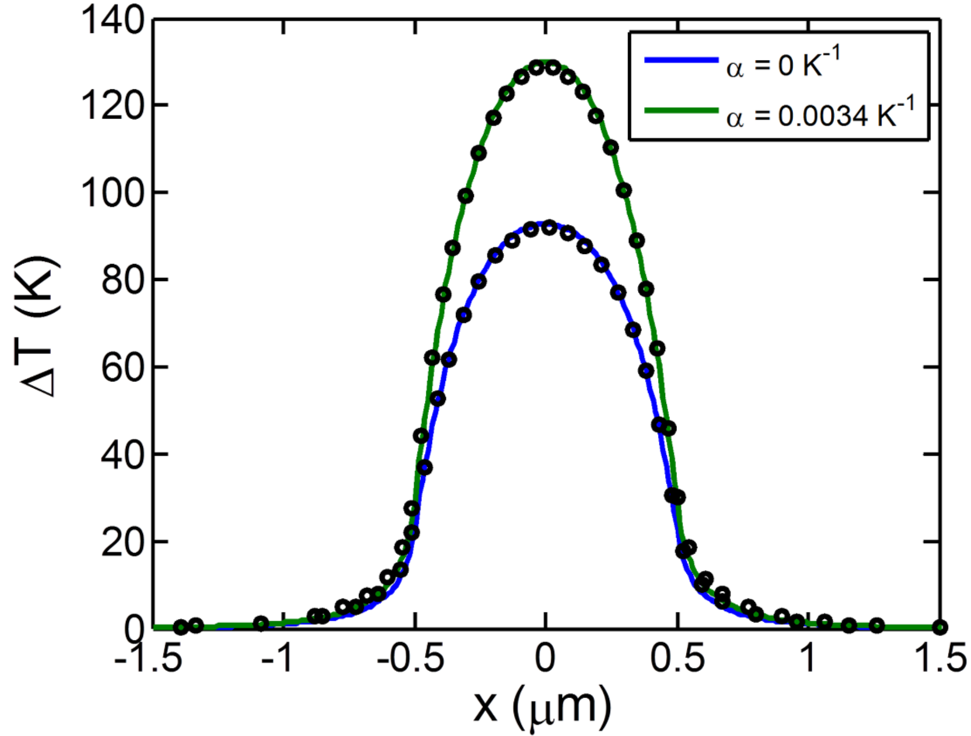

Figure 6.6. Plot of temperature rise versus position for a nanowire with a temperature-independent resistivity having $\alpha = 0.0\,K^{-1}$ (lower blue line) and a temperature-dependent resistivity having $\alpha = 3.4 \times 10^{-3}\,K^{-1}$ (upper green line).

6.10 Conclusions

We have formulated an analytical diffusive model of Joule heating in a nanowire system that incorporates the heat spreading both below the nanowire and within the contact region through an interpolation function. Comparison of our analytical model with finite-element simulations shows excellent agreement over a wider range of system parameters in comparison to other recent models. Our heat-spreading model is particularly useful for cases when the width of the nanowire is less than the thermal healing length of the contacts and when the thermal resistance of the contact is appreciable relative to the thermal resistance of the nanowire. Our model also allows the inclusion of contact resistances that may be present at nanowire-contact interfaces and, in addition, can accommodate materials

with a linear temperature-dependent electrical resistivity. Our analytical model could find utility in designing electronic interconnects to withstand high applied currents and to understanding device degradation in nanowire systems.

Copyright © David Patrick Hunley 2015

APPENDICES

Appendix A: Cantilever Characterization

In order to apply precise load forces while scanning a sample, it is necessary to determine the spring constant (k) of a particular tip, as the actual value may vary significantly from the values supplied by the manufacturer. It is also necessary to determine the inverse optical lever sensitivity ($InvOLS$, units of nm/volt) which is the proportionality constant used to determine the deflection of the cantilever, in nanometers, from the vertical deflection voltage (V_{def}). From these, we have $Z_{def} = InvOLS \cdot V_{def}$, and the applied load force $L = -k \cdot Z_{def}$, which when combined, allow us to apply a specific load force by setting V_{def}.

The net load force F_{net} (the average net force over a flat horizontal surface) is the sum of L and the adhesion force (A) between the tip and sample. In general, the adhesion force can depend on van der Waals (vdW) forces, sample charging, tip geometry, and environmental conditions such as humidity. Measurement of the adhesion force was done by bringing the tip into contact with the sample surface then retracting it while monitoring the deflection voltage to determine the force required to snap the tip off the sample surface (Fig. A1). We found that differences in the tip-graphene and tip-SiO_2 adhesion forces are negligible for the results presented here (Fig. A2). The adhesion force also tends to increase due to wear on the tip at high loads (Fig. A3) therefore the adhesion was measured between successive scans.

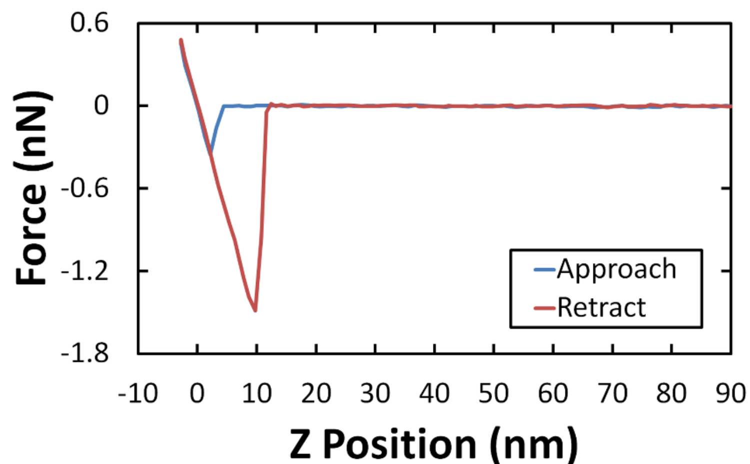

Figure A1. Adhesion/Force Curve Plots. The tip-sample adhesion force is measured by taking a force-distance curve. During this measurement, the tip is brought into hard contact with the sample surface. As the cantilever is retracted to withdraw the tip, adhesive forces oppose the release of the tip from the surface. The force measured just before the tip is released, in this case ≈1.5 nN, is the adhesion force.

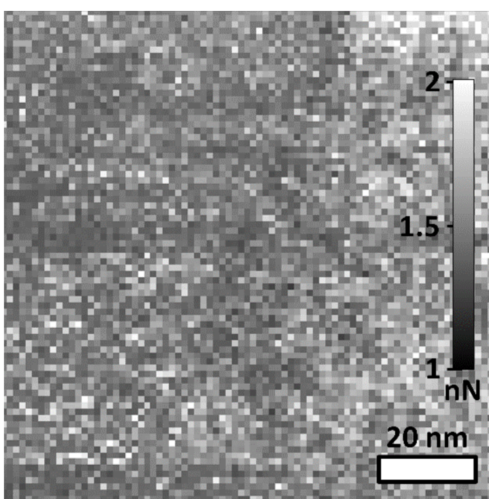

Figure A2. Adhesion force maps over various regions of sample. An adhesion force map is generated by taking a force-distance curve at every point during a scan centered about the same location as the AFM image shown in Fig. 5.1a (main text) for a single-layer on single-layer graphene cross. On average, we find the differences in the tip-graphene and tip-SiO_2 adhesion forces to be less than 0.2 nN.

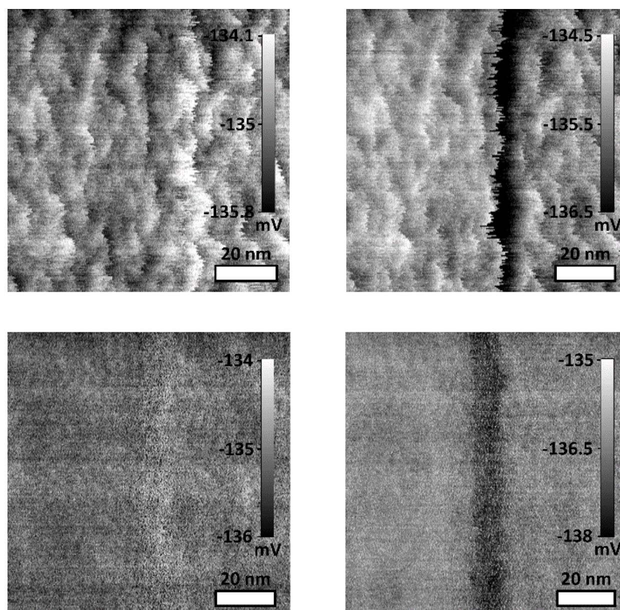

Figure A3. Effects of tip-wear. a-b, Trace and retrace LFM images, respectively, of an uncovered graphene step edge taken with a net applied load of 4.0 nN using a pristine LFM probe that exhibited an adhesion force of about ~1.0 nN. Note that the graphene edge compression features are enhanced. c-d, Respective LFM trace and retrace image comparisons of a similar region acquired with a net applied load of 3.9 nN with the same tip after it was scanned at a high load (approximately 20 nN) over the SiO_2 surface. The high-load scans were performed four times with a square window scan size of 125 nm and a scan rate of 0.6 Hz. The blunted tip exhibited an adhesion force of about 2.9 nN.

Crosstalk, the convolution of the lateral deflection voltages into the vertical deflection voltage channel and vice versa, must also be considered when making LFM measurements. This crosstalk can have many possible sources, including a rotated PSD, asymmetries in the tip/cantilever, or large changes in either topographical or frictional features in the sample.[150] In these experiments, it was found that the degree of crosstalk was largely dependent on the tip being used and only probes that exhibited minimal crosstalk were used.

Copyright © David Patrick Hunley 2015

Appendix B: Lateral Force Models

To quantify these changes in friction and morphology, we model the forces on an AFM cantilever tip as shown in the schematic in Figs. 5.1b and 5.1c (main text) as it is dragged over the local surface having an incline angle θ. The forces on the tip are balanced by the forces and moments applied to the AFM cantilever and will sum to zero assuming the tip is not accelerating. Separating the forces parallel and normal to the inclined surface yields respectively for the rightward (trace) motion of the tip,

$$\text{(B1)} \quad T_t \cos\theta - L\sin\theta - F_{f_t} - A\sin\theta_A = 0$$

$$\text{(B2)} \quad -T_t \sin\theta - L\cos\theta \mp N - A\cos\theta_A = 0,$$

where the applied horizontal force on the cantilever is T_t, the vertical load applied to the cantilever is L, the frictional force at the tip is F_{f_t}, and A is the adhesion force on the tip which is directed at the angle of θ_A with respect to the normal of the surface. We will also assume Amonton's law such that $F_{f_t} = \mu N$, where μ is the coefficient of friction and N is the normal force acting on the tip from the surface. This normal force can be eliminated from equations (B1) and (B2) and solved for T_t such that

$$\text{(B3)} \quad T_t = \frac{L(\sin\theta + \mu\cos\theta) + A(\sin\theta_A + \mu\cos\theta_A)}{\cos\theta - \mu\sin\theta}.$$

We will assume small angles for the topography so that θ and θ_A are small and we can approximate T_t as

$$\text{(B4)} \quad T_t \approx \frac{L(\theta+\mu) + A(\theta_A+\mu)}{1-\mu\theta}.$$

Likewise the horizontal force for the leftward (retrace) motion of the tip is

$$\text{(B5)} \quad T_r = \frac{L(\sin\theta - \mu\cos\theta) + A(\sin\theta_A - \mu\cos\theta_A)}{\cos\theta + \mu\sin\theta} \approx \frac{L(\theta-\mu) + A(\theta_A-\mu)}{1+\mu\theta}.$$

Assuming a small tilt angle φ for the cantilever and requiring that the sum of the moments about the tip of the cantilever be zero we obtain

$$\text{(B6)} \quad M_t - \left(h + \frac{t}{2}\right) T_t - L\left(h + \frac{t}{2}\right)\varphi_t = 0,$$

where M_t is the constraining moment applied by the fixed base of the cantilever, h is the AFM tip height, and t is the cantilever beam thickness. Since the externally applied moment is in response to the torsional rotation of the cantilever by φ, we can relate the two quantities through

(B7) $$\varphi_t = \frac{M_t l}{GJ},$$

where l is the length of the cantilever, G is the shear modulus, and J is the torsion constant of the cantilever which depends on its geometrical cross section. Equation (B6) can now be written as

(B8) $$M_t \left\{1 - \frac{L\left(h+\frac{t}{2}\right)l}{GJ}\right\} = \left(h + \frac{t}{2}\right) T_t.$$

For the cantilevers we use and for vertical cantilever loads $L \lesssim 10\ nN$, we have $\frac{L\left(h+\frac{t}{2}\right)l}{GJ} \ll 1$, so that Eq. (B8) can be approximated as

(B9) $$M_t = \left(h + \frac{t}{2}\right) T_t,$$

with a similar relation for the retrace scan direction.

In LFM, we measure a voltage signal for the trace direction V_t that is related to the torsional rotation and, thus, the torsional moment on the cantilever. For small torsional angles this relation is (for both trace and retrace signals respectively)

(B10) $$V_t = V_0 + \frac{M_t}{\alpha\left(h+\frac{t}{2}\right)},$$

and

(B11) $$V_r = V_0 + \frac{M_r}{\alpha\left(h+\frac{t}{2}\right)},$$

where V_0 is an offset and α is the LFM calibration coefficient where the term $\alpha\left(h + \frac{t}{2}\right)$ converts a torsional moment applied to the cantilever to the measured voltage. For a flat surface with the lateral force only due to frictional effects, the term $\frac{M_t}{\left(h+\frac{t}{2}\right)}$ is the frictional force. We can determine the local frictional and topographical changes using the above

relations by taking half the difference ($\mathrm{W}_V = (V_t - V_r)/2$) and the average ($\Delta_V = (V_t + V_r)/2$,) of the trace and retrace voltage measurements, such that

$$\text{(B12)} \quad \mathrm{W}_V = \frac{1}{2\alpha}(T_t - T_r) \approx \frac{\mu(L+A)}{\alpha},$$

and,

$$\text{(B13)} \quad \Delta_{V_0} = \Delta_V - V_0 = \frac{1}{2\alpha}(T_t + T_r) \approx \frac{L\theta + A\theta_A + (L+A)\mu^2\theta}{\alpha},$$

where we have only kept terms to linear order in the small angles. The V_0 baseline can be estimated by taking the spatial average of Δ_V over a region where we expect θ and θ_A to vary equally on either side of zero. We use the flat regions over uniform thicknesses of FLG to perform this baseline determination.

Equation (B12) can be inverted to determine the local coefficient of friction from experimentally determined values such that,

$$\text{(B14)} \quad \mu = \frac{\alpha \mathrm{W}_V}{(L+A)}.$$

The local coefficient of friction of a surface can be obtained once the calibration coefficient α is determined.

Unlike the coefficient of friction, the local topography determined by the measurements is highly influenced by the relation between θ and θ_A. Conventionally, θ_A is chosen to be zero such that the adhesion is always directed normal to the local contact between the AFM tip and the surface. However, this choice is not necessarily valid for very short inclines that are appropriate for atomic scale changes in topography. Thus we arrive at the two possible cases: For normal adhesion we have,

$$\text{(B15)} \quad \theta = \frac{\alpha \Delta_{V_0}}{L + (L+A)\mu^2},$$

while for vertical adhesion we have,

$$\text{(B16)} \quad \theta = \frac{\alpha \Delta_{V_0}}{(L+A)(1+\mu^2)}.$$

For both cases we consider here for the adhesion, the local coefficient of friction can be determined from Eq. (B14) and inserted into Eqs. (B15) and (B16) to determine the local slope of the topography.

Copyright © David Patrick Hunley 2015

REFERENCES

[1] Geim, A. K.; Novoselov, K. S. *Nat Mater* **2007**, *6*, 183.
[2] Lee, C.; Wei, X.; Kysar, J. W.; Hone, J. *Science* **2008**, *321*, 385.
[3] Chen, J.-H.; Jang, C.; Xiao, S.; Ishigami, M.; Fuhrer, M. S. *Nat Nano* **2008**, *3*, 206.
[4] Morozov, S. V.; Novoselov, K. S.; Katsnelson, M. I.; Schedin, F.; Elias, D. C.; Jaszczak, J. A.; Geim, A. K. *Physical Review Letters* **2008**, *100*, 016602.
[5] Ghosh, S.; Calizo, I.; Teweldebrhan, D.; Pokatilov, E. P.; Nika, D. L.; Balandin, A. A.; Bao, W.; Miao, F.; Lau, C. N. *Applied Physics Letters* **2008**, *92*.
[6] Nair, R. R.; Blake, P.; Grigorenko, A. N.; Novoselov, K. S.; Booth, T. J.; Stauber, T.; Peres, N. M. R.; Geim, A. K. *Science* **2008**, *320*, 1308.
[7] Costello, K. *HYBRIDIZATON: Flexibility at its best.* http://www.chemistryland.com/CHM151S/09-CovalentBonds/Covalent.html. (accessed January 14, 2015).
[8] Leo, K. *Organic Semiconductor World.* **2014**. http://www.iapp.de/orgworld/?Basics:What_are_organic_semiconductors. (accessed January 14, 2015).
[9] Schönenberger, C. *Bandstructure of Graphene and Carbon Nanotubes: An Exercise in Condensed Matter Physics.* **2000**. http://www.google.com/url?sa=t&rct=j&q=&esrc=s&source=web&cd=13&cad=rja&uact=8&ved=0CG8QFjAM&url=http%3A%2F%2Focw.mit.edu%2Fcourses%2Fphysics%2F8-04-quantum-physics-i-spring-2013%2Fstudy-materials%2FMIT8_04S13_BandGrapheneCNT.pdf&ei=gOiJVOuLGIT7yATw7oCADQ&usg=AFQjCNH3oOSvYWSPQ82VIdhMAOX5FCy4KQ. (accessed January 14, 2015).
[10] Haarlammert, T. Doctoral Dissertation, University of Münster, **2011**.
[11] Graz University of Technology. *Molecular and Solid State Physics.* http://lamp.tu-graz.ac.at/~hadley/ss1/bands/tightbinding/tightbinding.php. (accessed January 14, 2015).
[12] Saito, R.; Dresselhaus, G.; Dresselhaus, M. S. *Physical Properties of Carbon Nanotubes*; Imperial College Press: Imperial College, **1998**.
[13] Avouris, P.; Chen, Z.; Perebeinos, V. *Nat Nano* **2007**, *2*, 605.
[14] Kebes. *CNTnames.* **2005**. http://commons.wikimedia.org/wiki/File:CNTnames.png. (accessed April 3, 2015).
[15] Javey, A.; Guo, J.; Wang, Q.; Lundstrom, M.; Dai, H. *Nature* **2003**, *424*, 654.
[16] Buldum, A.; Lu, J. P. *Phys. Rev. B* **2001**, *63*, 161403.
[17] Wong, H.-S. P., Akinwande, Deji *Nanotube and Graphene Device Physics*; Cambridge University Press, **2011**.
[18] Bolotin, K. I.; Sikes, K. J.; Hone, J.; Stormer, H. L.; Kim, P. *Physical Review Letters* **2008**, *101*, 096802.
[19] Purewal, M. S.; Hong, B. H.; Ravi, A.; Chandra, B.; Hone, J.; Kim, P. *Physical Review Letters* **2007**, *98*, 186808.
[20] White, C. T.; Todorov, T. N. *Nature* **1998**, *393*, 240.
[21] Committee, I. R. *Semiconductor Industry Association, San Francisco, CA, available at: http://www. itrs. net/Links/2013ITRS/2013Chapters/2013ExecutiveSummary. pdf* **2013**.
[22] Pereira, V. M.; Castro Neto, A. H.; Peres, N. M. R. *Phys. Rev. B* **2009**, *80*, 045401.
[23] Guinea, F.; Katsnelson, M. I.; Geim, A. K. *Nat Phys* **2010**, *6*, 30.
[24] Geim, A. K.; MacDonald, A. H. *Physics Today* **2007**, *60*, 35.
[25] Jia, X.; Campos-Delgado, J.; Terrones, M.; Meunier, V.; Dresselhaus, M. S. *Nanoscale* **2011**, *3*, 86.

[26] Nakada, K.; Fujita, M.; Dresselhaus, G.; Dresselhaus, M. S. *Phys. Rev. B* **1996**, *54*, 17954.
[27] Guimaraes, M. H. D.; Shevtsov, O.; Waintal, X.; van Wees, B. J. *Phys. Rev. B* **2012**, *85*.
[28] Son, Y.-W.; Cohen, M. L.; Louie, S. G. *Nature* **2006**, *444*, 347.
[29] Son, Y.-W.; Cohen, M. L.; Louie, S. G. *Phys. Rev. Lett.* **2006**, *97*, Art. No. 216803.
[30] Barone, V.; Hod, O.; Scuseria, G. E. *Nano Lett.* **2006**, *6*, 2748.
[31] Cruz-Silva, E.; Botello-Mendez, A. R.; Barnett, Z. M.; Jia, X.; Dresselhaus, M. S.; Terrones, H.; Terrones, M.; Sumpter, B. G.; Meunier, V. *Physical Review Letters* **2010**, *105*.
[32] Jia, X.; Hofmann, M.; Meunier, V.; Sumpter, B. G.; Campos-Delgado, J.; Romo-Herrera, J. M.; Son, H.; Hsieh, Y.-P.; Reina, A.; Kong, J.; Terrones, M.; Dresselhaus, M. S. *Science* **2009**, *323*, 1701.
[33] Lu, Y.; Goldsmith, B.; Strachan, D. R.; Lim, J. H.; Luo, Z.; Johnson, A. T. C. *Small* **2010**, *6*, 2748.
[34] Ponomarenko, L. A.; Schedin, F.; Katsnelson, M. I.; Yang, R.; Hill, E. W.; Novoselov, K. S.; Geim, A. K. *Science* **2008**, *320*, 356.
[35] Kim, K.; Sussman, A.; Zettl, A. *ACS Nano* **2010**, *4*, 1362.
[36] Han, M. Y.; Ozyilmaz, B.; Zhang, Y.; Kim, P. *Phys. Rev. Lett.* **2007**, *98*, Art. No. 206805.
[37] Jiao, L. Y.; Xie, L. M.; Dai, H. J. *Nano Res.* **2012**, *5*, 292.
[38] Jiao, L. Y.; Wang, X. R.; Diankov, G.; Wang, H. L.; Dai, H. J. *Nat. Nanotechnol.* **2010**, *5*, 321.
[39] Jiao, L.; Zhang, L.; Wang, X.; Diankov, G.; Dai, H. *Nature* **2009**, *458*, 877.
[40] Lu, Y.; Merchant, C. A.; Drndic, M.; Johnson, A. T. C. *Nano Letters* **2011**, *11*, 5184.
[41] Borrnert, F.; Fu, L.; Gorantla, S.; Knupfer, M.; Buchner, B.; Rummeli, M. H. *ACS Nano* **2012**, *6*, 10327.
[42] Fischbein, M. D.; Drndic, M. *Applied Physics Letters* **2008**, *93*, 113107.
[43] Moser, J.; Bachtold, A. *Applied Physics Letters* **2009**, *95*, 173506.
[44] Standley, B.; Bao, W.; Zhang, H.; Bruck, J.; Lau, C. N.; Bockrath, M. *Nano Letters* **2008**, *8*, 3345.
[45] Kosynkin, D. V.; Higginbotham, A. L.; Sinitskii, A.; Lomeda, J. R.; Dimiev, A.; Price, B. K.; Tour, J. M. *Nature* **2009**, *458*, 872.
[46] Cai, J. M.; Ruffieux, P.; Jaafar, R.; Bieri, M.; Braun, T.; Blankenburg, S.; Muoth, M.; Seitsonen, A. P.; Saleh, M.; Feng, X. L.; Mullen, K.; Fasel, R. *Nature* **2010**, *466*, 470.
[47] Prins, F.; Barreiro, A.; Ruitenberg, J. W.; Seldenthuis, J. S.; Aliaga-Alcalde, N.; Vandersypen, L. M. K.; van der Zant, H. S. J. *Nano Letters* **2011**, *11*, 4607.
[48] Narita, A.; Feng, X. L.; Hernandez, Y.; Jensen, S. A.; Bonn, M.; Yang, H. F.; Verzhbitskiy, I. A.; Casiraghi, C.; Hansen, M. R.; Koch, A. H. R.; Fytas, G.; Ivasenko, O.; Li, B.; Mali, K. S.; Balandina, T.; Mahesh, S.; De Feyter, S.; Mullen, K. *Nat. Chem.* **2014**, *6*, 126.
[49] Datta, S. S.; Strachan, D. R.; Khamis, S. M.; Johnson, A. T. *Nano Lett.* **2008**, *8*, 1912
[50] Tomita, A.; Tamai, Y. *J. Phys. Chem.* **1974**, *78*, 2254.
[51] Campos, L. C.; Manfrinato, V. R.; Sanchez-Yamagishi, J. D.; Kong, J.; Jarillo-Herrero, P. *Nano Lett* **2009**, *9*, 2600.
[52] Liao, A. D.; Wu, J. Z.; Wang, X. R.; Tahy, K.; Jena, D.; Dai, H. J.; Pop, E. *Physical Review Letters* **2011**, *106*.
[53] Wang, X.; Ouyang, Y.; Li, X.; Wang, H.; Guo, J.; Dai, H. *Phys. Rev. Lett.* **2008**, *100*, 206803.
[54] Chen, Z.; Lin, Y.-M.; Rooks, M. J.; Avouris, P. *Physica E* **2007**, *40*, 228.
[55] Hunley, D. P.; Sundararajan, A.; Boland, M. J.; Strachan, D. R. *Applied Physics Letters* **2014**, *105*.
[56] Datta, S. S.; Strachan, D. R.; Mele, E. J.; Johnson, A. T. *Nano Lett.* **2009**, *9*, 7
[57] Novoselov, K. S.; Geim, A. K.; Morozov, S. V.; Jiang, D.; Zhang, Y.; Dubonos, S. V.; Grigorieva, I. V.; Firsov, A. A. *Science* **2004**, *306*, 666.

[58] Hunley, D. P.; Johnson, S. L.; Stieha, J. K.; Sundararajan, A.; Meacham, A. T.; Ivanov, I. N.; Strachan, D. R. *ACS Nano* **2011**, *5*, 6403.

[59] Nasseri, M.; Hunley, D. P.; Sundararajan, A.; Boland, M. J.; Strachan, D. R. *Carbon* **2014**, *77*, 958.

[60] Bonnell, D. *Scanning probe microscopy and spectroscopy: theory, techniques, and applications*; 2nd ed.; Wiley-VCH, Inc., **2001**.

[61] Brown, K. A.; Satzinger, K. J.; Westervelt, R. M. *Nanotechnology* **2012**, *23*.

[62] Guriyanova, S.; Golovko, D. S.; Bonaccurso, E. *Meas. Sci. Technol.* **2010**, *21*.

[63] Jacobs, H. O.; Leuchtmann, P.; Homan, O. J.; Stemmer, A. *J. Appl. Phys.* **1998**, *84*, 1168.

[64] Cherniavskaya, O.; Chen, L. W.; Weng, V.; Yuditsky, L.; Brus, L. E. *J. Phys. Chem. B* **2003**, *107*, 1525.

[65] Tsutsui, M.; Taniguchi, M. *Sensors* **2012**, *12*, 7259.

[66] Geim, A. K.; Novoselov, K. S. *Nature Materials* **2007**, *6*, 183.

[67] Zhou, W. W.; Ding, L.; Liu, J. *Nano Res.* **2009**, *2*, 593.

[68] Ismach, A.; Segev, L.; Wachtel, E.; Joselevich, E. *Angew. Chem.-Int. Edit.* **2004**, *43*, 6140.

[69] Kocabas, C.; Hur, S.-H.; Gaur, A.; Meitl, M. A.; Shim, M.; Rogers, J. A. *Small* **2005**, *1*, 1110.

[70] Han, S.; Liu, X.; Zhou, C. *Journal of the American Chemical Society* **2005**, *127*, 5294.

[71] Xiao, J.; Dunham, S.; Liu, P.; Zhang, Y.; Kocabas, C.; Moh, L.; Huang, Y.; Hwang, K.-C.; Lu, C.; Huang, W.; Rogers, J. A. *Nano Letters* **2009**, *9*, 4311.

[72] Ishigami, N.; Ago, H.; Imamoto, K.; Tsuji, M.; Iakoubovskii, K.; Minami, N. *Journal of the American Chemical Society* **2008**, *130*, 9918.

[73] Huang, S.; Cai, X.; Liu, J. *Journal of the American Chemical Society* **2003**, *125*, 5636.

[74] Huang, S. M.; Woodson, M.; Smalley, R.; Liu, J. *Nano Letters* **2004**, *4*, 1025.

[75] Zhang, Y.; Chang, A.; Cao, J.; Wang, Q.; Kim, W.; Li, Y.; Morris, N.; Yenilmez, E.; Kong, J.; Dai, H. *Applied Physics Letters* **2001**, *79*, 3155.

[76] Kocabas, C.; Kang, S. J.; Ozel, T.; Shim, M.; Rogers, J. A. *J. Phys. Chem. C* **2007**, *111*, 17879.

[77] Jeon, S.; Lee, C.; Tang, J. Y.; Hone, J.; Nuckolls, C. *Nano Res.* **2008**, *1*, 427.

[78] Geblinger, N.; Ismach, A.; Joselevich, E. *Nat. Nanotechnol.* **2008**, *3*, 195.

[79] Ci, L.; Xu, Z. P.; Wang, L. L.; Gao, W.; Ding, F.; Kelly, K. F.; Yakobson, B. I.; Ajayan, P. M. *Nano Res.* **2008**, *1*, 116.

[80] Tapaszto, L.; Dobrik, G.; Lambin, P.; Biro, L. P. *Nat. Nanotechnol.* **2008**, *3*, 397.

[81] He, Y. D.; Dong, H. L.; Li, T.; Wang, C. L.; Shao, W.; Zhang, Y. J.; Jiang, L.; Hu, W. P. *Applied Physics Letters* **2010**, *97*, 3.

[82] Li, X.; Wang, X.; Zhang, L.; Lee, S.; Dai, H. *Science* **2008**, *319*, 1229

[83] Cao, X. H.; He, Q. Y.; Shi, W. H.; Li, B.; Zeng, Z. Y.; Shi, Y. M.; Yan, Q. Y.; Zhang, H. *Small* **2011**, *7*, 1199.

[84] Li, B.; Cao, X. H.; Ong, H. G.; Cheah, J. W.; Zhou, X. Z.; Yin, Z. Y.; Li, H.; Wang, J. L.; Boey, F.; Huang, W.; Zhang, H. *Adv. Mater.* **2010**, *22*, 3058.

[85] Ortolani, L.; Houdellier, F.; Monthioux, M.; Morandi, V. *Carbon* **2010**, *48*, 3050.

[86] Falvo, M. R.; Taylor, R. M.; Helser, A.; Chi, V.; Brooks, F. P.; Washburn, S.; Superfine, R. *Nature* **1999**, *397*, 236.

[87] Paulson, S.; Helser, A.; Nardelli, M. B.; Taylor, R. M.; Falvo, M.; Superfine, R.; Washburn, S. *Science* **2000**, *290*, 1742.

[88] Liu, J.; Rinzler, A. G.; Dai, H. J.; Hafner, J. H.; Bradley, R. K.; Boul, P. J.; Lu, A.; Iverson, T.; Shelimov, K.; Huffman, C. B.; Rodriguez-Macias, F.; Shon, Y. S.; Lee, T. R.; Colbert, D. T.; Smalley, R. E. *Science* **1998**, *280*, 1253.

[89] Falvo, M. R.; Steele, J.; Taylor, R. M.; Superfine, R. *Phys. Rev. B* **2000**, *62*, 10665.

[90] Buldum, A.; Lu, J. P. *Physical Review Letters* **1999**, *83*, 5050.

[91] Yanagi, H.; Sawada, E.; Manivannan, A.; Nagahara, L. A. *Applied Physics Letters* **2001**, *78*, 1355.
[92] Rettig, C.; Bodecker, M.; Hovel, H. *J. Phys. D-Appl. Phys.* **2003**, *36*, 818.
[93] Yi, J. H.; El Khakani, M. A. *Chem. Phys. Lett.* **2005**, *413*, 182.
[94] Miura, K.; Takagi, T.; Kamiya, S.; Sahashi, T.; Yamauchi, M. *Nano Letters* **2001**, *1*, 161.
[95] Hovel, H.; Bodecker, M.; Grimm, B.; Rettig, C. *J. Appl. Phys.* **2002**, *92*, 771.
[96] Kuo, W. S.; Ko, T. H.; Lu, H. F. *Micro Nano Lett.* **2009**, *4*, 128.
[97] Hunley, D. P.; Johnson, S. L.; Stieha, J. K.; Sundararajan, A.; Meacham, A. T.; Ivanov, I. N.; Strachan, D. R. *ACS Nano* **2011**, *5*, 6403.
[98] Schaffel, F.; Wilson, M.; Bachmatiuk, A.; Rummeli, M. H.; Queitsch, U.; Rellinghaus, B.; Briggs, G. A. D.; Warner, J. H. *ACS Nano* **2011**, *5*, 1975.
[99] Schaffel, F.; Warner, J. H.; Bachmatiuk, A.; Rellinghaus, B.; Buchner, B.; Schultz, L.; Rummeli, M. H. *Nano Res.* **2009**, *2*, 695.
[100] Ishigami, M.; Chen, J. H.; Cullen, W. G.; Fuhrer, M. S.; Williams, E. D. *Nano Letters* **2007**, *7*, 1643.
[101] Ismach, A.; Kantorovich, D.; Joselevich, E. *Journal of the American Chemical Society* **2005**, *127*, 11554.
[102] Yao, Z.; Postma, H. W. C.; Balents, L.; Dekker, C. *Nature* **1999**, *402*, 273.
[103] Luo, Z.; Somers, L. A.; Dan, Y.; Ly, T.; Kybert, N. J.; Mele, E. J.; Johnson, A. T. C. *Nano Letters* **2010**, *10*, 777.
[104] Dresselhaus, M. S.; Jorio, A.; Hofmann, M.; Dresselhaus, G.; Saito, R. *Nano Letters* **2010**, *10*, 751.
[105] Schneider, G. F.; Calado, V. E.; Zandbergen, H.; Vandersypen, L. M. K.; Dekker, C. *Nano Letters* **2010**, *10*, 1912.
[106] Lu, W.; Lieber, C. M. *Nature Materials* **2007**, *6*, 841.
[107] Buldum, A.; Lu, J. P. *Phys. Rev. B* **2001**, *63*.
[108] Maarouf, A. A.; Mele, E. J. *Phys. Rev. B* **2011**, *83*.
[109] Buia, C.; Buldum, A.; Lu, J. P. *Phys. Rev. B* **2003**, *67*.
[110] Hipps, K. W. *Science* **2001**, *294*, 536
[111] Franklin, A. D.; Luisier, M.; Han, S. J.; Tulevski, G.; Breslin, C. M.; Gignac, L.; Lundstrom, M. S.; Haensch, W. *Nano Letters* **2012**, *12*, 758.
[112] Franklin, A. D.; Chen, Z. H. *Nat. Nanotechnol.* **2010**, *5*, 858.
[113] Xia, F. N.; Perebeinos, V.; Lin, Y. M.; Wu, Y. Q.; Avouris, P. *Nat. Nanotechnol.* **2011**, *6*, 179.
[114] Cook, B. G.; French, W. R.; Varga, K. *Applied Physics Letters* **2012**, *101*.
[115] Kane, A. A.; Sheps, T.; Branigan, E. T.; Apkarian, V. A.; Cheng, M. H.; Hemminger, J. C.; Hunt, S. R.; Collins, P. G. *Nano Letters* **2009**.
[116] Lee, C.; Wei, X. D.; Kysar, J. W.; Hone, J. *Science* **2008**, *321*, 385.
[117] Murali, R.; Yang, Y.; Brenner, K.; Beck, T.; Meindl, J. D. *Applied Physics Letters* **2009**, *94*, 243114.
[118] Sze, S. M.; Ng, K. K. *Physics of Semiconductor Devices*; Third Edition ed.; John Wiley & Sons, Inc.: Hoboken, NJ, U.S.A., **2007**.
[119] Ribes, G.; Mitard, J.; Denais, M.; Bruyere, S.; Monsieur, F.; Parthasarathy, C.; Vincent, E.; Ghibaudo, G. *IEEE Trans. Device Mater. Reliab.* **2005**, *5*, 5.
[120] Hunley, D. P.; Boland, M. J.; Strachan, D. R. *Adv. Mater.* **2014**, n/a.
[121] Han, S. M.; Benaroya, H.; Wei, T. *J. Sound Vibr.* **1999**, *225*, 935.
[122] Wong, E. W.; Sheehan, P. E.; Lieber, C. M. *Science* **1997**, *277*, 1971.
[123] Ru, C. Q. *Phys. Rev. B* **2000**, *62*, 9973.
[124] Yakobson, B. I.; Brabec, C. J.; Bernholc, J. *Physical Review Letters* **1996**, *76*, 2511.

[125] Berger, C.; Song, Z. M.; Li, T. B.; Li, X. B.; Ogbazghi, A. Y.; Feng, R.; Dai, Z. T.; Marchenkov, A. N.; Conrad, E. H.; First, P. N.; de Heer, W. A. *J. Phys. Chem. B* **2004**, *108*, 19912.
[126] Bolotin, K. I.; Sikes, K. J.; Jiang, Z.; Klima, M.; Fudenberg, G.; Hone, J.; Kim, P.; Stormer, H. L. *Solid State Commun.* **2008**, *146*, 351.
[127] Dutta, S.; Pati, S. K. *J. Mater. Chem.* **2010**, *20*, 8207.
[128] Girit, C. O.; Meyer, J. C.; Erni, R.; Rossell, M. D.; Kisielowski, C.; Yang, L.; Park, C. H.; Crommie, M. F.; Cohen, M. L.; Louie, S. G.; Zettl, A. *Science* **2009**, *323*, 1705.
[129] Guinea, F.; Katsnelson, M. I.; Geim, A. K. *Nat. Phys.* **2010**, *6*, 30.
[130] Levy, N.; Burke, S. A.; Meaker, K. L.; Panlasigui, M.; Zettl, A.; Guinea, F.; Neto, A. H. C.; Crommie, M. F. *Science* **2010**, *329*, 544.
[131] de Juan, F.; Cortijo, A.; Vozmediano, M. A. H.; Cano, A. *Nat. Phys.* **2011**, *7*, 810.
[132] Guinea, F.; Katsnelson, M. I.; Vozmediano, M. A. H. *Phys. Rev. B* **2008**, *77*, 075422.
[133] Guinea, F.; Horovitz, B.; Le Doussal, P. *Phys. Rev. B* **2008**, *77*.
[134] Shenoy, V. B.; Reddy, C. D.; Ramasubramaniam, A.; Zhang, Y. W. *Physical Review Letters* **2008**, *101*, 245501.
[135] Cresti, A.; Fogler, M. M.; Guinea, F.; Neto, A. H. C.; Roche, S. *Physical Review Letters* **2012**, *108*, 166602.
[136] Guinea, F.; Geim, A. K.; Katsnelson, M. I.; Novoselov, K. S. *Phys. Rev. B* **2010**, *81*, 035408.
[137] Fogler, M. M.; Castro Neto, A. H.; Guinea, F. *Phys. Rev. B* **2010**, *81*, 161408.
[138] Prada, E.; San-Jose, P.; Leon, G.; Fogler, M. M.; Guinea, F. *Phys. Rev. B* **2010**, *81*, 161402.
[139] Filleter, T.; McChesney, J. L.; Bostwick, A.; Rotenberg, E.; Emtsev, K. V.; Seyller, T.; Horn, K.; Bennewitz, R. *Physical Review Letters* **2009**, *102*, 086102.
[140] Lee, C.; Li, Q. Y.; Kalb, W.; Liu, X. Z.; Berger, H.; Carpick, R. W.; Hone, J. *Science* **2010**, *328*, 76.
[141] Lee, H.; Lee, N.; Seo, Y.; Eom, J.; Lee, S. *Nanotechnology* **2009**, *20*, 325701.
[142] Choi, J. S.; Kim, J. S.; Byun, I. S.; Lee, D. H.; Lee, M. J.; Park, B. H.; Lee, C.; Yoon, D.; Cheong, H.; Lee, K. H.; Son, Y. W.; Park, J. Y.; Salmeron, M. *Science* **2011**, *333*, 607.
[143] Mate, C. M.; McClelland, G. M.; Erlandsson, R.; Chiang, S. *Physical Review Letters* **1987**, *59*, 1942.
[144] Baselt, D. R.; Baldeschwieler, J. D. *J Vac Sci Technol B* **1992**, *10*, 2316.
[145] Meyer, G.; Amer, N. M. *Appl. Phys. Lett.* **1990**, *57*, 2089.
[146] Steiner, P.; Gnecco, E.; Krok, F.; Budzioch, J.; Walczak, L.; Konior, J.; Szymonski, M.; Meyer, E. *Physical Review Letters* **2011**, *106*, 186104.
[147] Holscher, H.; Ebeling, D.; Schwarz, U. D. *Physical Review Letters* **2008**, *101*, 246105.
[148] Muller, T.; Lohrmann, M.; Kasser, T.; Marti, O.; Mlynek, J.; Krausch, G. *Physical Review Letters* **1997**, *79*, 5066.
[149] Hunley, D. P.; Flynn, T. J.; Dodson, T.; Sundararajan, A.; Boland, M. J.; Strachan, D. R. *Phys. Rev. B* **2013**, *87*, 035417.
[150] Such, M. W.; Kramer, D. E.; Hersam, M. C. *Ultramicroscopy* **2004**, *99*, 189
[151] Varenberg, M.; Etsion, I.; Halperin, G. *Rev. Sci. Instrum.* **2003**, *74*, 3362.
[152] Ogletree, D. F.; Carpick, R. W.; Salmeron, M. *Review of Scientific Instruments* **1996**, *67*, 3298.
[153] Popov, V. L. *Contact Mechanics and Friction, Physical Principles and Applications*; Springer-Verlag: Berlin Heidelberg, **2010**.
[154] Zhang, D. B.; Akatyeva, E.; Dumitrica, T. *Physical Review Letters* **2011**, *106*, 255503.
[155] Cranford, S.; Sen, D.; Buehler, M. J. *Applied Physics Letters* **2009**, *95*, 123121.
[156] Smolyanitsky, A.; Killgore, J. P.; Tewary, V. K. *Phys. Rev. B* **2012**, *85*.

[157] Christou, A. *Electromigration and Electronic Device Degradation*; Wiley-Interscience: New York, **1994**.
[158] Ho, P. S.; Kwok, T. *Rep. Prog. Phys.* **1989**, *52*, 301.
[159] Park, H.; Lim, A. K. L.; Park, J.; Alivisatos, A. P.; McEuen, P. L. *Appl. Phys. Lett.* **1999**, *75*, 301
[160] Liang, W.; Shores, M. P.; Bockrath, M.; Long, J. R.; Park, H. *Nature* **2002**, *417*, 725.
[161] Park, J.; Pasupathy, A. N.; Goldsmith, J. I.; Chang, C.; Yaish, Y.; Petta, J. R.; Rinkoski, M.; Sethna, J. P.; Abruna, H. D.; McEuen, P. L.; Ralph, D. C. *Nature* **2002**, *417*, 722
[162] Yu, L. H.; Natelson, D. *Nano Lett.* **2004**, *4*, 79
[163] Strachan, D. R.; Smith, D. E.; Johnston, D. E.; Park, T.-H.; Therien, M. J.; Bonnell, D. A.; Johnson, A. T. *Appl. Phys. Lett.* **2005**, *86*, 043109.
[164] Hadeed, F. O.; Durkin, C. *Appl. Phys. Lett.* **2007**, *91*, 123120.
[165] Ward, D. R.; Halas, N. J.; Natelson, D. *Applied Physics Letters* **2008**, *93*, 213108.
[166] Johnston, D. E.; Strachan, D. R.; Johnson, A. T. *Nano Lett.* **2007**, *7*, 2774.
[167] Johnson, S. L.; Sundararajan, A.; Hunley, D. P.; Strachan, D. R. *Nanotechnology* **2010**, *21*, 125204.
[168] Johnson, S. L.; Hunley, D. P.; Sundararajan, A.; Johnson, A. T. C.; Strachan, D. R. *IEEE Trans. Nano.* **2010**.
[169] Strachan, D. R.; Johnston, D. E.; Guiton, B. S.; Datta, S. S.; Davies, P. K.; Bonnell, D. A.; Johnson, A. T. *Phys. Rev. Lett.* **2008**, *100*, 056805.
[170] Strachan, D. R.; Smith, D. E.; Fischbein, M. D.; Johnston, D. E.; Guiton, B. S.; Drndic, M.; Bonnell, D. A.; Johnson, A. T. *Nano Lett.* **2006**, *6*, 441.
[171] Esen, G.; Fuhrer, M. S. *Applied Physics Letters* **2005**, *87*, 263101.
[172] Trouwborst, M. L.; van der Molen, S. J.; van Wees, B. J. *J. Appl. Phys.* **2006**, *99*.
[173] Wu, Z. M.; Steinacher, M.; Huber, R.; Calame, M.; van der Molen, S. J.; Schonenberger, C. *Applied Physics Letters* **2007**, *91*, 053118.
[174] Hertel, S.; Kisslinger, F.; Jobst, J.; Waldmann, D.; Krieger, M.; Weber, H. B. *Applied Physics Letters* **2011**, *98*, 212109.
[175] Kuribara, K.; Wang, H.; Uchiyama, N.; Fukuda, K.; Yokota, T.; Zschieschang, U.; Jaye, C.; Fischer, D.; Klauk, H.; Yamamoto, T.; Takimiya, K.; Ikeda, M.; Kuwabara, H.; Sekitani, T.; Loo, Y.-L.; Someya, T. *Nat Commun* **2012**, *3*, 723.
[176] Kang, M. J.; Miyazaki, E.; Osaka, I.; Takimiya, K.; Nakao, A. *ACS Applied Materials & Interfaces* **2013**.
[177] Moser, J.; Barreiro, A.; Bachtold, A. *Applied Physics Letters* **2007**, *91*.
[178] Durkan, C.; Schneider, M. A.; Welland, M. E. *J. Appl. Phys.* **1999**, *86*, 1280.
[179] Durkan, C.; Welland, M. E. *Ultramicroscopy* **2000**, *82*, 125.
[180] Hunley, D. P.; Johnson, S. L.; Flores, R. L.; Sundararajan, A.; Strachan, D. R. *J. Appl. Phys.* **2013**, *113*.
[181] Pop, E. *Nanotechnology* **2008**, *19*, 295202.
[182] Pop, E.; Mann, D. A.; Goodson, K. E.; Dai, H. *J. Appl. Phys.* **2007**, *101*, 093710.
[183] Yu, Y. J.; Han, M. Y.; Berciaud, S.; Georgescu, A. B.; Heinz, T. F.; Brus, L. E.; Kim, K. S.; Kim, P. *Applied Physics Letters* **2011**, *99*.
[184] Ashcroft, N. W.; Mermin, N. D. *Solid State Physics*; W. B. Saunders Company: Philadelphia, **1976**.

VITA

DAVID PATRICK HUNLEY

EDUCATION

University of Kentucky, Lexington, Kentucky
Thesis advisor: Professor Douglas R. Strachan
Research Focus: Nanomaterials and Nanotechnology
M.S. in Physics (2010)
Morehead State University, Morehead, Kentucky
B.S. in Physics (2007)
B.S. in Mathematics (2007)

PROFESSIONAL EXPERIENCE

Graduate Research Assistant, University of Kentucky (Sept. 2009 – Present)

Teaching Assistant, Department of Physics and Astronomy, University of Kentucky (2008 – 2009, 2012 – 2014)

Research Experience for Undergraduates (REU) Graduate Assistant, Department of Electrical and Computer Engineering, University of Kentucky: (June 2008 – August 2008)

Laboratory Assistant, Department of Physics, Morehead State University (2005 – 2007)

Research Experience for Undergraduates (REU) Awardee, Department of Electrical and Computer Engineering, University of Kentucky (June 2006 – August 2006)

Math and Science Tutor, Learning Lab, Morehead State University, (2004 – 2006)

Undergraduate Research Assistant, Department of Physics, Morehead State University (January 2006 – May 2006)

Research Experience for Undergraduates (REU) Awardee, Department of Physics and Astronomy, University of Toledo (June 2005 – August 2005)

PUBLICATIONS

D. Patrick Hunley, Mathias J. Boland, and Douglas R. Strachan, *Integration of Nanotubes, Etch Tracks, and Nanoribbons in Crystallographic Alignment to a Graphene Lattice*, Advanced Materials, Vol. 27, 5, pp 813-818 (2015)

D. Patrick Hunley, Abhishek Sundararajan, and Douglas R. Strachan, *Electrostatic Force Microscopy and Electrical Isolation of Etched Few-Layer Graphene Nano-Domains*, Applied Physics Letters, 105, 243109 (2014)

Mohsen Nasseri, **D. Patrick Hunley**, Abhishek Sundararajan, Mathias J. Boland, and Douglas R. Strachan, *Tuning Between Crystallographically Aligned Carbon Nanotube Growth and Graphene Etching,* CARBON, Vol. 77, pp 958-963 (2014)

Abhishek Sundararajan, Mathias J. Boland, **D. Patrick Hunley**, and Douglas R. Strachan, *Doping and Hysteretic Switching of Polymer-Encapsulated Graphene Field Effect Devices*, Applied Physics Letters, 103, 253505 (2013)

D. Patrick Hunley, Stephen L. Johnson, Roel L. Flores, Abhishek Sundararajan, and Douglas R. Strachan, *Analytical Model for Self-Heating in Nanowire Geometries*, Journal of Applied Physics. 113, 234306 (2013)

D. Patrick Hunley, Tyler J. Flynn, Tom Dodson, Abhishek Sundararajan, Mathias J. Boland, and Douglas R. Strachan, *Friction, Adhesion, and Elasticity of Graphene Edges*, Physical Review B, 87, 035417 (2013)

D. Patrick Hunley, Stephen L. Johnson, Joseph K. Stieha, Abhishek Sundararajan, Aaron T. Meacham, Ilia N. Ivanov, and Douglas R. Strachan, *Crystallographically Aligned Carbon Nanotubes Grown on Few-Layer Graphene Films*, ACS Nano, 5 (8), pp 6403-6409 (2011)

S. L. Johnson, **D. P. Hunley**, A. Sundararajan, A. T. C. Johnson, and D. R. Strachan, *High-Throughput Nanogap Formation Using Single Ramp Feedback Control*, IEEE Transactions on Nanotechnology, Vol. 10, No. 4 (2011)

S. L. Johnson, A. Sundararajan, **D. P. Hunley**, and D. R. Strachan, *Memristive Switching of Single-Component Metallic Nanowires*, Nanotechnology 21, 125204 (2010)

W. Tan, **D. Patrick Hunley**, and Ingrid St. Omer, *Properties of Silicon Carbide Nanotubes Formed via Reaction of SiO powder with SWCNTs and MWCNTs*, SoutheastCon 2009 Proceedings IEEE (2009)

E. T. Legba, **D. Patrick Hunley**, Nikki Olida, and Ingrid St. Omer, *Synthesis and Characterization of Silicon Carbide (SiC) Microstructures*, SoutheastCon 2007 Proceedings IEEE (2007)

Kent Price, Chris Lacy, and **D. Patrick Hunley**, *Photovoltage Decay in CdTe/CdS Solar Cells*, Proceedings of the 2006 IEEE 4th World Conference on Photovoltaic Energy Conversion (2006)

PATENTS

David Patrick Hunley and Douglas Robert Strachan. *Integrated Multi-Terminal Devices Consisting of Carbon Nanotube, Few-Layer Graphene Nanogaps, and Few-Layer Graphene Nanoribbons Having Crystallographically Controlled Interfaces*. Submitted to the University of Kentucky Intellectual Property Office on June 3, 2014, Invention ID: INV14/2016.

Douglas Robert Strachan and **David Patrick Hunley**. *Crystallographically-Oriented Carbon Nanotubes Grown on Few-Layer Graphene Films*. U.S. Patent 20130025918 A1, filed October 1, 2012, currently pending.

Douglas R. Strachan, Joseph Kelly Stieha, **D. Patrick Hunley**, Stephen Lee Johnson, JR. 2013. *Few-Layer Graphene Nanoribbon and a Method of Making the Same*. U.S. Patent 20140004327 A1, filed June 29, 2012, currently pending.

HONORS AND AWARDS

University of Kentucky Graduate School Academic Year Fellowship, 2012 – 2013
Two-year recipient of the University of Kentucky Center for Advanced Materials Fellowship, 2010 – 2012
1st Place, 9th Annual UK Physics & Astronomy Poster Competition, 2011
1st Place, 8th Annual UK Physics & Astronomy Poster Competition, 2010
Kentucky Opportunity Fellowship, 2007 – 2008
Max Steckler Fellowship, 2007
National Science Foundation's Computer Science, Engineering, and Mathematics Scholarship, 2004 – 2007
William Everhart Endowment Scholarship, 2006 – 2007
2nd Place, UK Research Experience for Undergraduates competition, 2006
2nd Place, Kentucky Academy of Science Undergraduate Research Competition, 2005